

AFM AND IMAGING XPS DATA CORRELATION

A dissertation submitted
to Kent State University in partial
fulfillment of the requirements for the
degree of Doctor of Philosophy

by

Jabari O. Farrar

December 2004

Dissertation written by
Jabari O. Farrar
B.S., Kent State University, 1997
Ph.D., Kent State University, 2004

Approved by

_____, Chair, Doctoral Dissertation Committee
_____, Members, Doctoral Dissertation Committee
_____,
_____,
_____,
_____,

Accepted by

_____, Chair, Department of Chemistry
_____, Dean, College of Arts and Sciences

TABLE OF CONTENTS

LIST OF FIGURES.....	v
LIST OF TABLES.....	viii
ACKNOWLEDGEMENTS.....	ix
CHAPTER	
I. Introduction.....	1
II. X-ray Photoelectron Spectroscopy.....	9
Atomic Force Microscopy.....	31
Confocal Microscopy.....	41
III. Image Processing and Multitechnique Correlation and Fusion.....	50
IV. Correlation of AFM and XPS Imaging for Qualitative and Quantitative Phase Identification in Polymer Blends.....	67
V. Image Fusion of Polymer Blends using AFM, Confocal Microscopy and Imaging XPS.....	101
VI. Preliminary Evaluation of Fluorescent Polymer Beads for Image Registration and 3-D Feature Correlation.....	151
VII. Summary and Future Work.....	173
BIBLIOGRAPHY.....	181

LIST OF FIGURES

FIGURE

1.	AFM, imaging XPS, and LSCM sampling depths.....	6
2.	The Photoelectron emission process.....	12
3.	Kratos Axis Ultra spectroscopy mode.....	18
4.	Example of a survey spectrum.....	24
5.	Example of a high resolution spectrum.....	25
6.	Example of valence band spectra.....	26
7.	Kratos Axis Ultra imaging mode.....	28
8.	Example of an XPS high magnification image.....	29
9.	C 1s image and spectra of a PMMA/PVC blend.....	30
10.	Atomic Force Microscope set up.....	33
11.	Force versus distance curve.....	34
12.	Phase imaging.....	37
13.	AFM topography and phase image of PS*/PB.....	40
14.	LSCM set up.....	43
15.	Confocal image of fluorescein labeled polystyrene.....	46
16.	Confocal image of PS*/PMMA blend.....	47
17.	Example of image classification.....	55
18	Example of histogram equalization.....	56

19	Two dimensional histogram to illustrate joint entropy.....	60
20.	Example of a Scree plot.....	64
21.	Example of PCA.....	65
22.	Converting a three-way array into a two-way array.....	66
23.	Example of cropping and XPS image.....	75
24.	Example of a deresolved AFM image.....	80
25.	Resolution matched AFM topography, phase, and XPS images.....	81
26.	Example of image classification of an XPS Cl 2p image.....	83
27.	AFM topography and phase images of PMMA/PVC blends.....	85
28.	XPS O 1s and Cl 2p images of PMMA/PVC blends.....	86
29.	%PMMA detected by AFM vs. % PMMA detected by XPS.....	89
30.	AFM and XPS images taken from the same area on the patterned surface.....	97
31.	AFM and XPS images take from the same area on a PMMA/PVC blend.....	98
32.	Structure of PS* and PB.....	106
33.	Spectra of PS* and PB.....	107
34.	Valence band spectra of PS* and PB.....	109
35.	Confocal image of the marked area.....	110
36.	Confocal and AFM image of the analyzed area.....	112
37.	Confocal slices from a PS*/PB blend.....	113
38.	O 1s and C 1s image of a PS*/PB blend.....	114
39.	Valence band images from a PS*/PB blend.....	116
40.	PCA applied to a set of valence band images.....	117

41.	Comparison of PC #3 and an XPS valence band image.....	119
42.	Image registration using two AFM images.....	121
43.	Confocal image of the marked area.....	122
44.	Registered AFM and confocal image.....	125
45.	Registered AFM, XPS and confocal image.....	126
46.	Structure of PS* and PMMA.....	129
47.	XPS spectra of PS* and PMMA.....	130
48.	Confocal image of the are marked by the AFM tip.....	132
49.	AFM topography and phase image of a PS*/PMMA blend.....	133
50.	Confocal slices from a PS*/PMMA blend.....	134
51.	PCA loadings and scores calculated from the confocal stack.....	135
52.	Confocal principal component image.....	137
53.	XPS images acquired from the PS*/PMMA blend.....	138
54.	PCA scores and loadings calculated from a set of XPS images.....	139
55.	Registered AFM, XPS and confocal images.....	142
56.	Curve-fit spectra of PS* obtained from two different areas.....	147
57.	Plots from the original and quantified confocal data.....	148
58.	Confocal volume and AFM topography profile.....	149
59.	Assembled AFM and confocal volume and a cross-sectional image.....	150

60.	C 1s spectra of PS* microspheres and PMMA.....	157
61.	C 1s and O 1s XPS spectra of PS* microspheres and PP.....	158
62.	Optical image and O 1s XPS image of single bead.....	159
63.	Confocal image of PS* beads where the image contrast has been reversed...	160
64.	Confocal slices from a PS* bead embedded in PTFE-30.....	163
65.	XPS line scan of a single PS* bead.....	164
66.	Cross-sectional image and confocal volume image of a single PS* bead.....	166
67.	AFM image of single bead embedded in PTFE-30.....	167
68.	AFM cross-sectional image of a single bead embedded in PTFE-30.....	168
69.	Registered confocal and AFM images of a single PS* bead.....	172

LIST OF TABLES

TABLE

1. Technique summary.....	49
2. Fractal dimensions of PMMA/PVC blends.....	73
3. % ITO detected by AFM and XPS.....	84
4. Comparison of the % PMMA detected by AFM and XPS.....	88
5. The effect of kernel size on classification for a patterned sample.....	93
6. The effect of kernel size on classification for PMMA/PVC blends.....	94

ACKNOWLEDGEMENTS

I am grateful to my advisor, Dr. Julia Fulghum. Her kindness, patience and encouragement have helped me to reach this accomplishment. I want to give special thanks to Dr. Kateryna Artyushkova and Jeff Fenton. Kateryna, without your help, I would have never been able to finish this dissertation. Jeff, thank you for providing me with the necessary confocal data at the drop of a dime. My appreciation also goes to Dr. Ksenija Dejanovic, who took the time and had the patience to teach me AFM. Just put the broken AFM tips on my bill. I would also like to thank my committee members for their willingness to participate and for their valuable insights.

Special thanks goes to Dr. Patricia Maurice, Dr. Oleg Lavrentovich and Dr. Jeff Brinker for giving me access to their atomic force microscopes so that I can continue my research.

Last, but not least, I would like to thank my parents for their words of encouragement and believing in me.

Funding resources provided for this research are: NSF CHE-0113724
NSF ALCOM (DMR89-20147), NSF IGERT CORE.

CHAPTER 1

INTRODUCTION

Introduction

Polymers blends represent one of the most rapidly growing areas in material science. Polymeric mixtures are important in industry because they allow for the design and control of material properties such as strength, hardness and wear etc. Mixtures are rarely homogenous and an understanding of the spatial and volume composition is essential for correct operation of the final product.¹ Information on the nanometer scale is needed to evaluate advanced materials and is important for their continued development.

A thorough understanding of the surface morphology of heterogeneous organic samples can require the use of several different imaging, as well as spectroscopic, techniques. At a minimum, the imaging methods are likely to have different spatial resolutions, sampling depths, sample preparation requirements and damage mechanisms. As samples become more complex, the evaluation of multi-technique data becomes both more critical and more difficult.

Multi-technique spectroscopic and imaging techniques have been used in the past to study polymer blends. Feng et al. used secondary ion mass spectrometry mass spectrometry (SIMS) and scanning electron microscopy (SEM) to study the

compatibilizing effect of poly (methyl methacrylate) (PMMA) on polycarbonate /poly (vinylidene fluoride) blends.² Artyushkova et al used X-ray photoelectron spectroscopy (XPS) and Fourier transform infrared spectroscopy (FTIR) to understand the phase segregation behavior of poly (methyl methacrylate)/poly (vinyl chloride) blends from the surface and the bulk.³ Lhoest et al, used XPS and SIMS to study the surface segregation of PMMA in Bisphenol A Polycarbonate/ PMMA blends.⁴

Our research group has focused on developing methods for the non-destructive, 3-dimensional characterization of heterogeneous polymeric samples using X-ray photoelectron spectroscopy (XPS), Atomic Force Microscopy (AFM), and Laser Scanning Confocal Microscopy (LSCM) from the exact same area on a sample. One of the problems with multi-technique correlation in the past is that samples were either prepared using different substrates for characterization or data was obtained from different areas on the same sample.⁵ Therefore, any differences observed in the data could have been due to differences in the sampling properties of the techniques, differences in sample preparation, or the fact that data was not obtained from the same areas on the sample. By obtaining data from the same area on a sample, the latter two effects can be eliminated. A multi-technique correlative approach will provide different types of information about the system from the exact same area, which can be integrated to provide a more complete picture of the heterogeneous system under study.

XPS provides a qualitative and quantitative analysis of the top 10 nm of a surface, making it possible to identify different phases observed on the heterogeneous sample with a resolution of 3-5 microns. XPS also has imaging capabilities, allowing for

elemental and chemical distribution maps of a surface to be obtained. The atomic force microscope allows for non-destructive, nanometer resolution imaging of surface topography. In addition, AFM has the ability of to detect surface heterogeneities that will cause contrast in the images, creating what is known as phase images. Confocal microscopy allows one to optically section through the bulk of the sample at various depths throughout the sample. This allows for visualization of the bulk morphology throughout the sample and the subsequent generation of a 3-D volume of the bulk by combining the optical sections.

Fusion of imaging XPS, AFM, and confocal microscopy images can be used to generate a three-dimensional model of a heterogeneous polymeric system since the three techniques have varying sampling depths as shown in Figure 1; however, this involves correlating all three techniques, which is a difficult task. The focus of the research in this dissertation involves one aspect of the project, correlating topography and phase data from AFM with the chemical information obtained from imaging XPS. This is difficult due to differences in technique sampling properties, sampling depth and spatial resolution.

For heterogeneous organic polymeric materials it is important to be able to characterize and understand the structure, phase state and composition on the nanometer scale.⁶ This is what makes AFM ideal for studying polymer blends. AFM has nanometer spatial resolution and is non-destructive to the sample when the appropriate imaging mode is chosen. Within the past ten years there have been many studies utilizing AFM to help elucidate the surface structure and behavior of polymers, making imaging on the

nanometer scale routine.⁷⁻¹² In the past, material scientists traditionally used other high-resolution techniques such as SEM and TEM to observe morphology, surface roughness, surface chemistry etc.^{2,13,14}

These methods often require complex sample preparation, such as etching or coating the sample with a metal, which can lead to a change in or loss of information about the sample and its properties. AFM does not require complicated sample preparation, and the sample is left virtually untouched prior to analysis. One drawback of AFM is that chemical information cannot be obtained from the images, making identification of the observed phases difficult.¹⁵

XPS has also been increasingly used to study the behavior of polymers and polymer blends^{3,16,17}. The improved spatial resolution of XPS has led to the detection of concentration gradients and local regions of high analyte concentrations on the surface, which is important for understanding heterogeneous polymer blends.¹⁸ Concentration gradients were previously undetected due to poor resolution and led to the assumption that the surface was homogeneous. With the advent of imaging XPS and fast parallel imaging with an enhanced lateral resolution, 3-5 microns, polymer blend surfaces can be mapped into two-dimensional images, revealing the surface chemical distribution on the micron scale. In addition, small area spectroscopy with analysis areas as small as 15 microns can yield the chemical composition from a particular area within an image. Combining the chemical and spatial distribution information obtained from XPS images with compositional information obtained from small area spectra, observing polymer blend behavior on the surface becomes possible.

The complementary nature of AFM and XPS is what makes the two techniques ideal for correlative studies of polymer blends. In the literature there has been relatively few publications on multi-technique correlation of polymer blends using AFM and XPS together.¹⁹⁻²¹ These are limited to studies where spectroscopic data was acquired from the surface of a blend with XPS then AFM images of the same surface were obtained to view the surface morphology, but no direct correlation was made from the data. Moreover, there have been no publications correlating imaging XPS and AFM data. To our knowledge, this is the first attempt to correlate AFM topography and phase images with XPS images.

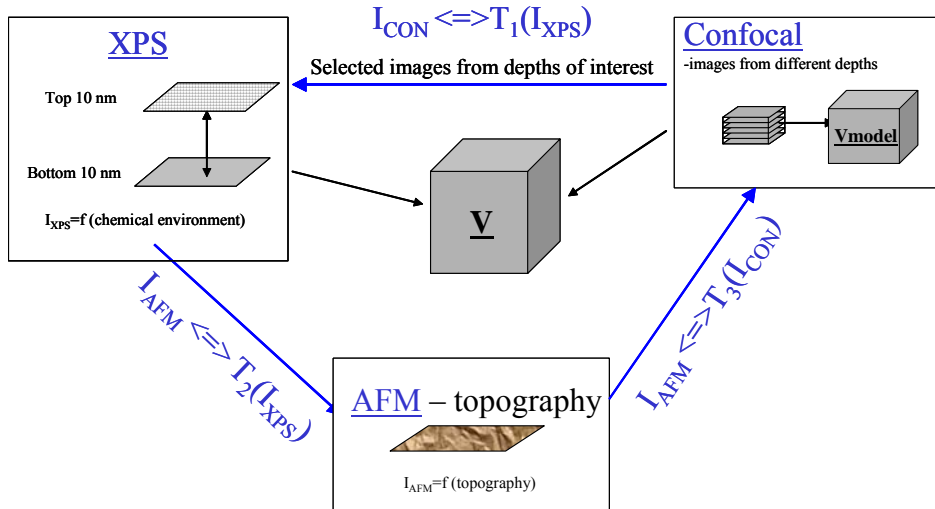


Figure 1. XPS provides elemental and chemical information from the top 10 nm of the surface. AFM provides topography and phase images of the surface on the nanometer scale. Confocal microscopy provides information throughout the bulk of the sample at various depths. Since the three techniques have different sampling depths, the images can be correlated to create a 3-dimensional volume, showing morphology changes throughout the sample.

Correlation of AFM and XPS Imaging for Qualitative and Quantitative Phase Identification in Polymer Blends

XPS provides elemental and chemical information from the top 8-10 nm of a sample. Imaging XPS provides an elemental or chemical distribution map of the surface with a 2-5 μm spatial resolution. Phase-contrast AFM provides information about sample properties, such as adhesion, friction and viscoelasticity, but no direct chemical information can be derived from the images.^{8,22-26} This makes it difficult to identify the phases responsible for the observed contrast. Combining the elemental and chemical information obtained from XPS with the topographical and phase data obtained from AFM, positive identification and quantification of the different phases becomes possible.

Multi-technique correlation of polymeric samples using both AFM and XPS will provide a more complete picture of the sample under study. A method to chemically identify the observed phases in AFM by Quantitative XPS Imaging will be discussed. Correlating the data from both techniques involves resizing, image alignment, resolution matching, and classification methods. The approach will be applied to a patterned polymer surface of known properties for validation and then to heterogeneous polymer blends of Poly (methyl methacrylate)/Poly (vinyl chloride) (PMMA/PVC) to identify and quantify the phases present on the sample surface.

Image Fusion of Polymer Blends using AFM, Confocal Microscopy and Imaging XPS

In order to generate a 3-D model of a heterogeneous organic polymeric sample using XPS, AFM, and confocal microscopy the images from the three different techniques have to be fused. The goal of image fusion is to combine image data to form a new image that contains more interpretable information than could be gained using the original data.

This portion of the dissertation will focus on the development of methods to fuse images from AFM, imaging XPS and LSCM, obtained from the same area on polymer blends. The varying sampling depths of the three techniques will enable a 3-D model to be generated without destroying the sample.

Preliminary Evaluation of Fluorescent Polymer Beads for Image Registration and 3-D Feature Correlation

The goal of this work is to develop a method to obtain data from a single 9 μm microsphere using XPS, AFM and LSCM. Once a method is developed, the dimensions of the features will be measured and compared with each other and the manufacturers value. In addition, the feasibility of using the microspheres as an image registration method is investigated.

CHAPTER 2

THEORY AND INSTRUMENTATION

Introduction

This research develops methods for the correlation of X-ray photoelectron spectroscopy (XPS), atomic force microscopy (AFM), and laser scanning confocal microscopy (LSCM). These techniques are briefly described below.

X-ray Photoelectron Spectroscopy

X-ray Photoelectron Spectroscopy (XPS), also known as electron spectroscopy for chemical analysis (ESCA), is a nondestructive surface characterization technique used to obtain semi-quantitative elemental and chemical information from the top 10 nm of a surface for all elements except hydrogen and helium.²⁷ Kai Sieghban pioneered the technique in the 1960s for which he won a Nobel Prize in physics in 1981.²⁷ XPS has found widespread applications in various areas, including, but not limited to, semiconductors, microelectronics, polymers and catalysts.

The technique is based upon the photoelectric effect. Incident light is used to eject photoelectrons from atoms on a surface. When X-rays are used as a source, core level

photoelectrons are ejected from the atom putting it in an (n-1) electron state as shown in Figure 2(a). The photoemission process can be expressed by the following equation:

$$\text{BE} = h\nu - \text{KE} - \phi \quad (1)$$

In equation (1), BE is the binding energy of the electron in the atom from which it came, and the BE depends upon the atom's atomic number, the atomic shell from which was ejected, and the chemical environment of the atom. $h\nu$ is the photon energy from the X-ray source, KE is the kinetic energy the photoelectron has leaving the surface, and ϕ is the spectrometer work function, which is the energy required to move the electron from the Fermi level into the vacuum. The KE of the ejected photoelectron is measured in the XPS experiment. Since $h\nu$ and ϕ are already known, the BE of the ejected photoelectron can then be calculated. The binding energies are then compared with tables of binding energies or standard spectra to identify chemical state.

After photoemission, the atom reorganizes by moving an electron from an outer shell to the vacancy shown in Figure 2(b). The atom must then rid itself of excess energy by one of two competing processes. In the first process, known as X-ray fluorescence, an X-ray photon with energy equal to the difference between the core level hole and the outer shell electron energy is released. The second process produces what is known as an Auger electron. The excess energy is used to eject an electron from a higher energy level, as shown in Figure 2 (c).²⁷

X-rays penetrate microns into the sample, causing the ejection of core level electrons throughout the sample. However, most of these electrons undergo inelastic scattering and never leave the sample. Electrons that do not undergo any loss of energy before leaving the surface contribute to the photoemission peak; those that escape the surface with energy loss contribute to the background in the spectra. Photoelectrons that escape from the top 8-10 nm of the surface with no energy loss make XPS a surface sensitive technique. The sampling depth can be described in terms of λ , the inelastic mean free path (IMFP). The IMFP is the average distance in nanometers an electron can travel before it undergoes an inelastic collision. In XPS this is defined as the thickness of matter through which 63% of the photoelectrons will lose their energy.²⁷ The sampling depth is defined as 3λ ; values for λ depend upon the electron energy and the material in which the photoelectron travels.

When choosing an X-ray source, two factors must be considered, the width of the source and its energy. The X-ray line width of the source must be narrow enough not to limit the energy resolution of the spectra, and the energy of the source must be high enough to eject core level electrons.²⁸ X-rays are produced by accelerating electrons to the anode material with 10-15kV potentials with respect to the anode. Typical X-ray sources for XPS include aluminum (Al) and magnesium (Mg) sources, along with the higher energy resolution monochromated aluminum source. These sources are commonly used because they have enough energy to excite core and

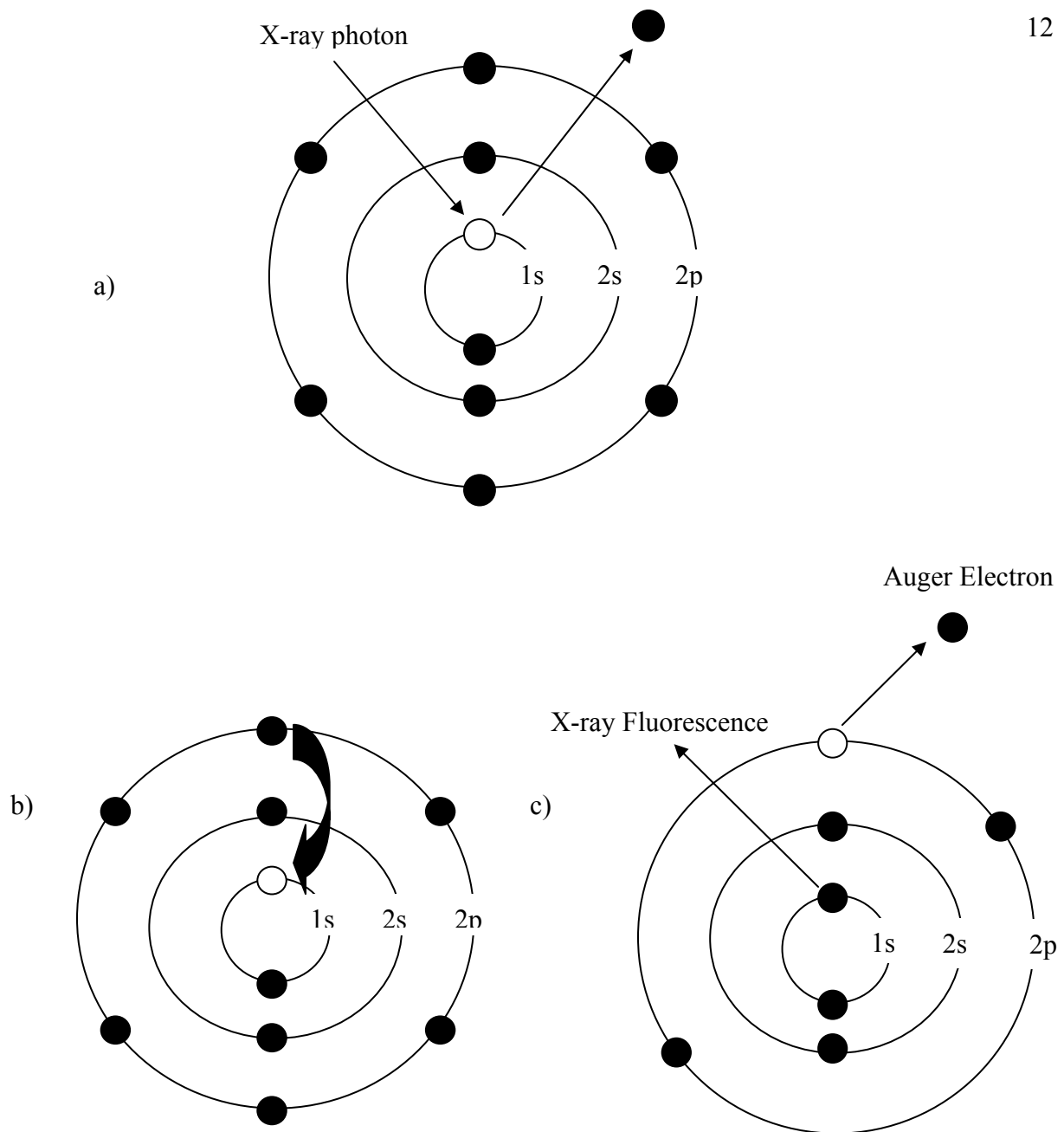


Figure 2. (a) An X-ray photon ejects a core level electron from the atom

(b) An electron from an outer shell fills the vacant core level hole. (c)

The atom must now rid itself of energy by using the excess energy to

emit an Auger electron or by X-ray fluorescence.

valence electrons, low atomic numbers to minimize satellites, a narrow X-ray line width, and are easy to machine.²⁸ An unmonochromated Al K α source has an energy of 1486.6 eV and line width of ~0.85 eV, and the unmonochromated Mg K α source has an energy of 1253.6 eV and a line width of ~0.7 eV. Sources that are not monochromated usually have wide line widths because they contain more than one excitation wavelength, leading to satellite peaks. This is one factor limiting the resolution of the photoelectron spectra.²⁸

Monochromatization is achieved through the use of a crystal to disperse the X-rays. Only radiation that satisfies Bragg's Law, equation 2 below, will be reflected and focused onto the sample.

$$n\lambda = 2d \sin \theta \quad (2)$$

In equation (2), the diffraction order is n, λ is the wavelength of radiation used, d is the spacing of the diffraction grating, and θ is the incident angle of the photons. The diffraction grating is usually a quartz crystal. The monochromatized Al K α X-ray source has a line width of ~0.4 eV, allowing for higher resolution spectra to be obtained. Other advantages include a decrease in Bremsstrahlung (background), satellite peaks from the source, and an increase in the signal to background ratio. One of the main disadvantages of a monochromatic source is that the X-ray flux onto the sample is decreased. Therefore, longer acquisition times can be required.²⁸

Once the photoelectrons are ejected and have passed from the Fermi level into the vacuum, they are focused by a lens system into the analyzer. On the Kratos Axis Ultra XPS used for this dissertation, there are two different modes of operation, spectroscopy and imaging. These modes require two different analyzers. In spectroscopy mode the electrostatic hemispherical analyzer is used, as shown in Figure 3. The electrostatic hemispherical analyzer is an energy dispersive analyzer that consists of two concentric hemispheres that have voltages applied across them. A specific voltage allows photoelectrons of a particular kinetic energy, E_0 , to pass between the two hemispheres and onto an exit plane. The following equation shows the relationship between voltage and kinetic energy, E_0 .

$$\Delta V = E_0 (R_2/R_1 - R_1/R_2) \quad (3)$$

R_1 and R_2 are the radii of the internal and external hemispheres, respectively. ΔV is the potential difference across the two hemispheres. Photoelectrons that have kinetic energies greater than E_0 are focused above the exit slit, and photoelectrons with kinetic energies less than the E_0 are focused below the exit slit. In the case of a survey scan where ranges of kinetic energies are collected, the voltage across the concentric hemispheres is scanned to allow different kinetic energies to be focused on the exit slit.²⁹

The electrostatic analyzer also retards the KE of photoelectrons to the pass energy of the electrostatic analyzer. This is necessary since energy resolution is defined as $\Delta E/E$, where ΔE is the full width at half maximum of the peak (FWHM), and E is the pass

energy of the photoelectron. Therefore, a lower pass energy can provide higher resolution spectra; however, there will be a decrease in signal intensity with a lower pass energy. Pass energies typically range from 5-160 eV, depending on the type of spectra that is being acquired.

Electrons are detected by channel electron multipliers that consist of semi-conducting glass tubes that have a potential difference applied along the length. When electrons impinge upon the wall of the tube secondary electrons are released. These electrons are then accelerated by the potential difference into another wall, creating a cascade of electrons. This process is repeated until an amplification of 10^6 - 10^8 is achieved, allowing for single electron detection. The amplified current is then measured and recorded either in pulse mode or ac mode. The intensity of the photoelectrons is displayed as counts per second. Usually, a number of channel electron multipliers are used, allowing the signal to be summed for faster acquisition times.²⁹

XPS requires strict vacuum condition for analysis. One reason for this is that the photoelectrons have to be able to reach the analyzer. If an analysis was done at atmospheric pressure, a photoelectron could only travel 10^{-7} m before colliding with an air molecule. If an analysis was done at 10^{-6} torr, the photoelectron could travel 100 m before a collision would take place, making it possible for a photoelectron to reach the analyzer. This condition can be met by operating in high vacuum; however, ultra high vacuum is required for proper analysis. It is important that the surface remain unaltered for the analysis; at atmospheric pressure a new monolayer can form on the surface in 10^{-9} s. Conversely, at $< 10^{-9}$ torr it will take 10,000 s for a new monolayer to form on the

surface of the sample. Therefore, operating under ultra high vacuum conditions is important.

Charge neutralization can be critical in XPS analyses, especially for insulators. Since photoelectrons are being ejected, a positive charge can build up on the surface of the sample as a result of electron depletion. A positively charged sample surface causes the photoelectrons to leave the surface with a lower KE, causing a change in the binding energy that is calculated for a particular element. Charging will also cause peaks to broaden or split into more than one peak.³⁰

One solution to sample charging is to flood the sample surface with low energy electrons to compensate for the charged surface. One example of a charge compensation system can be found on a Kratos Axis Ultra XPS. Low energy electrons (0.1 eV) are injected to the sample surface from a filament above the sample. At the same time, a magnet below the sample creates magnetic field lines that are used to focus the photoelectrons to the analyzer. The low energy electrons follow these magnetic field lines back down to the sample to the same area from which the photoelectrons were ejected. This prevents differential charging from occurring on the analyzed area.³¹

Binding energy referencing is required to obtain accurate information about peak shifts observed in the spectra. When conducting samples are placed in contact with the spectrometer, the Fermi levels of the conducting sample and the spectrometer are at the same energy level. When this occurs, the sum of the KE and true BE does not exactly equal the X-ray energy, leading to an incorrectly calculated BE. The difference is due to the work function of the spectrometer, ϕ_{sp} . The difference is equal to the amount of

energy it takes to move the photoelectron from the Fermi level into the vacuum. In order to obtain accurate binding energies, the work function must be calibrated correctly. The binding energy scale is calibrated using Copper (Cu) and Gold (Au) by adjusting the peaks so that they appear at a standard BE.³²

Materials such as insulators lack conductivity and utilize charge neutralization to reduce the charge buildup on a surface. This allows the vacuum level of the sample to be in electrical equilibrium with electrons from the charge neutralizer. This causes a problem since the BE of the insulator now depends upon the spectrometer work function and the energy of the electrons from the charge neutralizer. In this case, an internal standard is commonly used. Carbon referencing is the most common method used, in which the Carbon 1s photoelectron peak at 285.0 eV is used as the reference peak.³³ Therefore, the hydrocarbon Carbon 1s peaks from the spectra are assigned a value of 285.0 eV to calibrate the energy scale. The hydrocarbon peak at 285.0 eV is frequently utilized since this adventitious carbon is ubiquitous in the environment. Other methods of charge calibration include deposition of a calibrant such as gold and ion implantation of rare gases.³³

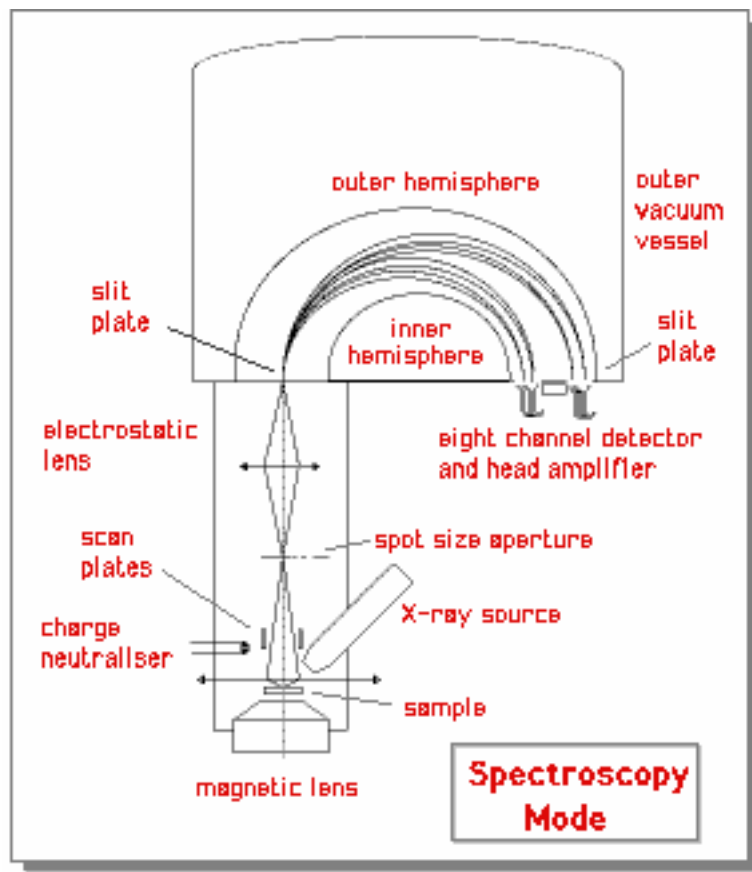


Figure 3. Kratos Axis Ultra XPS Spectroscopy mode

Analysis of a sample usually begins by taking a survey spectrum, also known as a wide scan spectrum. A survey spectrum is a low energy resolution spectrum acquired over a binding energy range of 1400 eV or less, and it is used to identify the elements that are present. The number of photoelectron peaks for each element in the survey spectrum corresponds to the number of occupied energy levels in the atom with binding energies lower than the excitation energy. The peaks are indicated by atomic notation, the name of the shell from which they were ejected, and their spin state if spin-orbit coupling occurs. Figure 4(a) is a survey spectrum of poly (methyl methacrylate) (PMMA). The axes of the spectrum are intensity in counts per second (CPS) versus binding energy given in electron volts (eV). There are three different peaks identified in Figure 4; the O 1s and C 1s peaks are core level photoemission peaks from the oxygen and carbon in PMMA. The set of peaks labeled O KLL are due to the Auger transition in the oxygen atom.

The intensity of the peaks is directly related to the concentration of the element on the sample surface, and the elements observed can be identified according to their binding energies. Looking at other peaks present in the spectrum from the same element can eliminate ambiguity in elemental identification. Several references are available for identifying elemental and chemical shifts for different elements. The Handbook of X-ray Photoelectron Spectroscopy is available from PHI.³⁴ The XPS of Polymers Database edited by G. Beamson and D. Briggs is helpful for identifying polymers and their chemical shifts.³⁵

Another feature of the survey spectra shown in Figure 4 is the step background that increases with increasing binding energy. This background arises due to inelastic

scattering of the photoelectrons; that is, the photoelectrons escape the surface with a loss in energy. As a result there is a step-like shape because the background signal is cumulative.²⁷

High-energy resolution spectra reveal more detail about the elements identified in the survey spectrum. The spectra provide chemical information pertaining to oxidation states, functional groups and concentrations. The energy differences between peaks of different chemical states are similar to the observed peak widths (~1.0 eV), and individual peaks are rarely completely separated in a spectrum. Therefore, a peak fitting routine is needed to resolve the individual peaks.

A combination of background removal, peak shape, position, height and width are used as parameters to fit each peak. Most commercially available software has a peak-fitting routine. Figure 5 is a high-resolution carbon spectrum of poly (methyl methacrylate) (PMMA). A peak fitting routine is applied, revealing the four different chemical species present. The peaks that are shown are attributed to chemical shifts due to atoms bound to the carbon. The structure of PMMA is shown as an inset; the numbers beside the carbon correspond to the numbered peak shown in the spectrum. For example, carbon 4 in the structure, the ester carbon, corresponds to peak 4 in the spectrum at a binding energy of 289 eV. This chemical shift was identified using a polymer reference book. The chemical shift of each carbon atom is affected by the element in which it is bound. The carbons bound to oxygen, peaks 3 and 4, occur at a higher binding energy; the carbons bound to carbon peaks occur at a lower binding energy. The oxygen atom, which is more electronegative than carbon, removes electron density away from the

carbon atom, giving it a slightly positive charge. This will cause the electrons to be held with more energy, resulting in a higher calculated binding energy.²⁷ Therefore, high-resolution spectra can also give information about the chemical state of the element.

The valence band region of a spectrum is the binding energy range from 0-40eV. This region of the spectrum corresponds to the valence shell electrons that comprise the outer shell electrons of an atom. The structure of the valence band is closely related to the occupied density of states.³⁶ The valence shell electrons are directly involved with bonding among the different atoms, and are thus affected by the chemical environment. Until recently, the region was underutilized due to long acquisition times needed to obtain spectral signals that are often 30 times lower than the core level spectra.³⁵ Recent advances in instrumentation now allow the spectra to be collected in a matter of minutes instead of hours. The valence band region can provide electronic structure information as well as structural information. In the case of polymers, isomers of poly iso (butyl methacrylate) were investigated by Thomas and Fulghum.³⁷ Because they are isomers they have the same molecular formula but a different structural formula. This means that there will not be a difference in core-level peak shapes. However, Figure 6 is the valence band structure for the same isomers; there are distinct differences in the peak shapes. This makes it possible to identify different structural isomers using XPS. The valence band not only plays a qualitative role in XPS, but it can also be used quantitatively. Thomas and Fulghum have used the valence band to quantify the surface composition of various polymer blends: poly (vinyl chloride)/poly (methyl methacrylate), poly (n-hexylacrylate)/ poly (n-butyl acrylate).³⁷ Since the valence band region is closely related

to the occupied density of states structure, it is also important for the study of electronic structure of materials, device applications, and verifying band structure calculations.³⁶

The most common method used for quantifying XPS results is by measuring the areas under the peaks after background subtraction. The peak areas are directly related to the concentration of a particular element or chemical species. The most common method of quantification is through the use of relative sensitivity factors (RSF). An elemental peak is assigned a value to which all the other elements are referenced. In XPS a value of 1 is assigned to the F 1s photoelectron peak. The RSF is calculated using equation 4.

$$\text{RSF} = I_A / N_A \quad (4)$$

In equation (4), I_A is the signal intensity from element A, and N_A is the area or distribution of element A within the sample surface.³⁸ The relative atomic concentration can be determined by using the following equation:

$$\% C_A = [I_A \text{RSF}_A / \sum_X (I_X \text{RSF}_X)] \times 100 \% \quad (5)$$

C_A is the atomic concentration of element A, I_X is the photoelectron intensity from element X, and RSF_A and RSF_X are the RSF's for element A and X, respectively.³⁸

Over the past ten years, manufactures have included imaging capabilities on XPS instruments. The Kratos Axis Ultra utilizes a parallel imaging system. The photoelectrons

in imaging mode pass through a spherical mirror analyzer shown in Figure 6. As the photoelectrons pass through the analyzer they maintain their spatial orientation and are detected and amplified by a microchannel plate detector. The charges detected by the microchannel plate are converted to light pulses that are detected by a CCD camera. This makes it possible to record a two-dimensional image at a fixed binding energy and pass energy. The imaging mode configuration is shown in Figure 7.

Photoelectron intensity in an image is brought about by changes in elemental or chemical state as well as surface topography. Therefore, photoelectron images can provide an elemental or chemical distribution map of heterogeneous surfaces. Image fields of view can range from $700 \times 700 \mu\text{m}^2$ to $200 \times 200 \mu\text{m}^2$ with a resolution varying from 2-20 μm depending on the magnification used. Figure 8 is an example of a high magnification ($200 \times 200 \mu\text{m}^2$) In 3d image of a patterned surface composed of alternating lines of Indium tin oxide (ITO) and polymer. The width of each line is $\sim 6 \mu\text{m}$. The color scale at the right of the image correlates the color in the image with image intensity. The more intense colors in the image are due to the presence of the Indium lines and the darker areas are where polymer is present.

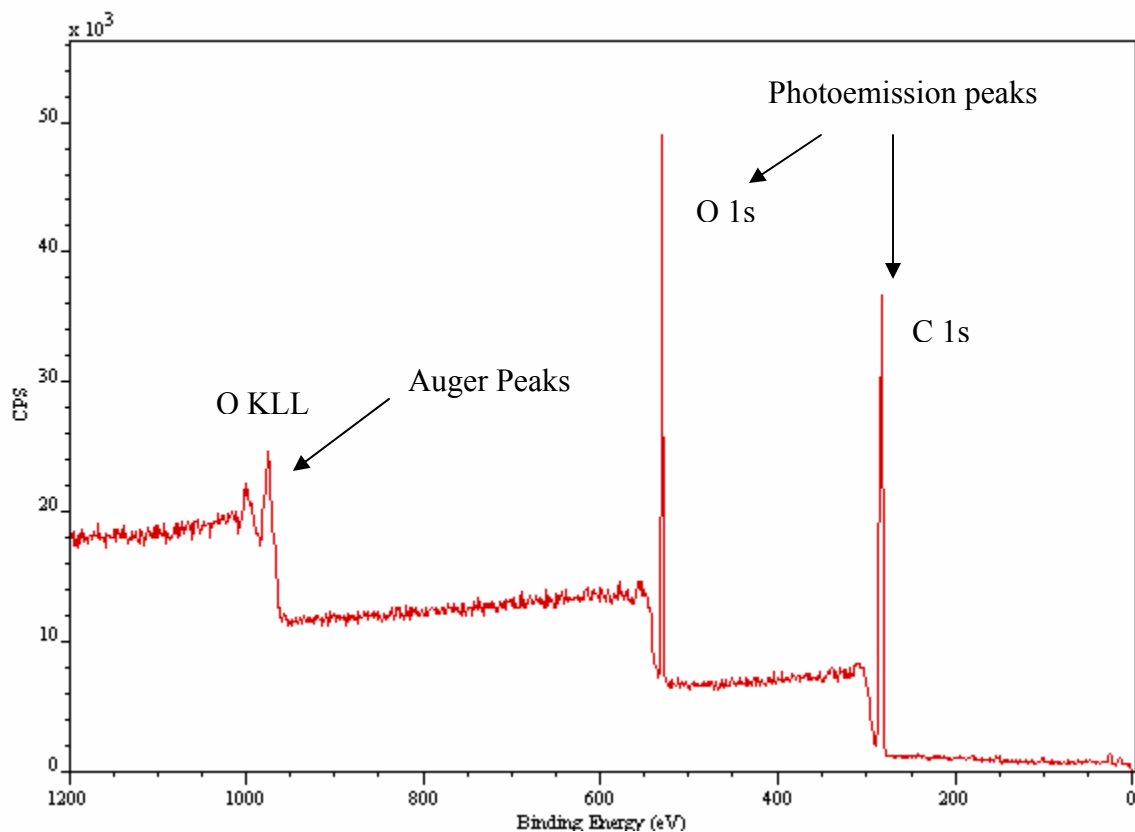


Figure 4. Example of a survey spectrum of PMMA that contains C and O.

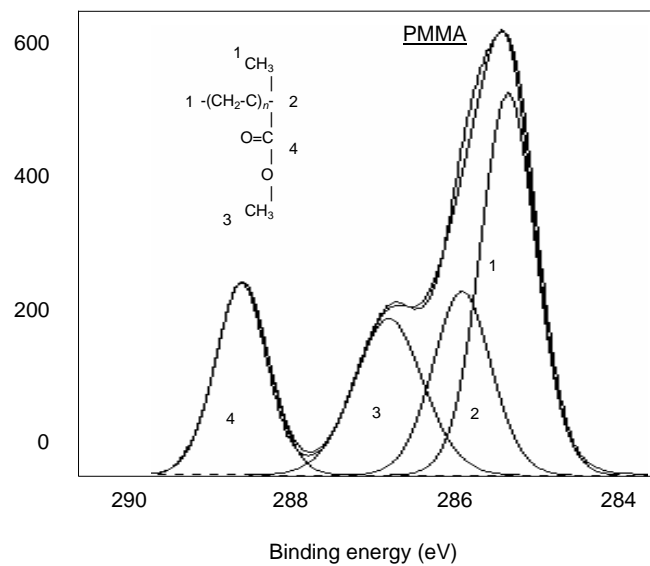


Figure 5. (a) A high-resolution carbon (C 1s) spectrum of poly (methyl methacrylate) (PMMA). A peak fitting routine was applied, revealing the four different chemical species present. The structure of PMMA is shown as an inset; the numbers beside the carbon correspond to the numbered

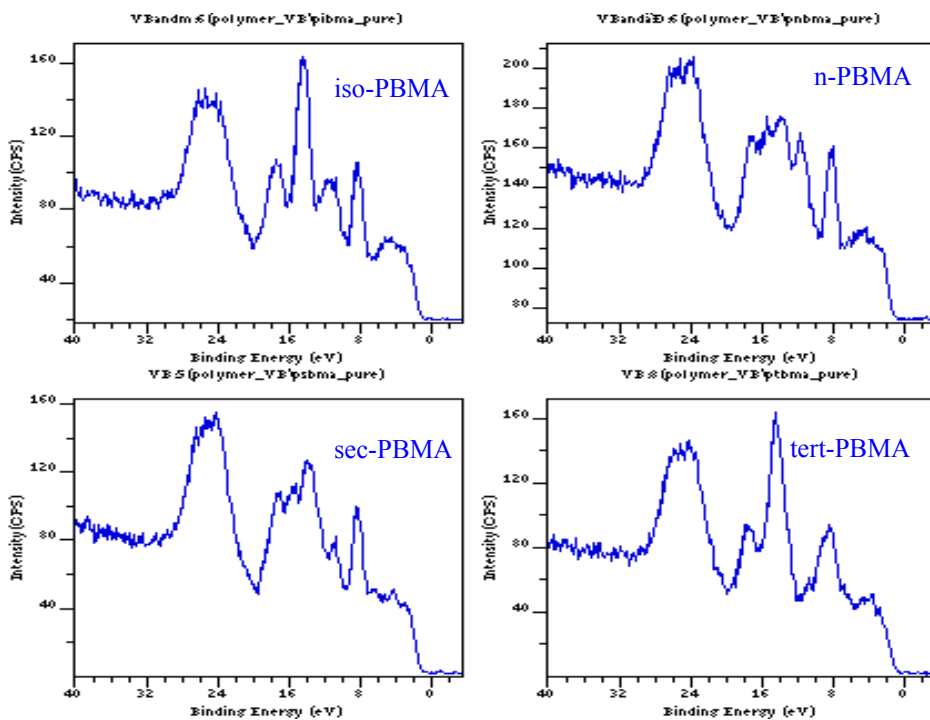


Figure 6. Valence band spectra of poly (butyl methacrylate) (PBMA) allow for the differentiation of isomers: (a) poly (iso-butylmethacrylate) (b) poly (*n*-butylmethacrylate), (c) poly (sec-butylmethacrylate), (d) poly (tert-butylmethacrylate)

Imaging XPS coupled with small area analysis can be used to obtain composition information in an area of interest in an image. Figure 9(a) is an example of point analysis taken from two different points on a $350 \mu\text{m}^2$, O 1s image of a 50:50 blend of poly (vinyl chloride)/ poly (methyl methacrylate).³ The more intense areas are enriched in PMMA; the dark areas are enriched in PVC. Figure 9(b) and (c) show small area ($55 \mu\text{m}$) survey spectra and high-resolution C 1s spectra that were acquired from points 1 and 2, respectively. The survey spectra in Figure 8(b), show that area 1 has a larger Cl 2p component compared to area 2, indicative of more PVC in region 1. The curve fit for the pure component spectra in Fig. 9(d) is used to evaluate the high-resolution C 1s spectra of the blends. When comparing the C 1s spectrum from point 1 with the pure component spectra, it can be seen that both PMMA and PVC are present, whereas at point 2 there is mostly PMMA.³

In this dissertation, XPS is used to image a patterned sample of polymer on indium tin oxide; phase separated blends of poly (vinyl chloride)/ poly (methyl methacrylate), fluorescein-labeled poly (styrene)/ poly (butadiene), and poly (styrene)/ poly (methyl methacrylate); and a $9 \mu\text{m}$ diameter fluorescein-labeled poly (styrene) bead.

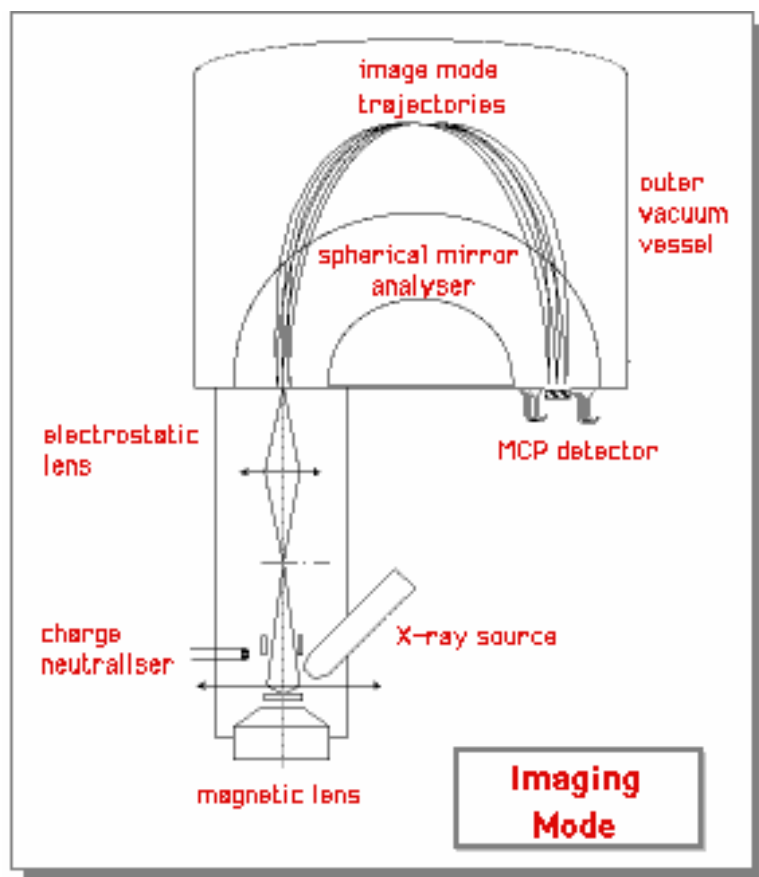


Figure 7. Kratos Axis Ultra XPS Imaging mode

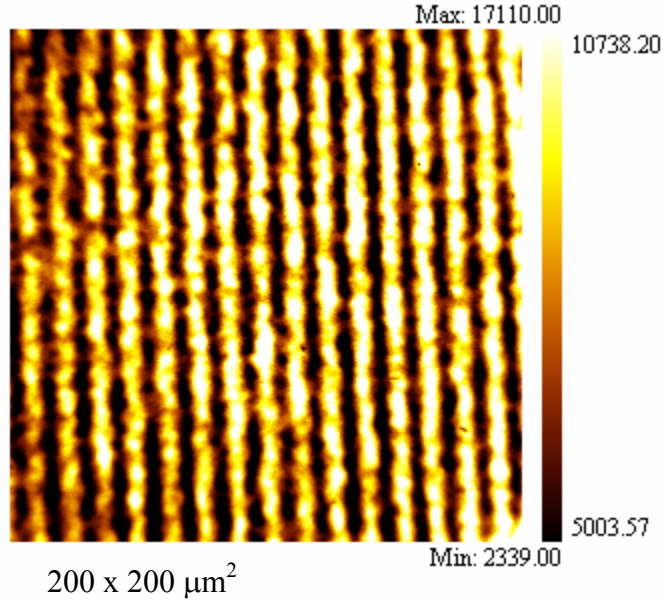


Figure 8. Example of a high magnification image of a patterned surface composed of alternating lines of Indium Tin Oxide (ITO) and polymer. The intensity is due to the Indium in the substrate, ITO.

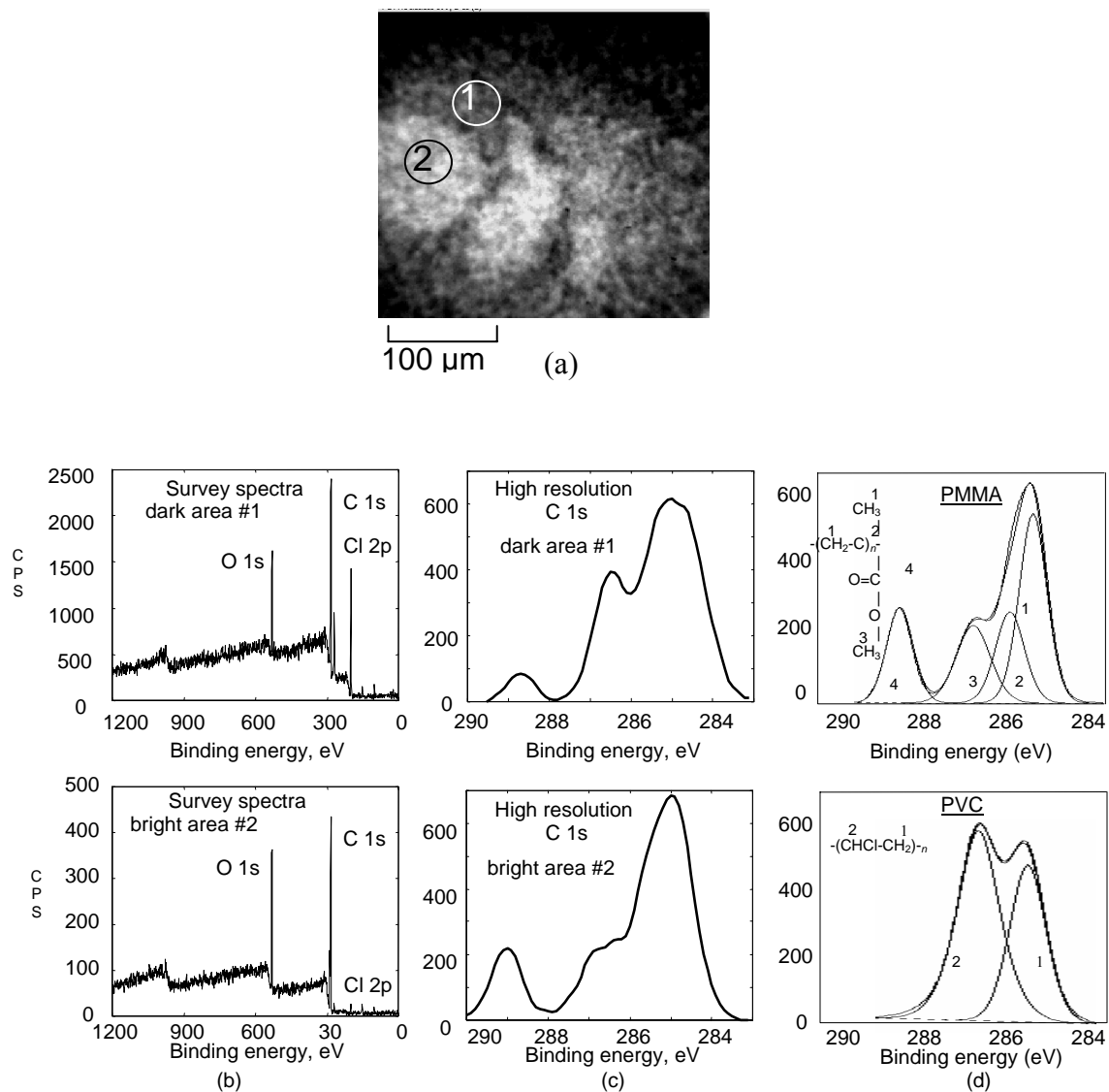


Figure 9. (a) A $350 \mu\text{m}^2$ C 1s image of a 50 % PVC : 50 % PMMA blend (b) Small area ($55 \mu\text{m}$ diameter) survey spectra from points 1 and 2. (c) High resolution C 1s spectra from points 1 and 2 (d) High resolution C 1s spectra of pure PMMA and PVC

Atomic Force Microscopy

The atomic force microscope (AFM) was invented by Binnig, Quate and Gerber in 1986.³⁹ It has become a useful technique for imaging surfaces from the micron scale down to the atomic scale and for measuring forces on the nano-Newton scale. AFM has been used to image many different surfaces, including biological molecules, polymeric samples, and semiconductor nanostructures.⁴⁰ In addition, AFM has been used to measure and map a variety of surface properties, including adhesion, stiffness, electrical potential, and temperature.⁴⁰ The AFM does not require the sample to be conducting, as is the case with the scanning tunneling microscope (STM), and extensive sample preparation is not required.

The AFM consists of a cantilever that has a reflective coating (silicon, gold or aluminum) on the back and a sharp tip (2-20 nm) at one end of the cantilever. A diode laser is focused onto the back of the reflective cantilever. As the cantilever is scanned across the surface, moving up and down with the sample topography, the laser beam is deflected off the cantilever onto a four quadrant positional photodetector. The force, F, between the tip and sample leads to deflection according to Hooke's Law for small displacements:

$$F = -kz \quad (6)$$

k is the spring constant of the cantilever and z is the vertical displacement of the cantilever from equilibrium. The detector response is linked to the piezoelectric crystal

by a feedback loop telling the piezo to move either up or down according to the topography of the surface. Figure 10 shows a typical set-up for the Atomic Force Microscope. Several different modes of imaging are available for AFM, including contact mode, non-contact mode and tapping mode. Contact mode and tapping mode will be discussed in more detail since they were used in this research.

Van der Waals forces are responsible for the deflection of the cantilever. Figure 11 is an interatomic force versus distance curve. Moving from right to left, the distance between the tip and sample decreases. Initially, the tip responds to the weak attractive van der Waals forces. As the interatomic distance between the tip and sample decreases, there is a repulsive force due to the interaction of electron clouds from the tip and sample. The attractive forces weaken as the separation distance decreases. The attractive force then goes to zero when the distance between the tip and surface is a few angstroms. When the van der Waals forces are positive, the atoms in the tip and sample are in contact.⁴¹ Each AFM mode operates in a different regime along the van der Waals curve leading to various advantages and disadvantages for each mode of operation.

In contact mode, operating in the repulsive region of the van der Waals curve, the deflection of the cantilever is kept constant, thus the force exerted on the surface is constant. As the tip is scanned across the sample, surface features cause deflection of the cantilever. The feedback loop acts to maintain a constant deflection by moving

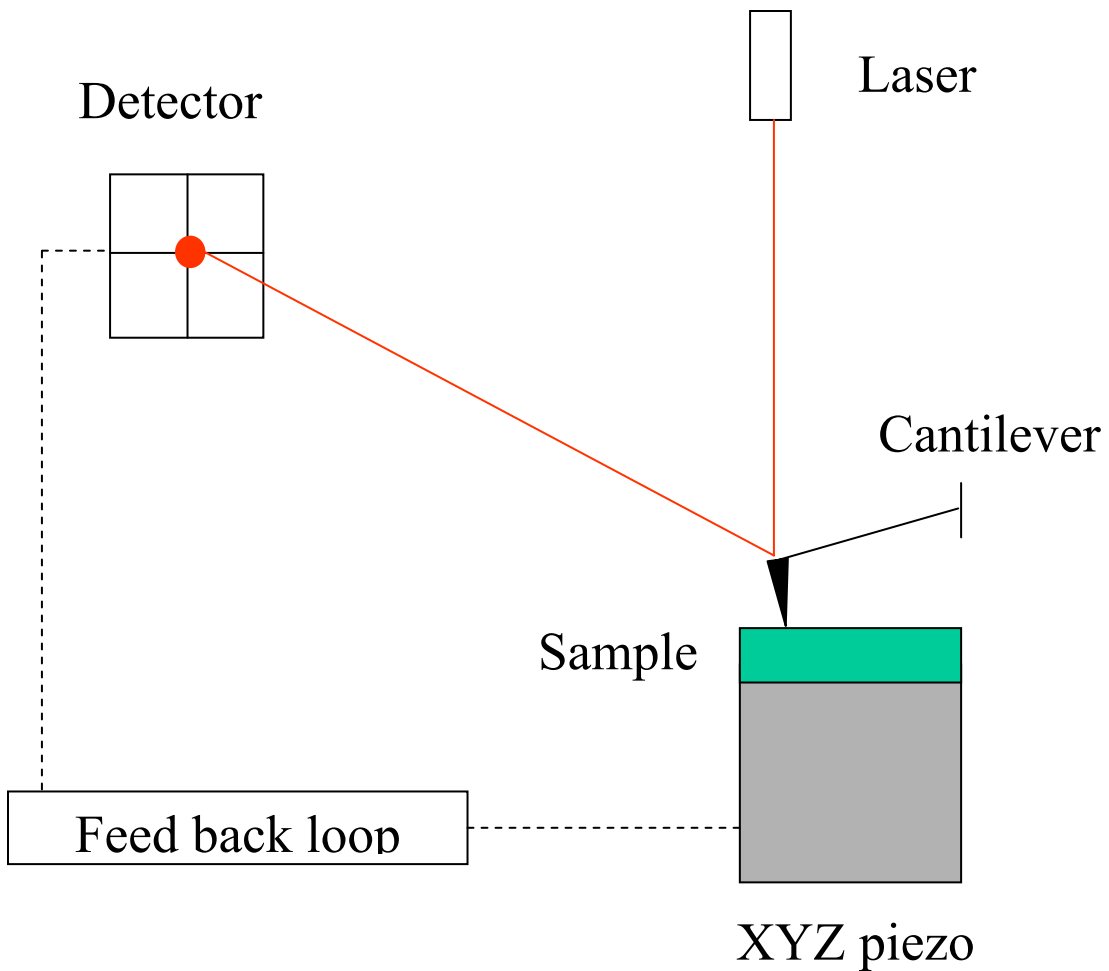


Figure 10. A typical set up for Atomic Force Microscopy (AFM) is shown above.

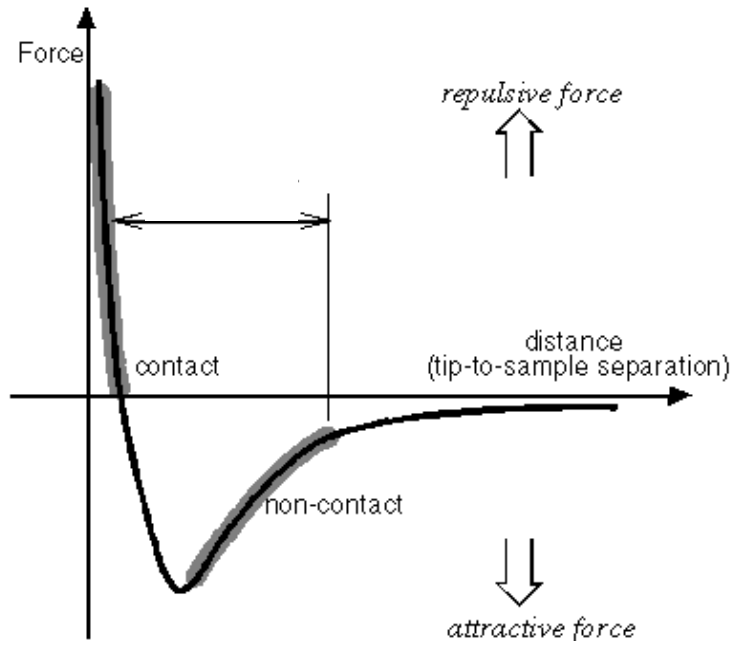


Figure 11. A force versus distance curve illustrating the interaction potential between an AFM tip and the surface. Tip-sample distance decrease from left to right. Two different imaging regimes are noted in the figure, contact and non-contact. Contact mode AFM operates in the region marked contact along the curve, and tapping mode AFM operates in both the contact and non-contact regions of the curve as the tip oscillates on and off the surface.

the piezo in the z direction according to the surface features. The main disadvantage of contact mode AFM is the lateral forces imparted to the sample while scanning. These forces can lead to tip-induced damage of the sample surface, making it difficult to accurately image soft surfaces, such as polymers. Additionally, the adsorbed water layer found on most surfaces under ambient conditions acts to increase the forces exerted on the sample by the tip due to capillary forces.⁴² This has the tendency to damage the sample and worsen the resolution of the image.

Since contact mode is not suitable for imaging soft surfaces, the methodology for another technique came about by studying the problems that emerged during the scanning process in contact mode AFM.⁴³ This led to the development of AFM lithography. In AFM lithography the tip is used as a mechanical tool to physically scribe or indent the surface. By applying large forces to the tip, patterns can be created on substrate surfaces by controlling the tip movement.

In tapping mode, which operates in both the attractive and repulsive regimes, the cantilever oscillates at or near its resonant frequency (50-500 kHz), and the tip strikes the surface on each oscillation. A feedback loop acts to maintain constant amplitude of tapping by measuring the RMS value of the deflection detector signal and constantly comparing it with the predetermined set point value.⁴² A topographical image can be generated by scanning an area while the feedback loop maintains a constant oscillation amplitude. For example, if the oscillating tip moves over a valley, the oscillation amplitude increases and the feedback loop acts to decrease the amplitude to the set point value by moving the tip down. If the tip moves over a hill, the oscillation amplitude is damped and the feedback

loop moves the tip up to maintain the set point amplitude. If the changes in z direction are plotted as a function of the x and y coordinates, a topographical image is generated.

In tapping mode, when the tip comes in contact with the surface at a high oscillation frequency (50-500 kHz), the surface becomes viscoelastic, and the tip-sample adhesion forces become greatly reduced. The tapping motion of the tip provides enough energy to overcome the attractive capillary forces due to the water layer present on the surface.⁴² In addition, the shear forces are eliminated since the tip taps the surface and then moves laterally, unlike contact mode AFM, which is in constant contact with the surface while scanning. The amount of time the tip spends in contact with the sample in tapping mode is significantly less than in contact mode, minimizing damage to the surface.⁴⁴ These advantages make tapping mode AFM amenable to soft samples such as polymers and biological samples.⁴⁵

Phase imaging is an extension of tapping mode that provides significantly more contrast than the topographic image alone; it is useful in identifying surface composition variations on a sample surface. When the oscillating tip is scanned across the surface, not only will the cantilever deflection amplitude change, but also the cantilever will oscillate at a frequency that lags that of the excitation frequency. As the tip moves over heterogeneous features on the surface, the phase lag will be different for different features, as shown in Figure 12. A lock-in amplifier can be used to extract the phase information.⁴⁵ The phase lag measured is related to adhesive forces, viscoelastic properties, and the elastic modulus of the sample only if there are

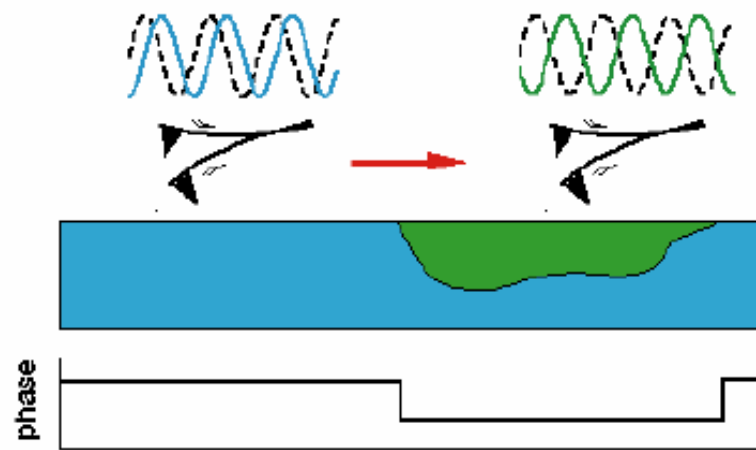


Figure 12. Figure 3 shows the phase lag observed between the frequency at which the tip is being driven to oscillate and its response as the tip moves over surface compositional variations. This phase lag can be mapped to show the location of these variations on a surface.

tip-sample inelastic interactions.^{22-26,46} Phase shifts in the absence of inelastic interactions are independent of the value of the elastic modulus. Phase shifts associated with elastic properties arise if a fraction of the cantilever's kinetic energy is dissipated into the sample.⁴⁷ This leads to the most widely accepted interpretation of phase images as energy dissipation images in which the amount of energy dissipated depends on the stiffness of the sample and cantilever, the natural frequency, the quality factor of the cantilever, and the oscillation amplitudes. It has been shown that there is proportionality between the sine of the phase lag and the energy loss observed.²⁴ Figure 13 (a) and (b) are AFM topography and phase images, respectively, of a 50:50 blend of poly(styrene) and poly(butadiene). In the phase image the different constituents of the polymer blend on the surface can be distinguished. Note that there is a difference in contrast between the topography and phase images.

The lateral resolution of the atomic force microscope is largely dependent upon the radius of curvature of the tip. The radius of curvature of an AFM tip can range from 1-20 nm. Images acquired are a convolution of the tip and the feature being imaged. As long as the tip is sharper than the feature being imaged, the true profile of the image is represented. However, if the feature is sharper than the tip, the shape of the tip will dominate the image. Under normal imaging conditions, the resolution is on the order of a few nanometers, depending on the tip radius. Under special conditions, atomic resolution has been observed. In this case it is believed that a single atom at the apex of the tip interacts with the surface during imaging to reveal atomic resolution images.⁴⁷ The vertical resolution for AFM is ~ 0.1 Angstroms, and it is limited by the thermal noise of

the cantilever. Other factors that can affect the resolution include the imaging mode, scan speed, feedback loop design and vibration isolation.

In this dissertation research, AFM is used to obtain topography and phase images of a patterned sample of polymer on indium tin oxide; phase separated blends of poly (vinyl chloride)/ poly (methyl methacrylate), fluorescein-labeled poly (styrene)/ poly (butadiene), and poly (styrene)/ poly (methyl methacrylate); and a 9 μm diameter fluorescein-labeled poly (styrene) bead. In addition, AFM was used to mark analysis areas for obtaining multi-technique, correlated data acquisition.

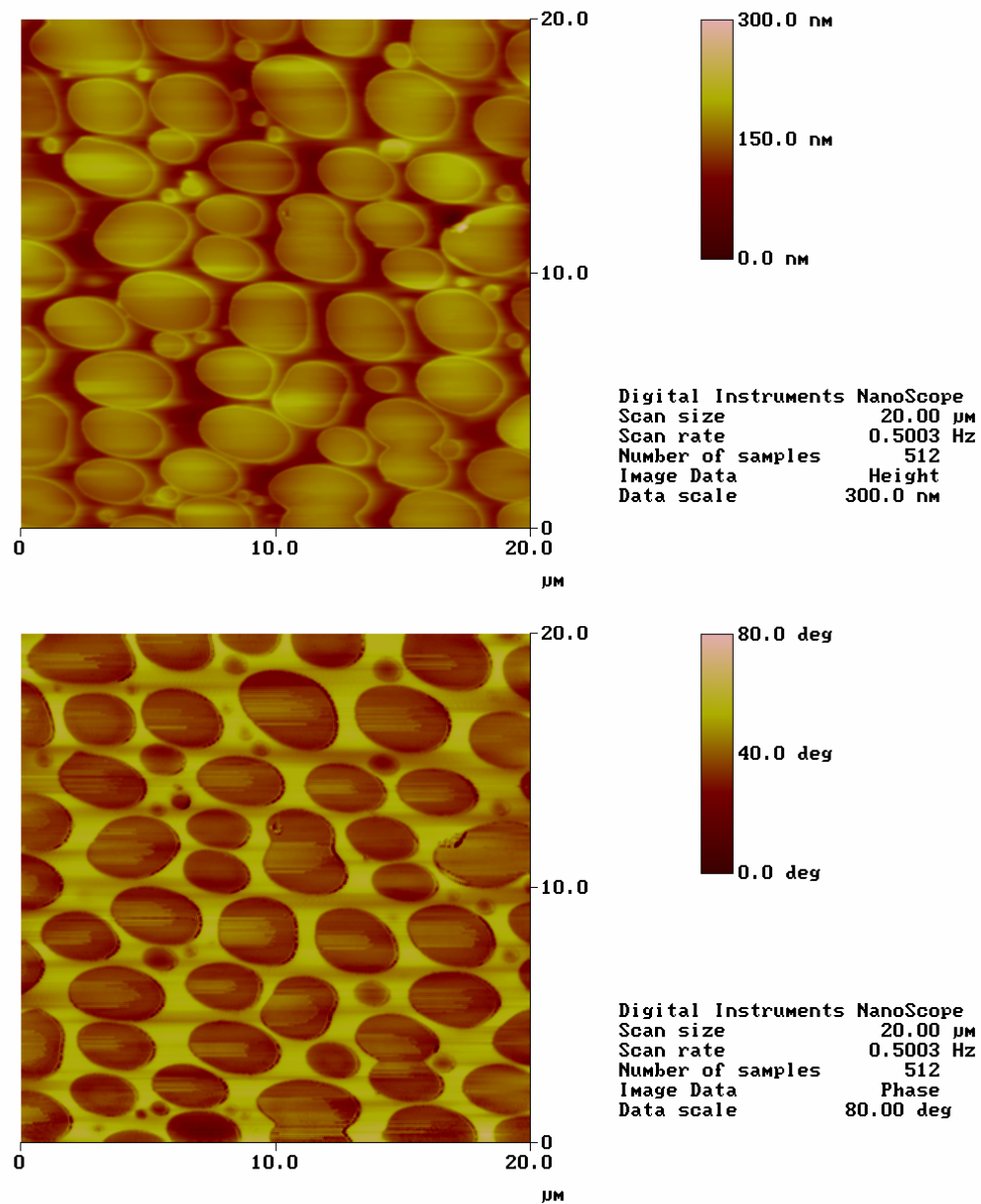


Figure 13. An AFM (a) topography and (a) phase image of a 50:50 blend of poly(styrene) and poly (butadiene)

Laser Scanning Confocal Microscopy

The laser scanning confocal microscope (LSCM) is used to optically section up to 10-50 μm through samples that fluoresce or contain a fluorescing component. This enables visualization within the sample and the ability to collect sharply defined optical sections from which a three-dimensional volume can be created. Marvin Minsky developed the principle of the confocal microscope in 1957, after determining that the ideal microscope should observe the amount of light reflected or transmitted at each point on a sample.⁴⁸ If intensities from all of the points were obtained simultaneously, the resolution would be lowered due to the contribution of adjacent, out-of-focus light, leading to blurring. Minsky introduced the idea of apertures to limit the area of light illumination on the sample and to limit the detection area. Since the data is to be obtained point-by-point, the entire sample is to be scanned, leading to increased acquisition times.⁴⁸

In the conventional fluorescence microscope, fluorescence occurs throughout the volume of the sample and lowers the resolution of the features detected from a particular focal plane. For thicker samples, greater than 2 microns, there is a high degree of fluorescence emission coming from within the depth of the sample further limiting the spatial resolution.⁴⁸ Confocal microscopy alleviates some of these problems by excluding fluorescence from areas that are not within the focal plane. Therefore, LSCM provides a marginal increase in resolution in the lateral (xy) and axial (z) directions. However, the

primary advantage of LSCM is the ability to optically section through a fluorescing sample non-destructively.

A common set up is shown in Figure 14.⁴⁹ A laser passes through a pinhole aperture and is reflected off a dichroic mirror. The laser beam then passes through the objective lens and into the sample. The sample usually contains a fluorescing component, such as Fluorescein, which has excitation and emission wavelengths of 494 nm and 518 nm, respectively. Fluorescein is used in the analyses of polymer blends in this dissertation. The fluorescence from the fluorescein passes out of the sample, through the objective lens and dichromatic mirror. The light then passes through another pinhole aperture and is detected by a photomultiplier tube. The laser is rastered across the sample point-by-point to generate a confocal image. In this research, an argon ion laser that emits at 488 nm is used to excite the Fluorescein.

The pinhole aperture that sits in front of the photo multiplier tube is the heart of the instrument. Only fluorescent light from a narrow focal plane reaches the detector. Fluorescent light from objects above and below the focal plane is excluded as is any out of focus light is excluded.

Refocusing the objective in a confocal microscope shifts the excitation and emission points on a specimen to a new plane that becomes confocal with the pinhole apertures of the light source and detector. A motor driven control stage allows the objective to be moved up or down, allowing for depth studies. The images acquired can then be put together to create a three-dimensional volume.

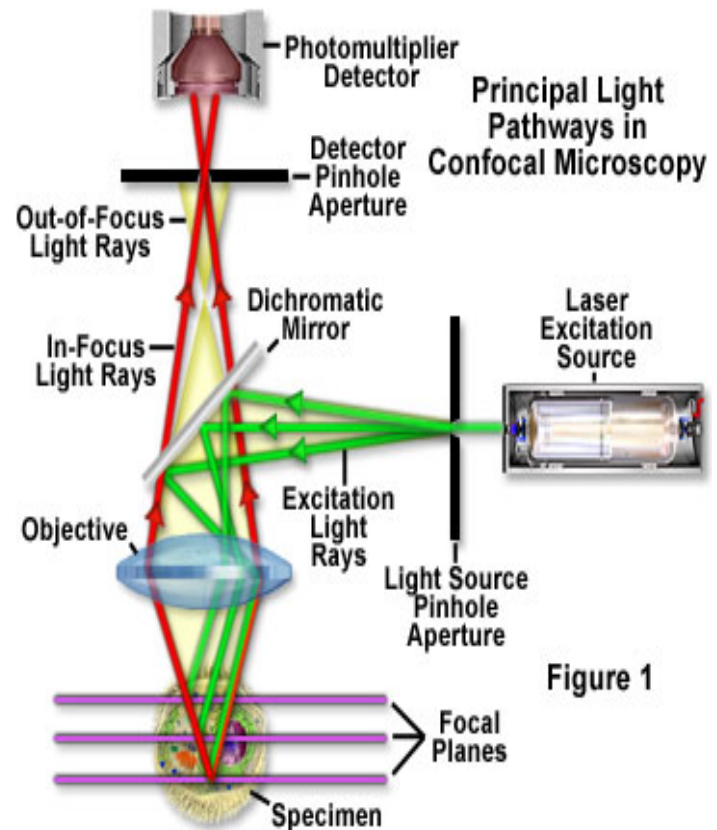


Figure 14. Instrumental set up for the laser scanning confocal microscope

The lateral resolution, the minimal resolvable distance d between two points in the xy horizontal plane for the confocal microscope, can be approximated by the following equation:

$$d_{x,y} \approx 0.4\lambda/NA \quad (7)$$

where λ is the wavelength of radiation and NA is the numerical aperture of the objective. Values can range from .3 μm to 2 μm , depending on the sample properties, wavelength of light, and the lenses used. This is a mild improvement over the $0.61\lambda/NA$ resolution for a typical optical microscope. The resolution in the axial directions (z-axis) for the confocal microscope can be approximated as:

$$d_z \approx 1.4\lambda\eta/NA^2 \quad (8)$$

η is the index of refraction. Values for the depth resolution can range from .4 μm to 1.5 μm , depending on the refractive index, wavelength of light used, lenses used and the sample properties.

The primary advantage of LSCM over the conventional microscope is the ability to section through samples optically, rather than physically. Optical sectioning allows for images to be taken at different depth throughout the sample. This simplifies sample preparation and makes the technique non-destructive. The stack of images collected can then be used for three-dimensional visualization using 3-D rendering software.⁴⁹

LSCM also has the ability to eliminate out of focus light from planes above and below the focal plan, allowing for improved image contrast.⁵⁰ Therefore, confocal microscopy is particularly well suited for examination of thick specimens where out-of-focus light would obscure details using conventional microscopy. With the use of fluorescent tagged polymers, naturally fluorescent molecules and dyes, LSCM has found use in investigating the structures of polymer blends.^{51,52} Figure 15 is a laser scanning confocal microscope image of fluorescein-labeled polystyrene spheres with a diameter of 9 μm . Figure 16 is a laser scanning confocal microscope image of fluorescein-labeled polystyrene/poly methyl methacrylate blend.

In this dissertation LSCM is used to obtain fluorescence images from blends of fluorescein-labeled poly (styrene)/ poly (butadiene), poly (styrene)/ poly (methyl methacrylate), and a 9 μm diameter fluorescein-labeled poly (styrene) bead.



Figure 15. A $308 \times 205 \mu\text{m}^2$ laser scanning confocal microscope image of fluorescein labeled polystyrene spheres with a $9 \mu\text{m}$ diameter.

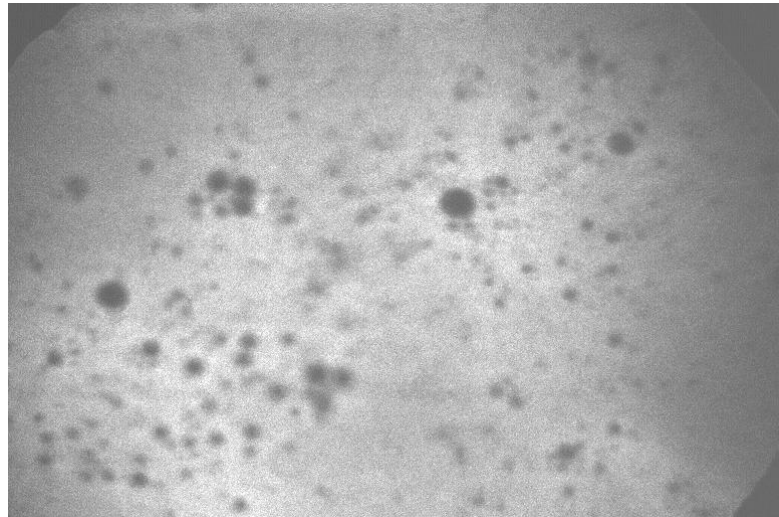


Figure 16. A $308 \times 205 \mu\text{m}^2$ laser scanning confocal microscope image of fluorescein labeled polystyrene/poly methyl methacrylate blend.

Technique Summary

Table 1 provides a brief comparison of imaging XPS, AFM and LSCM. XPS gives semi quantitative elemental and chemical information from the top 10 nm of a surface. In addition, imaging XPS provides an elemental or chemical distribution map of the surface with a lateral resolution of 2-5 μm . The main disadvantage of imaging XPS is the low lateral resolution compared to AFM.

AFM provides nanometer lateral resolution imaging of relatively smooth surfaces (features < 6 μm in height). In addition, phase-contrast AFM can provide phase images showing surface composition variations; however, there is no direct chemical information obtained from AFM, making interpretation of phase images difficult.

LSCM can optically section through a sample non-destructively to provide 2-D and 3-D fluorescence intensity maps from a sample that fluoresces or contains a fluorescing component. One disadvantage, however, is that quantification from the fluorescence intensity directly from LSCM is not possible. The lateral resolution for LSCM is 0.3-2 μm .

The chemical information obtained from XPS, combined with the nanometer resolution images obtained from AFM, and the optically sectioned images from the bulk with confocal makes these three techniques ideal for the non-destructive, 3-D characterization of heterogeneous polymer samples.

Table 1. Technique Summary

	Imaging XPS	AFM	LSCM
Signal	Photelectrons	surface properties associated with topography, adhesive forces, viscoelasticity and the elastic modulus	Fluorescence
Lateral Resolution	2-5 μm	nanometers	0.3-2 μm
Sampling Depth	10 nm	Topography	0.2 μm increments
Field of View	700x700 - 200x200 μm^2	< 150x150 μm^2	< 400x300 μm^2
Depth Profiling	Yes, over the top 2-20 atomic layers; greater depth requires sputtering	No	10-50 μm through a sample
Information	elemental and chemical state	topography/phase images	2-D and 3-D fluorescence intensity maps
Quantification	Yes	No	No
Destructive	No	No	No
Sample Requirements	vacuum compatible materials; flat samples best	smooth surface; features <6 μm in height	sample has to fluoresce or contain a fluorescing component
Primary Advantage	interpretable chemical characterization	high spatial resolution	non-destructive depth profiling
Complications	poor spatial resolution relative to AFM	interpretation of phases in phase-contrast AFM images	no quantification from fluorescence intensity, blurring of images

CHAPTER 3

IMAGE PROCESSING AND MULTI-TECHNIQUE CORRELATION AND FUSION

Introduction

Images are commonly acquired in digital format in which the data is represented spatially as pixels, with each pixel having a discrete brightness level. With the introduction of so many digital image-based techniques, new methods for image analysis are in constant demand. Digital image processing is the treatment of digital images and includes preprocessing, image enhancement and classification.⁵³ In this dissertation, image processing is used as a means to enhance interpretation, quantify images, correlated images from different techniques, and to fuse images. Different image processing techniques used in this dissertation are discussed below.

Median Filtering

A median filter is a non-linear filter commonly used as a smoothing routine for images. It is a sliding window filter in which the center of the kernel takes on the median brightness value of all the pixels covered by the kernel. The median filter requires an odd kernel size to be chosen over which to smooth the data. The odd kernel size ensures that

there is a central pixel, which will be modified by the filter operation. The advantage of the median filter over other filters (e.g. mean filter) is that it is a more robust average than the mean filter, and so a single unrepresentative pixel in a neighborhood will not affect the median value significantly. Since the median value must actually be the value of one of the pixels in the neighborhood, the median filter does not create new unrealistic pixel values when the filter is near an edge. For this reason the median filter is much better at preserving sharp edges than the mean filter. Edge preservation is important in image analysis in which objects are recognized by their outlines. A median filter is used to deresolve AFM images in Chapter 4.

Image Classification

The intent of the classification process is to categorize all pixels in a digital image into one of a fixed number of classes.⁵⁴ These classes have similar physical or chemical characteristics. The different labels are obtained by finding similarities between pixels or a group of pixels. Commonly, these classes are represented as different colors within the image. The result is a phase map image that shows the distribution of a particular phase or pixel.

The K-means unsupervised classification algorithm method is used for the research in this dissertation. In K-means unsupervised classification, statistical means are used to group data into their natural classes, however it is the task of the user to interpret the classes afterwards.

Since clustering is a pixel similarity based measurement, a method must be chosen to evaluate the similarity of two pixels. The Euclidian distance is a commonly chosen similarity measurement. In this calculation the pixel intensities are represented as vectors. In the Euclidian distance, d_{ij} , equation below, V_i and V_j are two pixels representing two vectors and N is the number of grayscale values.

$$d_{ij} = \frac{1}{N} \left[\sum_{n=1}^N |V_i - V_j|^2 \right]^{\frac{1}{2}} \quad (9)$$

The K-means method assumes that the final number of classes is known *a priori*. It is an iterative approach in which each iteration is composed of three steps. In the first step the location of the centers of the clusters is calculated. In the second step, the pixels are classified according to the nearest neighbor rule: pixel i is associated to class k if $d(i, k) < d(i', k)$, $k' \neq k$, where d is the distance between pixel i and the center of class k .⁵⁵

For the third step, if at least one pixel has been moved from one class to another during the second step, the second step is repeated, if not, the coordinates of the class centers are re-computed according to the results of the previous classification and the process is continued starting at step two.⁵⁵

After classification, post classification statistics is applied to the images to calculate the percent of the image each class, represented by a different color, occupies.⁵⁶

Figure 17 is an example of image classification. A gray scale Atomic Force Microscope (AFM) image of a 75:25 blend of PMMA/PVC is shown in Figure 17(a).

After image classification, shown in Figure 1(b), the image is represented by two colors, red and green. The percent surface coverage of the two colors is shown below the image. Image classification is utilized in the correlation of AFM and XPS images in Chapter 4.

Fractal Analysis of Images

Fractals are disordered systems whose disorder can be described in terms of a non-integral dimension. By definition, a fractal is a geometric shape that is self-similar and is a set for which the Hausdorff-Besicovitch (fractal), D , dimension exceeds the topological dimension, D_{top} . If D is equal to the topological, D_{top} , ($D_{\text{top}} = 0$ for a set of disconnected points; $D_{\text{top}} = 1$ for a curve; $D_{\text{top}} = 2$ for a surfaces and planes, $D_{\text{top}} = 3$ for spheres and other finite volumes), the system is called Euclidean. If a surface is fractal then the fractal dimension is $2 \leq D \leq 3$. The larger D is, the more disordered the surface is. If $D = D_{\text{top}}$, it is weakly disordered; if $D > D_{\text{top}}$, it is strongly disordered.⁵⁷

One method of calculating the fractal dimension is the box counting method.⁵⁸ In the box counting method an array of 3-dimensional cubes is superimposed on the surface image so that the cubes completely cover the surface. The size s of the cubes is varied and the number of cubes $n(s)$ intersected by the surface is recorded for every value of s . A double logarithmic plot of the number of cubic cells $n(s)$ used to cover the surface as a function of cell size is plotted. The fractal dimension is obtained from the slope of the plot.⁵⁸ The box counting method in the Digital Instruments software⁵⁹ was used to calculate the fractal dimension of various PMMA/PVC blends as discussed in Chapter 3.

Histogram Equalization

An image can be represented as a histogram by plotting the number of pixels with a given intensity value versus the intensity values. The goal of histogram equalization is to improve contrast and to obtain a uniform histogram by redistributing the intensity distributions. Histogram equalization will not flatten a histogram. For example, if the histogram of an image has many peaks and valleys, it will still have peaks and valleys after equalization, but the peaks and valleys will be shifted. Histogram equalization allows subtle intensity differences in a region to become resolved more easily. An example of histogram equalization is shown in Figure 18. The computer software ENVI⁶⁰ is used to histogram equalize 8-bit, gray scale AFM and Confocal images prior to image registration in Chapter 5.

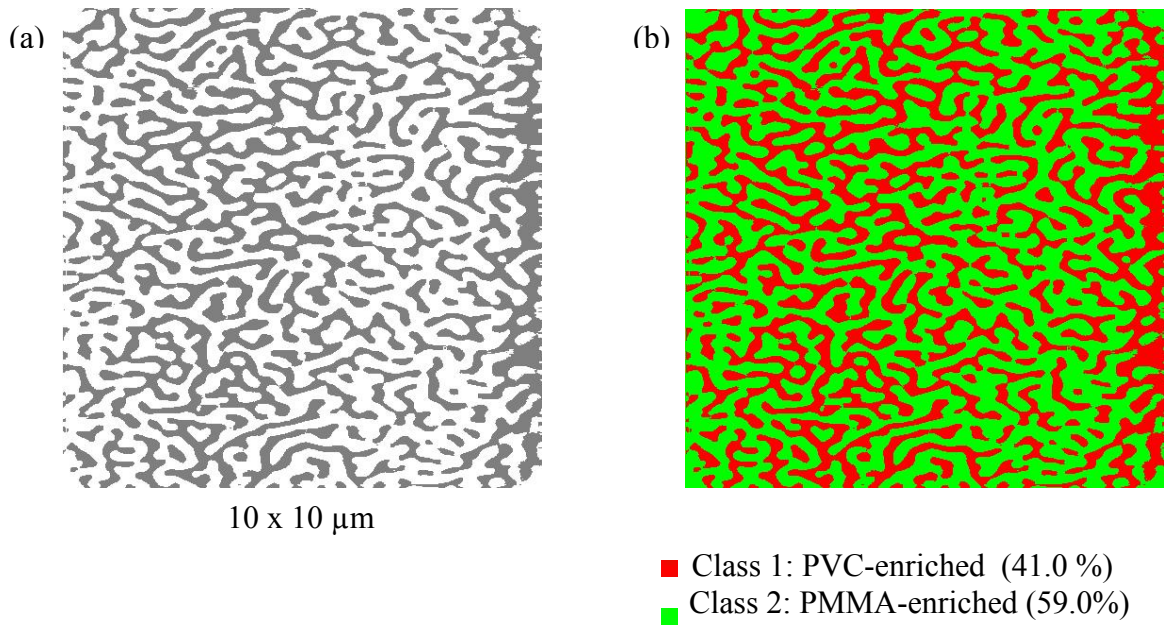


Figure 17. (a) A gray scale AFM topography image of a 75:25 blend of PMMA/PVC prior to image classification. (b) The AFM topography image after image classification. Two colors represent two different phases on the surface, red and green. Below the image are the post-classification statistics showing the percent surface coverage for each chemical phase.

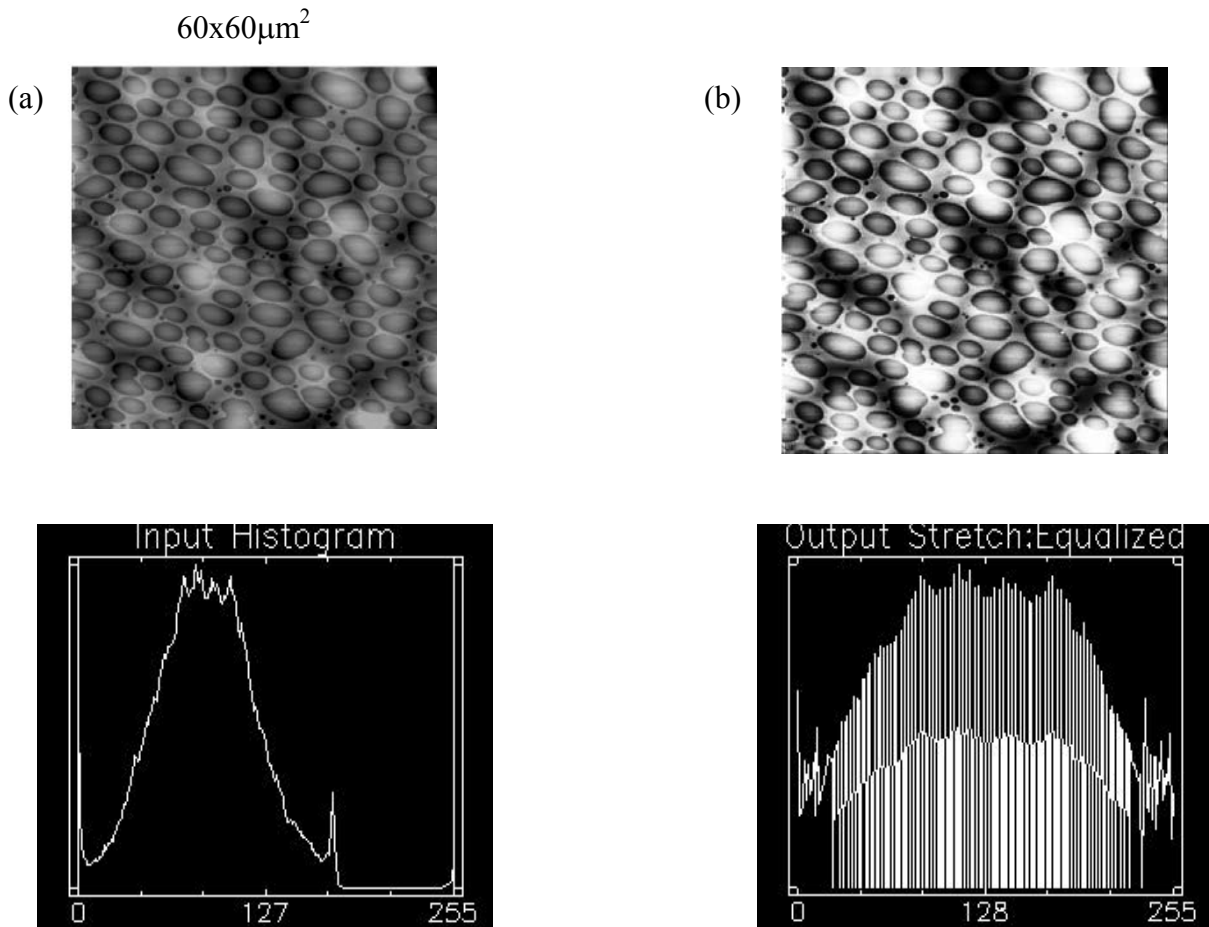


Figure 18. (a) A gray scale AFM topography image of a 50:50 blend of fluorescein-labeled poly(styrene) and poly(butadiene). Below the image is the image histogram (b) The AFM topography image after histogram equalization. Below the image is the equalized histogram of the image.

Image Registration

Image registration is used to establish a spatial correspondence between two images; it is the geometric alignment of corresponding pixels from two images. One concept that was introduced in the medical imaging field for multi-technique image registration is the idea of mutual information (MI).⁶¹⁻⁶⁴ MI is a pixel intensity measure based upon the assumptions that similar features in two different images will have similar gray values for all corresponding points in a specific region and that the variance of the ratio of gray values for corresponding points is minimal.⁶² Qualitatively, the idea is to maximize the amount of shared information between two images or it can be thought of as reducing the amount of information in a combined image. This means that there must be a way to measure the information from the images directly. A common measure of information is the Shannon-Wiener entropy measure H , which comes from the field of information theory.⁶²

$$H = -\sum_i p_i \log p_i \quad (10)$$

H is the average amount of information given by a set of symbols, i , whose probabilities are given $p_1, p_2, p_3, \dots, p_i$. If all the symbols have an equal probability of occurring, entropy will have a maximum value. The entropy will be at a minimum if the probability of one symbol occurring is 1 and the probabilities for all the other symbols are 0.

Joint entropy is a measure of information that is given from two combined images, A and B. The joint entropy H (A, B) is given by:

$$H(A, B) = -\sum_a \sum_b p_{AB}(a, b) \log p_{AB}(a, b) \quad (11)$$

If images A and B are unrelated, the joint entropy will be the sum of the entropies of the individual images. If A and B are not independent of each other, the joint entropy will be lower. Hill et al used the concept of a joint histogram as an aid to visualization of this concept.⁶² A joint histogram is a two dimensional plot of the combination of gray values in each of the two images for corresponding points for a particular image translation and rotation. When alignment is achieved, that is, image B as been transformed with respect to image A so that corresponding pixels overlap, the joint histogram will show clusters for the gray values for the overlapping features. Joint histograms for various alignments are shown in Figure 19.

For valid image registration to take place, the marginal entropies have to be considered. The marginal entropies take into account the information contributed to the overlapping volume by having each image registered, as well with the joint information.⁶⁵ This avoids situations in which only an area of background overlaps for two images, leading to images that appear registered according to the joint histogram, but are in fact mis-registered. The marginal entropies are the entropy of the individual images being registered, given by:

$$H(A) = -\sum_a p_A(a) \log p_A(a) \quad (12)$$

$$H(B) = -\sum_b p_B(b) \log p_B(b) \quad (13)$$

In equation (13), p_A and p_B are the marginal probability distributions of images A and B, respectively. If there are two images A and B, the mutual information $I(A,B)$ of the image is defined as

$$I(A, B) = H(A) + H(B) - H(A, B) \quad (14)$$

$H(A)$ and $H(B)$ are the marginal entropies of the separate images and $H(A,B)$ is the entropy of the joint image. Therefore, two images are registered when the joint entropy is minimized and the marginal entropies, $H(A)$ and $H(B)$ are maximized. To perform image registration, a program was written in MATLAB.⁶⁶

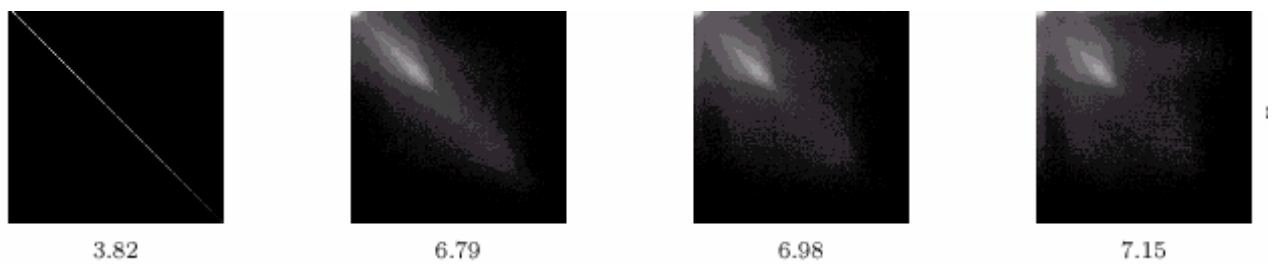


Figure 19. (a) A two dimensional histogram where each axis is the number of possible grayscale values in the image. Each entry is the number of times an intensity a in one image corresponds to an intensity b in the other. The first image shows a two dimensional histogram for the perfect alignment of two images and the corresponding joint entropy. The images to the right show a spread in the histogram as image mis-alignment increase from left to right and the corresponding joint entropies.

Principal Component Analysis of Multivariate Images

Principal component analysis (PCA) is a multivariate technique that finds the directions in n-dimensional space that best describes the data in the least squares sense. That vector gives the direction of the first principal component. A second vector orthogonal to the first principal component is then determined. This vector accounts for the variation of the data that is not described by the first. The principal components are ordered such that the first principal component explains the greatest amount of variation in the data set, the second principal component explains the next greatest variance, and so on.⁶⁷ The maximum number of principal components that can be calculated is the smaller of the number of samples or variables. Generally, the first few principal components will contain most of the systematic variation in the data, so if there are n principal components, the remaining $n-p$ components account for the noise within the data set. Therefore, the principal components that account for the largest variation, p , can be used to recreate the original data within experimental error. The number of meaningful components needed to explain most of the variance in the data can be determined by various procedures. A method proposed my Cattell in 1966 to determine the number of significant components is the scree plot, which is a plot of the eigenvalues or percent variance captured versus the principal component.⁶⁸ From the scree plot shown in Figure 4, the plot gives a horizontal line over the range of components that describes only noise, and there is a positive deviation when the data describes systematic variation in the data in addition to error.⁶⁷ Cattell suggests looking for a point in the plot where the percent

variance captured is greater than the noise level; he referred to it as a “knee” in the plot. Components to the right of the knee are not retained for the model. In Figure 20, three or four components would be retained for the model. In this sense, principal component analysis can be used to compress highly correlated data and remove unstructured noise from the data.

A multivariate image can be considered to be a stack of congruent, gray level images, where each image is a variable (e.g. wavelength, energy, frequency, time etc.) and can be represented as a 3D array. In multivariate image analysis, PCA decomposes a multivariate image into a ‘variable’ part and an ‘object’ part. The ‘variable’ portion is called the loadings.⁶⁹ Loadings describe the relationship between the variables, which contribute the most or the least to each principal component. The ‘object’ part is called a score image. The score image describes the relationships between pixels, which contribute the most or least for each principal component.⁵⁶ Figure 21 illustrates the decomposition of a multivariate data set into score images and loadings.

Multivariate image analysis by PCA begins by first unfolding the 3D ($n_x * n_y * n_z$) array, that was described in the previous paragraph, into a 2D ($(n_x * n_y) * n_z$) matrix X, as shown in Figure 22, and then performing PCA:

$$\mathbf{X} = \sum_{a=1}^A \mathbf{t}_a \mathbf{p}_a^T + \mathbf{E} = \mathbf{T} \mathbf{P}^T + \mathbf{E} \quad (15)$$

where **T** is the score matrix composed of orthogonal columns \mathbf{t}_a known as score vectors, T is the matrix transpose, **P** is the loading matrix composed of orthonormal columns \mathbf{p}_a

called loading vectors and E is the residual, noise. In the summation A is less than or equal to the rank.⁷⁰

Since the resulting long and thin unfolded array is large, a kernel matrix ($\mathbf{X}^T \mathbf{X}$) is calculated and single value decomposition is performed on this matrix to obtain the loading vectors \mathbf{p}_a ($a = 1, \dots, A$). The score vectors are calculated from:

$$\mathbf{t}_a = \mathbf{X}\mathbf{p}_a \quad (16)$$

The score vectors \mathbf{t}_a ($a = 1, \dots, A$) are then folded back into score matrices \mathbf{T}_a ($a = 1, \dots, A$) which will appear as images. \mathbf{T}_1 is the image with the largest variance followed by \mathbf{T}_2 , and so on.⁷⁰

PCA can be used to highlight specific features in the image, for example. A principal component variable, \mathbf{t}_a , for each dimension ($a = 1, \dots, A$). This principal component variable is a linear combination of the pixel intensities from each variable image. The linear combination is determined by the corresponding loading vectors \mathbf{p}_a . Therefore, each principal component captures a different feature in the image and the score matrix \mathbf{T}_a represents the image in terms of the feature.⁷⁰ Multivariate image analysis is applied to a set of multivariate valence band XPS images, core level XPS images and confocal images in Chapter 4.

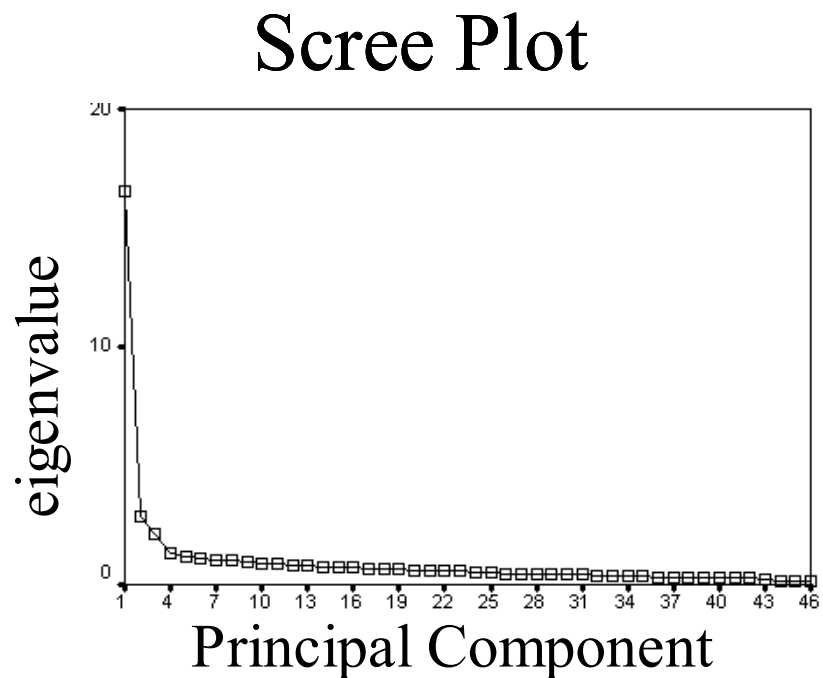


Figure 20. A scree plot obtained from PCA. The horizontal line in the plot represents noise in the data. A positive deviation from the horizontal line is where the principal components begin to explain the systematic variation in the data, the “knee”. In this plot, the first 3 or 4 components would be retained for the model.

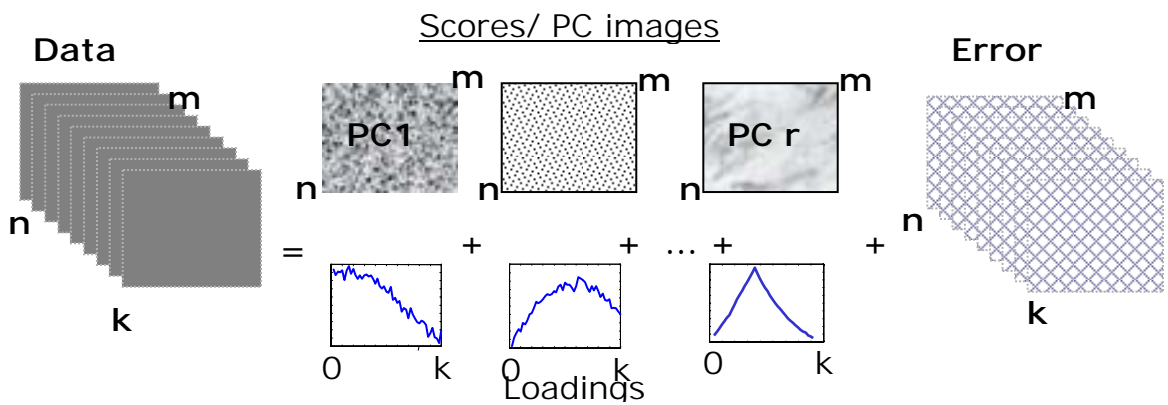


Figure 21. A multivariate data set that is decomposed into an ‘object part’ (scores), a ‘variable’ part (loadings), and an error matrix, E . p principal components account for much of the variation in the data, while $n-p$ components represent noise in the data, E

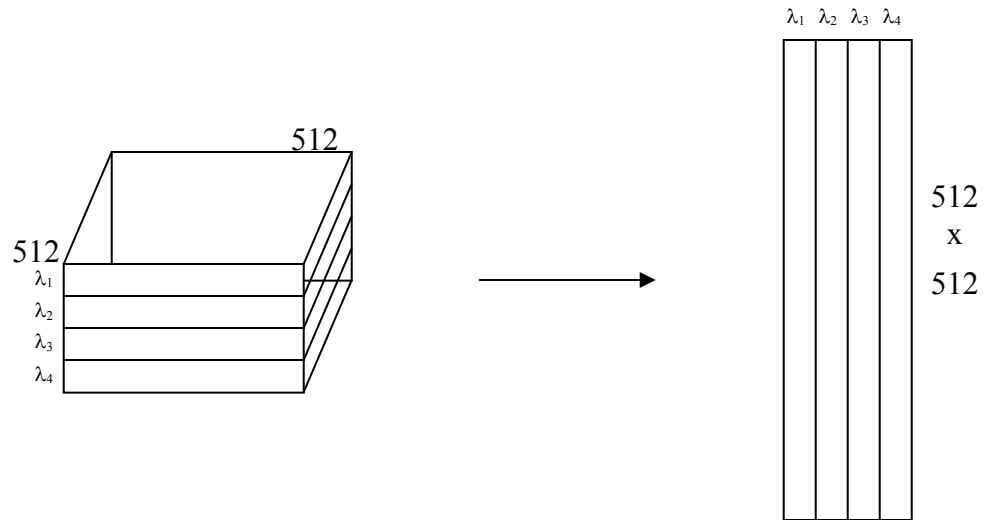


Figure 22. (a) A stack of 512×512 images at 4 different wavelengths λ_i , making a 3-way array. The matrix is unfolded into a 2-way matrix. The column dimension is now equal to 262,144 ($512 \cdot 512$), forming image data that have thin and long unfolded matrices.

CHAPTER 4

CORRELATION OF AFM AND XPS IMAGING FOR QUALITATIVE AND QUANTITATIVE PHASE IDENTIFICATION IN POLYMER BLENDS

Introduction

For multi-component materials, understanding both bulk and surface composition is important. It can, however, be difficult to uniquely distinguish between alternative surface morphologies that are formed in heterogeneous samples or to obtain sufficient information to completely understand the surface chemical structure of an organic material using a single surface analysis method. A multitechnique correlative approach will yield information that can be integrated to provide a more complete picture of complex organic systems. Improvements in the spatial resolution and data acquisition times for a variety of analytical instrumentation allow for new approaches to the chemical characterization of complex heterogeneous materials. For example, recently there has been an increase in the number of spectroscopic imaging techniques, including imaging Fourier transform infrared spectroscopy (FTIR) and imaging X-ray photoelectron spectroscopy (XPS). Current instrumentation for these two techniques allows for fast parallel imaging, comparable lateral resolution, and an overlap in the field of view, making direct image comparison possible. Direct correlative studies combining XPS and

FTIR data from the same areas on polymer blend samples allowed for correlation of bulk and surface chemistry.^{3,56} Long acquisition times, dramatic differences in spatial resolution and problems in locating the same areas for multiple techniques made this approach impractical until the current generation of instruments was available.

Although the difference in spatial resolution and analysis area complicates comparisons, XPS and AFM can also be correlated to enhance chemical characterization of polymer blends. XPS provides elemental and chemical information from the top 8-10 nm of a sample. Imaging XPS provides an elemental or chemical distribution map of the surface with a 2-5 μm spatial resolution.⁷¹ Phase-contrast AFM provides information about the sample properties, adhesion, friction and viscoelasticity,^{8,22-24,26} but no direct chemical information can be derived from the images. This makes it difficult to identify the phases responsible for the observed contrast. Combining the elemental and chemical information obtained from XPS with the topographical and phase data obtained from AFM, positive identification and quantification of the different phases becomes possible. This work demonstrates a procedure for image phase identification and correlation on two different sample systems. The first is a patterned surface containing easily identifiable phases that can be used to test and validate methods described herein. The approaches developed are then applied to poly (methyl methacrylate)/poly (vinyl chloride) (PMMA/PVC) blends of varying composition.

A variety of different methods have been used to characterize PMMA/PVC blends, leading to inconsistencies and conflicting conclusions regarding their structure.^{5,17,72} The level of heterogeneity that is detected depends upon the analysis area of the

characterization technique, and the number of areas and/or films, which are analyzed. These blends were previously analyzed using a large analysis area relative to the domain size, leading to the conclusion that the blends were homogenous. Surface analysis of the blends using modern XPS instruments with small sampling areas, and TOF-SIMS imaging of such films, demonstrated heterogeneous surface composition with an enrichment of PMMA at the surface.^{17,37,73} Extensive research by our group on this blend, using spectroscopy and imaging XPS, showed that the PMMA/PVC polymer blend system phase separates with the formation of two phases: one enriched in PVC and the second enriched in PMMA, although both PMMA and PVC are present in each phase.^{3,37} The substrate-facing side is homogeneous and enriched in PVC, while the air-facing side is heterogeneous and enriched in PMMA. The behavior of PMMA/PVC blends is complex, but our understanding of the system through previous work makes the blend a good “real” sample to use, after developing an approach on a patterned surface. One previous study in our group involved direct correlative studies combining XPS and FTIR data from the same areas on polymer blend samples.³ The readily interpretable chemical information obtained from the combination of XPS imaging and small area spectroscopy makes it possible to utilize XPS in the evaluation of phases detected by AFM phase imaging. As will become apparent in this discussion, it is critical to have one technique for which the chemical information can unambiguously be obtained even if there is a large difference in spatial resolution or sampling depth.

Experimenta

l

Films of Shipley S1818 were spun cast onto indium tin oxide and post apply baked at 95 °C. The photoresist was exposed to a mercury UV lamp for five minutes through a patterned mask containing ~6 µm line widths with a pitch of ~6 µm. After exposure, the sample was developed using a Shipley Microposit MF-312 Developer CD-27 for one minute. The sample was rinsed using deionized water, air blow dried and hard baked at 115 °C.

Poly (vinyl chloride) (PVC) of 73.3 kDa and poly (methyl methacrylate) (PMMA) of 75 kDa were used as received from Scientific Polymer Products, Inc. Three blends containing 25 % PMMA : 75% PVC, 50% PMMA : 50% PVC and 75% PMMA : 25% PVC were prepared for AFM and XPS analyses.

Films for XPS analysis were prepared by combining the PMMA and PVC in a 2% w/v solution in HPLC-grade tetrahydrofuran. The solutions were allowed to sit for at least 24 h and deposited on Teflon® watch glasses using pipettes. Films were allowed to air dry for 24-48 h and then peeled from the Teflon substrate for analysis. The 50/50 PMMA/PVC blend utilized for XPS and AFM analysis on the same sample area was prepared as described above, but the sample was left on the Teflon® substrate during the analysis.

Samples for AFM characterization were prepared by mixing PMMA and PVC in a 0.2% w/v solution in HPLC-grade tetrahydorfuran. Solutions were allowed to sit at least 12 hours before being solvent cast on freshly cleaved mica substrates. For these

samples, the solutions were deposited on mica with pipettes and allowed to sit for at least 12 hours before AFM analysis.

AFM images were obtained on a Digital Instruments Multimode NanoScope IIIa scanning probe microscope. Height and phase images were recorded simultaneously under ambient conditions in tapping mode. Commercial Si₃N₄ cantilevers with force constants of 2.5-8.5 N/m, and resonance frequencies between 120-190 kHz were used.

Spectra and images were acquired on a Kratos Axis Ultra photoelectron spectrometer using a monochromatic Al K α source operating at 300 W. The base pressure was 2×10^{-10} torr and the operating pressure was 2×10^{-9} torr. Charge neutralization was used for all samples to prevent charge accumulation. High magnification XPS images of the patterned surface were acquired at a pass energy of 80 eV for 4 minutes. Low and high magnification XPS images of the PMMA/PVC polymer blends were acquired at 80 eV for up to 6 minutes. Image files were transferred into ASCII format for deresolution and image classification in ENVI.⁶⁰

Qualitative Evaluation of AFM Images

Fractal Analysis of PMMA/PVC blends

The fractal dimension, D, for the PMMA/PVC blends was calculated to provide information about the self-similarity and disorder of the surface. As discussed in Chapter 3, if a surface is fractal then the fractal dimension is $2 \leq D \leq 3$. The larger D is, the more disordered the surface. AFM topography images of the PMMA/PVC blends deposited on

mica were analyzed for their fractal dimension using the box counting method in the Digital Instruments software.⁵⁹ 25/75, 50/50 and 75/25 PMMA/PVC blends were analyzed at three different scan sizes: 1 μm , 5 μm and 10 μm . Details about the calculation of the fractal dimension can be found in Chapter 3. The resolution of all measurements was 512 x 512 points with equal steps in the x and y directions. The results of the analysis are shown in Table 2. For the images acquired at a scan size of 1 μm the calculated fractal dimensions were similar for the three blend combinations, 2.50 ± 0.09 , 2.40 ± 0.02 and 2.46 ± 0.12 , for the 25/75, 50/50 and 75/25 PMMA/PVC blends, respectively. The fractal dimension for AFM images at the 5 μm level reaches a maximum of 2.79 for the 75/25 blend of PMMA and PVC. The fractal dimension for the 25/75 and 50/50 blends were similar, 2.66 ± 0.08 and 2.65 ± 0.06 . At a 10 μm scan size the fractal dimension for the 25/75 and 50/50 blends were determined not to be statistically different from each other as calculated from the Student's t-test. However, at the 10 μm scale, the fractal dimension for the 75/25 blend is 2.78 ± 0.04 . Overall, the data shows that there is not much of a difference in the fractal dimension for blends at the 25/75 and 50/50 level. From the fractal dimensions calculated, it appears that the PMMA/PVC blends form a highly disordered (fractal) surface. The fractal dimension was also calculated for three AFM topography images of the patterned polymer sample. The results can be found in Table 5. The fractal dimensions for the 100x100 μm^2 AFM topography images were all similar ($D = 2.57$, 2.57, and 2.58).

Table 2. The calculated fractal dimension for AFM topography images obtained at different scan sizes

Measured Sample	Scanning Area (μm^2)	Number of Samples Analyzed	Average FD \pm SD
25/75 PMMA:PVC	1	6	2.50 \pm 0.09
	5	3	2.66 \pm 0.08
	10	7	2.57 \pm 0.16
50/50 PMMA:PVC	1	4	2.40 \pm 0.02
	5	6	2.65 \pm 0.06
	10	10	2.62 \pm 0.13
75/25 PMMA:PVC	1	7	2.46 \pm 0.12
	5	2	2.79
	10	4	2.78 \pm 0.04

AFM Deresolution for Correlation with XPS Images

To qualitatively compare AFM and XPS images, differences in the imaging field of view and spatial resolution for the two techniques have to be taken into consideration. It is possible for the XPS imaging field of view to overlap with that of AFM. Currently, the field of view for imaging XPS can vary, depending on the instrument, from greater than $1 \times 1 \text{ mm}^2$ down to less than $200 \times 200 \mu\text{m}^2$, while that for AFM is up to $200 \times 200 \mu\text{m}^2$. It can be difficult to obtain AFM images this large on samples with significant topographical heterogeneity. Frequently, therefore, AFM images are smaller than high spatial resolution XPS images. Comparably sized XPS images are obtained by selecting an area from the XPS image and cropping the image to the same dimensions as the AFM image. Figure 23 (a) is a $200 \times 200 \mu\text{m}^2$, O 1s XPS distribution map of a 75% PMMA: 25% PVC polymer blend. The brighter areas are more enriched in oxygen-containing PMMA, while the darker areas are enriched in PVC relative to the bright areas. Black squares in the image outline the cropped area. Figure 23 (b) is the area from Figure 23 (a), cropped to $20 \times 20 \mu\text{m}^2$ to match the field of view of the AFM images. The lateral resolution in the photoelectron images allows for the same features to be distinguished in the small-cropped images as in the original images.

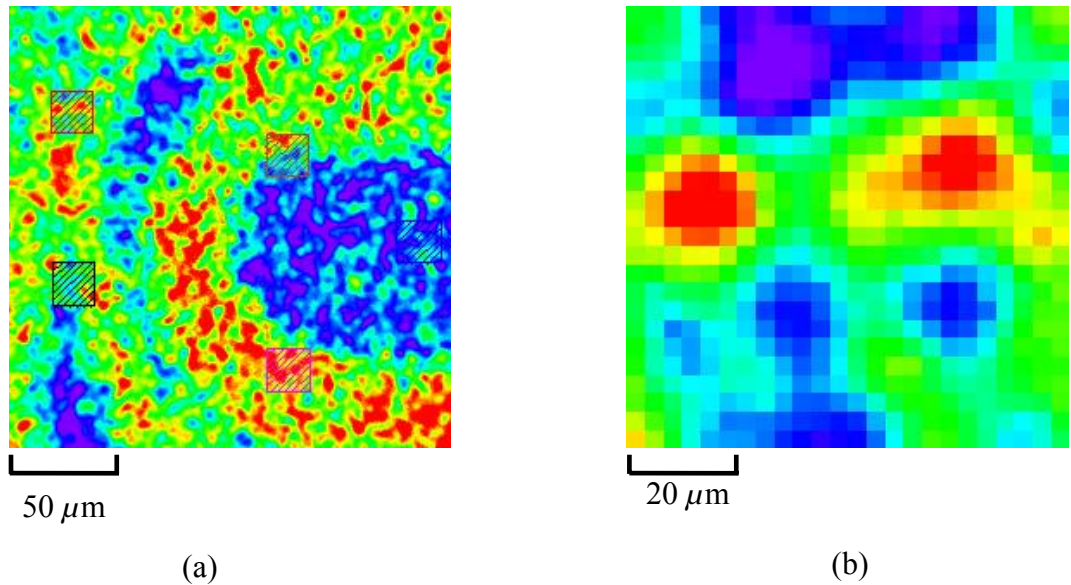


Figure 23. (a) Original 200x200 μm^2 , imaging XPS O_{1s} distribution map of a PMMA/PVC (75/25) polymer blend. The dark black line outlines the area that will be left after cropping the image. (b) The outlined area from Fig. 23(a) after being cropped to 20x20 μm^2 .

Even if the same phase information is present, the difference in spatial resolution complicates comparison of $20 \times 20 \text{ } \mu\text{m}^2$ XPS and AFM images. Imaging XPS has a spatial resolution of $2\text{-}5 \text{ } \mu\text{m}$, while the AFM has nanometer resolution. It is important to develop methods that allow for the determination of whether the two techniques are accessing similar compositional or phase variations. One approach to qualitative correlation of the XPS and AFM images is to match the resolution of images acquired from the two techniques. The higher spatial resolution AFM images can be deresolved by applying a median convolution filter to the images using a specific kernel size. This two-step procedure can be applied to any two images with different properties. First, the mathematical resolution of the two techniques is matched in terms of $\mu\text{m}/\text{pixel}$, followed by a match of the technique spatial resolutions. Technique spatial resolution, in this case, is the number of pixels that should be combined into one resolution unit. The mathematical resolution of the AFM images is matched to the XPS images by calculating the kernel size needed in the median convolution filter. The mathematical resolution for an XPS image and an AFM image is calculated in terms of $\mu\text{m}/\text{pixel}$. For example, a $50 \times 50 \text{ } \mu\text{m}^2$ AFM image composed of 512×512 pixels has a mathematical resolution of $0.1 \text{ } \mu\text{m}/\text{pixel}$ and a $50 \times 50 \text{ } \mu\text{m}^2$ cropped XPS image of 64×64 pixels has a mathematical resolution of $0.78 \text{ } \mu\text{m}/\text{pixel}$. The XPS mathematical resolution is divided by the AFM mathematical resolution and a value of 7.8 is obtained, but the kernel size must be an odd value, so it is rounded up to 9 pixels. Technique spatial resolution is matched by calculating the number of pixels that should be combined into one resolution unit. The obtained value corresponds to the kernel size that should be used in the median

convolution filter. The mathematical resolution of a cropped $50 \times 50 \mu\text{m}^2$ XPS image is $0.78 \mu\text{m}/\text{pixel}$ and the spatial resolution of imaging XPS is $\sim 3 \mu\text{m}$. To obtain the kernel size, the spatial resolution must be divided by the mathematical resolution. In this case a value of 3.8 pixels is calculated, but the kernel size is an odd value and is rounded up to 5 pixels.

Figure 24 (a) is an original $20 \times 20 \mu\text{m}^2$ AFM topography image of a PMMA/PVC (75/25) blend before being deresolved. Figure 24 (b) is the same image after deresolution, and Figure 24 (c) is a cropped $20 \times 20 \mu\text{m}^2$ XPS image of the same composition polymer blend. Similar size and shape features are observed in the deresolved AFM and XPS images. This allows for a qualitative comparison of the XPS and AFM image features, and for the chemical information in the XPS image to facilitate interpretation of phases in the AFM image. Based on this comparison, the light colored phases in 24 (b) appear to be areas enhanced in PMMA.

The patterned sample with $\sim 6 \mu\text{m}$ line widths and a $\sim 6 \mu\text{m}$ pitch was used to confirm the proposed qualitative correlation of AFM and XPS using images of different sizes: 30×30 , 50×50 and $100 \times 100 \mu\text{m}^2$. To match the field of view and resolution, XPS images were cropped to the size of the AFM images, while the AFM topography and phase images were deresolved by the procedure described above. Line widths of the images were measured using the measuring tool in ENVI.⁶⁰ Figure 25 shows resolution matched 30×30 and $100 \times 100 \mu\text{m}^2$ topography and phase AFM images, and an XPS image of the patterned surface. AFM topography and phase line widths were the same after deresolution. The unaltered $100 \times 100 \mu\text{m}^2$ and $30 \times 30 \mu\text{m}^2$ XPS images shown were

obtained by acquiring In 3d images. The intensity in the XPS images is due to the substrate, indium tin oxide (ITO). The dark areas in the images outline the polymer location on the surface, thus the images are the inverse of what is observed in the AFM image. The measured line widths for the $100 \times 100 \mu\text{m}^2$ XPS and AFM images are comparable. The line widths measured for the $30 \times 30 \mu\text{m}^2$ AFM and XPS images are similar. However, the line widths for the $30 \times 30 \mu\text{m}^2$ and $100 \times 100 \mu\text{m}^2$ images differ. One possible explanation for this is the noise in AFM topography and phase images, as well as in the XPS image. This causes variations in the measured line widths. This demonstrates that the proposed deresolution algorithms preserve edge information and feature shape as discussed in Chapter 3.

Quantitative Comparison of AFM and XPS Images

The image deresolution demonstrated in Figures 24 and 25 provides only a qualitative comparison of the XPS and AFM images. If the qualitative comparison indicates that comparable phases are being measured by both techniques, then a quantitative comparison of the phase distribution in each image type can be obtained using unsupervised image classification. Classification is the process of assigning data to one of a fixed number of possible classes.⁵⁴ The goal is to convert the numerical image data into descriptive labels that categorize different phases of the sample. Unsupervised

classification uses statistical techniques to group n-dimensional data into their natural spectral classes. This method is based on grouping or clustering of the data, and the same color is assigned to areas of the image containing similar physical or chemical characteristics. A color-coded phase map is generated showing the spatial distribution of a particular phase, followed by post classification statistics to calculate the percent coverage for the different phases observed. A K-means unsupervised classification algorithm in ENVI⁶⁰ was used to quantify the AFM and XPS images. Figures 26 (a) and (b) are examples of original and classified Cl 2p photoelectron images from a PMMA/PVC (25/75) polymer blend. The red, yellow and green pixels in the image represent areas of higher Cl 2p intensity, or PVC-enriched regions. The blue and purple pixels are PMMA-enriched regions. After applying K-means unsupervised classification to Figure 26 (a), the image contains two classes or phases. The green pixels correspond to PVC-enriched regions and the red pixels correspond to PMMA-enriched regions, previously identified in the original Cl 2p photoelectron image. The percent area surface coverage for the green and red pixels is calculated using post-classification statistics.

Unsupervised classification was initially applied to four AFM and twenty-four XPS images of three different sizes (100x100, 50x50, 30x30 μm^2) from patterned samples, and post-classification statistics were used to calculate the percentage of the image containing ITO. Table 3 shows the results of classification. Although the AFM and XPS images were not acquired from the same area on the sample, they are statistically similar, and reasonable results are obtained even from 30x30 μm^2 XPS images. The

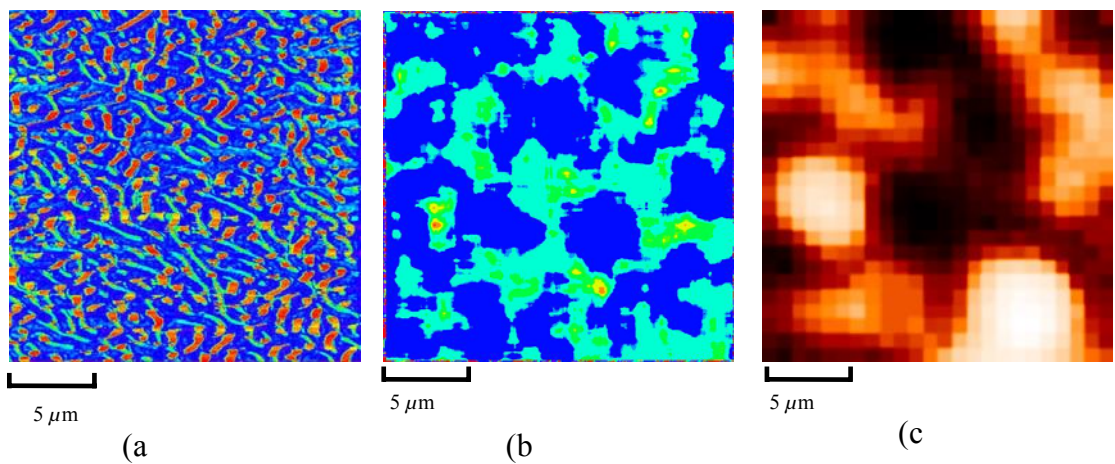


Figure 24. (a) Original $20 \times 20 \mu\text{m}^2$, AFM topography image of a PMMA/PVC (75/25) polymer blend. (b) The image in Fig. 24 (a) after being deresolved. (c) A cropped $20 \times 20 \mu\text{m}^2$ O 1s photoelectron image of the same composition blend shown in Fig 24 (a). Similar size and shape features are observed between the deresolved AFM topography and the cropped O 1s photoelectron image.

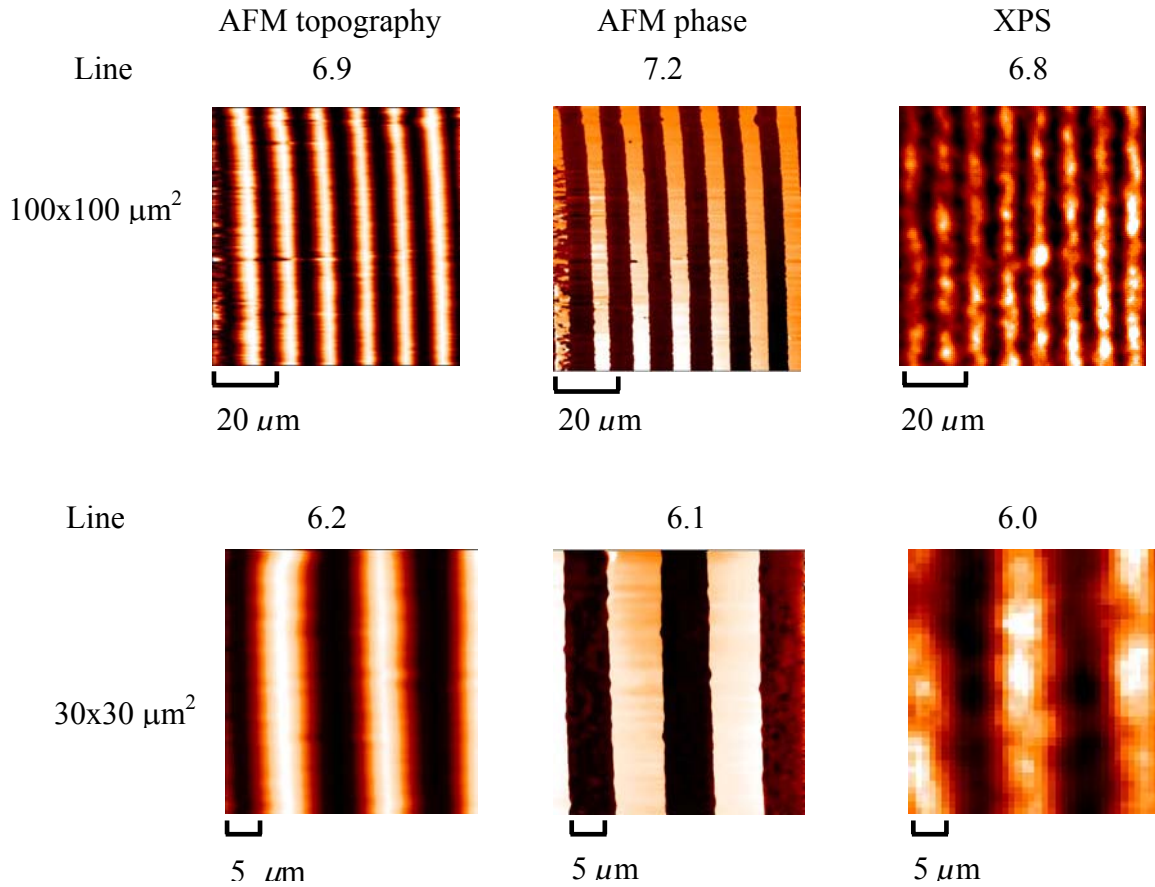


Figure 25. AFM topography and phase line widths, measured with ENVI are shown after deresolution, along with In 3d photoelectron images. The line widths measured for the 100x100 μm^2 XPS and AFM images are similar, and the measured line widths for the two techniques are comparable for the 30x30 μm^2 images. However, the measured line widths differ between the 30x30 μm^2 and 100x100 μm^2 images.

classification results based on this test sample were expected to be in good agreement, and primarily demonstrate the feasibility of the method. The use on a more complex sample is demonstrated on a series of PMMA/PVC blends.

AFM images of the solvent cast polymer films prepared from 0.2% w/v solutions are shown in Figure 27. The 25% PMMA : 75% PVC films in Figures 27 (a) and (b) show well-defined islands in a matrix in both the height and phase images. When the composition is changed to 50% PMMA : 50% PVC, as shown in Figure 27 (c) and (d), the island surface coverage increases. Figures 27 (e) and (f) show that at 75% PMMA : 25% PVC, the islands coalesce to form a larger, more continuous film on the surface. Since the island surface coverage increases with bulk PMMA composition, the islands are probably a PMMA-enriched phase, although this is difficult to determine based on AFM data alone.

High and low spatial resolution XPS images from the three films are shown in Figure 28. The O 1s images approximately represent the PMMA distribution on the surface, while the Cl 2p images represent the PVC distribution. In general, there tends to be PMMA in the PVC-enriched regions, so the images are not necessarily inverses. The O1s images show increasingly large areas enriched in PMMA as the %PMMA in the blend increases, and distinct domains are noticeable with changes in PMMA composition. Although the AFM and XPS phases are of different scales, both techniques show phase changes as a function of composition.

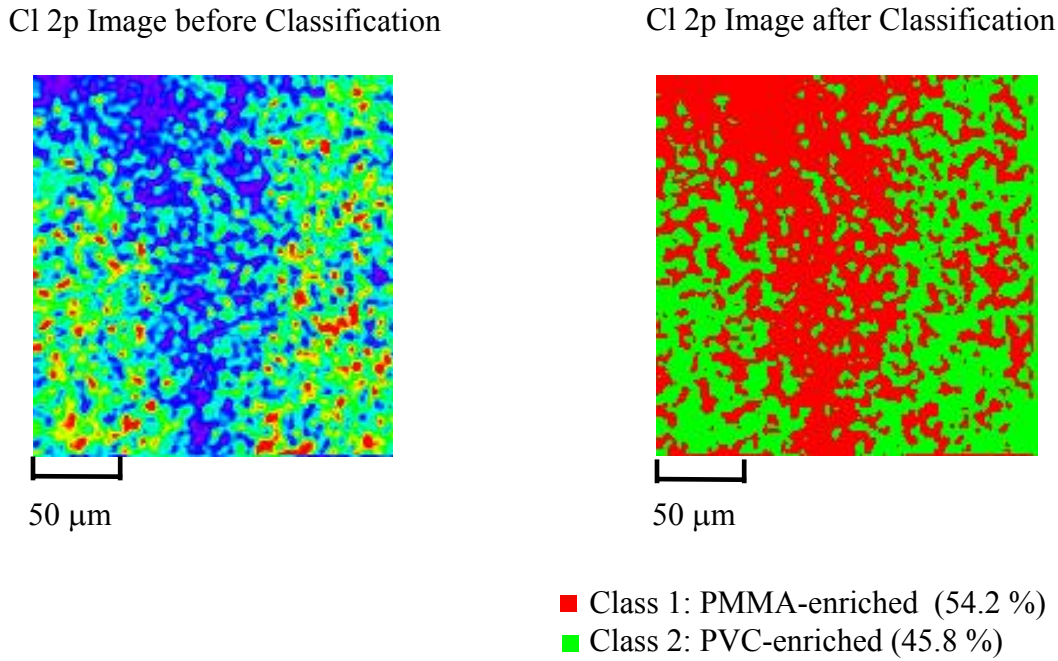


Figure 26. (a) Original 200x200 μm^2 , Cl 2p photoelectron image of a PMMA/PVC (25/75) polymer blend. The red yellow and green pixels in the image represent areas of Cl 2p intensity or PVC-enrichment, while darker blue and purple areas are enriched in PMMA. (b) The Cl 2p photoelectron image after K-means unsupervised image classification and post-classification statistics have been applied to the original Cl 2p photoelectron image. The image now displays two classes represented by red and green pixels. A green pixel in the image corresponds to the PVC-enriched regions identified in the original XPS image, and red pixels correspond to PMMA-enriched regions. Post-classification statistics calculated the percent area surface coverage for the red and green pixels, thus the surface coverage of PMMA-enriched regions and PVC-enriched regions in the image.

Table 3. % ITO detected by imaging XPS and AFM, calculated from K-means unsupervised classification post-classification statistics

	AFM Topography Image % ITO	AFM Phase Image % ITO	XPS Image % ITO
30x30 μm^2	50.3 \pm 0.8	50.5 \pm 9.3	48.7 \pm 1.3
50x50 μm^2	50.2 \pm 0.8	49.6 \pm 5.5	48.8 \pm 0.4
100x100 μm^2	50.1 \pm 1.1	44.1 \pm 2.6	48.3 \pm 0.9

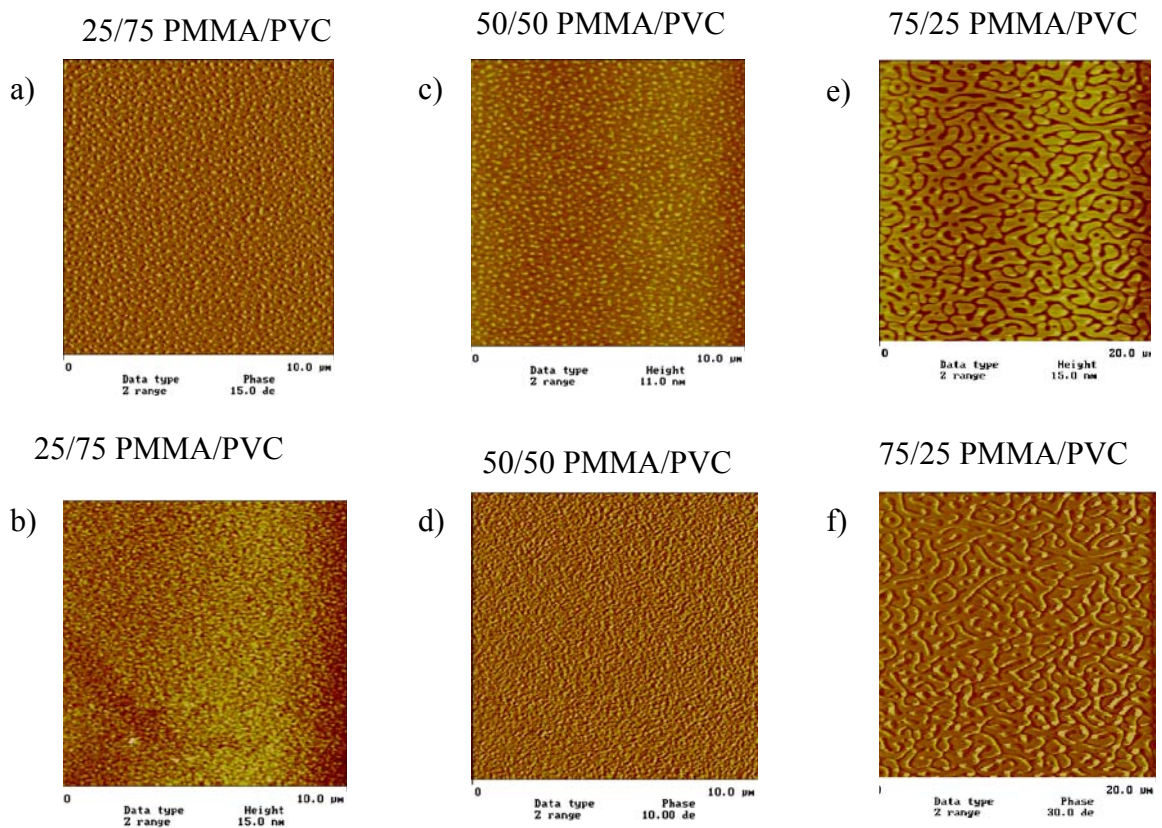


Figure 27. AFM surface topography (a,c,e) and phase image (b,d,f) of PMMA/PVC blends of various compositions (25/75, 50/50, 75/25).

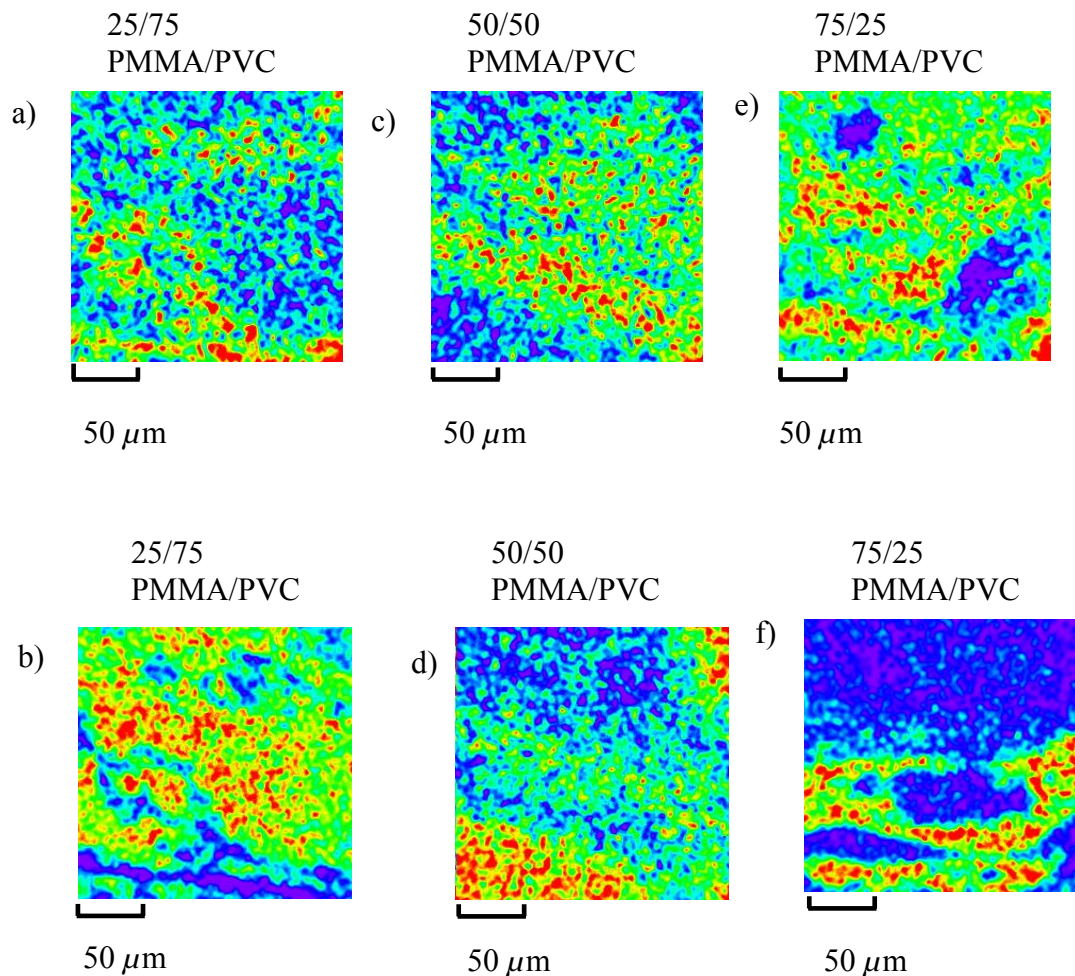


Figure 28. O1s (a, c, e) and Cl 2p (b, d, f) photoelectron images of PMMA/PVC film blends of various composition (25/75, 50/50, 75/25) solvent cast on Teflon® and removed for analysis. Films were prepared from a 2% w/v solution.

AFM images were deresolved for qualitative comparison with the XPS images. An example of image deresolution was shown in Figure 24 (b) for a PMMA/PVC blend (75/25). The deresolved AFM image contains features similar in size and appearance to the cropped XPS image shown in Figure 24 (c). K-means unsupervised classification was applied to the original AFM and XPS images to calculate the percent surface coverage for the PMMA and PVC-enriched regions in the XPS images, and to assist in chemical identification of the phases observed in the AFM images. Using the classification data obtained from the XPS and AFM images, the PMMA-enriched surface coverage for the blends (25/75, 50/50, 75/25) was calculated. Classification was applied to both O 1s and Cl 2p XPS images. PMMA-enriched regions were identified in the classified XPS images by comparison with the original XPS images. PMMA-enriched regions in the classified AFM phase images were also identified by comparison with the XPS classification results. Results of for the PMMA-enriched surface coverage for the PMMA/PVC blends detected by AFM and the PMMA-enriched surface coverage detected by XPS can be found in Table 4. A plot of the PMMA-enriched surface coverage for the PMMA/PVC blends detected by AFM versus the PMMA-enriched surface coverage detected by XPS demonstrates that the two techniques correlate reasonably well, as shown in Figure 29. This allows for a quantitative comparison of AFM and XPS images and can serve as a new method for identifying AFM phases observed. For the 25/75 and 50/50 blend compositions, surface segregation of PMMA

Table 4. A comparison of the %PMMA detected by AFM and XPS for PMMA/PVC blends (The number of samples analyzed is in parenthesis)

Measured Sample	%PMMA detected by XPS	%PMMA detected by AFM
25/75 PMMA:PVC	41.9 \pm 6.2 (4)	46.1 \pm 7.6 (4)
50/50 PMMA:PVC	52.3 \pm 2.4 (4)	62.3 \pm 9.1 (4)
75/25 PMMA:PVC	59.7 \pm 2.5 (4)	63.9 \pm 3.2 (5)

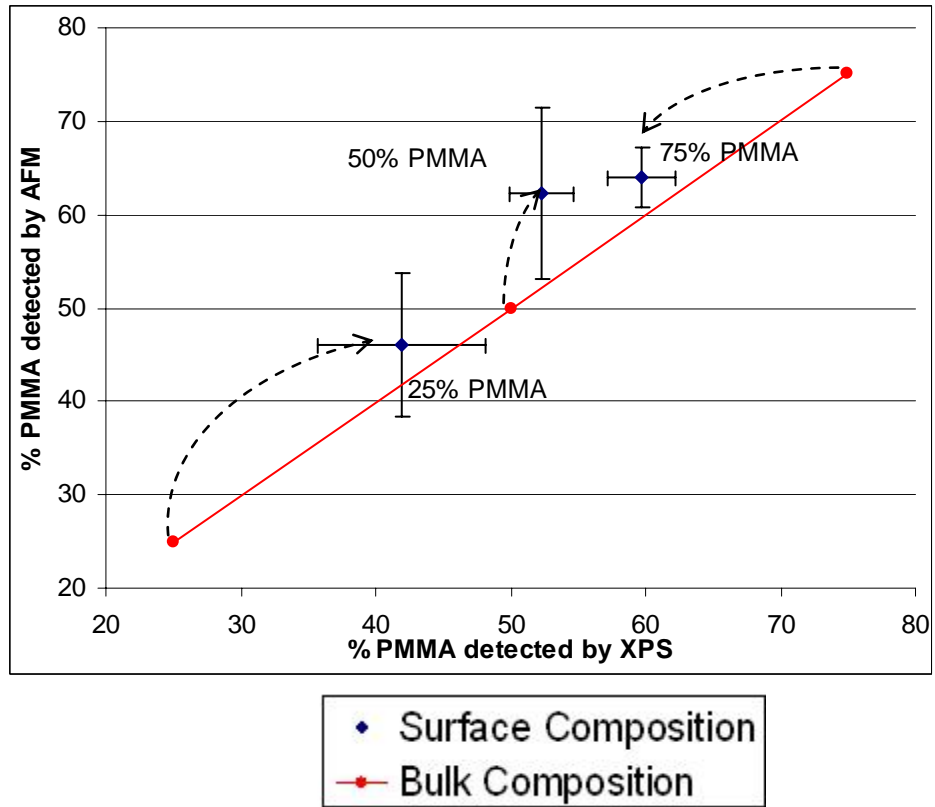


Figure 29. % PMMA detected by AFM versus the % PMMA detected by XPS. Both techniques show enhanced PMMA surface composition relative to the bulk composition for the blends containing 25% and 50% PMMA. The 75% blend contains less PMMA than the bulk composition, based on both XPS and AFM results.

relative to the bulk is confirmed by both methods. For the 75/25 blend, PVC segregation, relative to the bulk composition, is observed by both experiments, providing an interesting observation of a possible phase inversion.

Previous studies on PMMA/PVC blends by XPS and time-of-flight secondary ion mass spectrometry show that there is an enrichment of PMMA at the surface.^{5,17} One driving force for the enrichment of PMMA at the surface is the slightly lower surface tension of PMMA relative to PVC, and the degree of enrichment is dependent upon the molecular weight of PMMA.^{16,74} A slight excess of PMMA is observed for two blend combinations (25/75, 50/50), but for the 75/25 blend a phase inversion is observed. The % PMMA at the surface is less than the bulk composition, although the surface contains more PMMA than PVC. This is consistent with results obtained from Short et al.⁷² While most of the literature shows an excess of PMMA on the surface, relative to the bulk composition, Short et al. obtained results showing a phase inversion at the surface for 70/30 blends using TOF-SIMS imaging. At greater PMMA concentrations, PMMA formed the matrix.⁷²

The Effect of Kernel Size on Classification Results

The comparison above utilized the original AFM data. It is useful to evaluate the extent to which different kernel sizes affect classification results from the deresolved AFM topography and phase images were evaluated. This was done by comparing results from the original data with data obtained using different kernel sizes in the deresolution process. Kernel sizes of 9, 11 and 13 were used in the median convolution filter in the

first step of the two-step deresolution process. In the second step, a kernel size of 5 was used in the median convolution filter for all the deresolved images. All of the images were processed in ENVI,⁶⁰ as described in the deresolution and classification sections. Results are shown in Tables 5 and 6. The AFM topography and phase images of the patterned sample and various blends of PMMA/PVC were analyzed. For a series of AFM topography images of the patterned polymer sample, the largest percent difference observed between the original data and the deresolved data was 0.3%. In the case of the phase images of the patterned polymer sample, the largest percent difference observed was 1.2%. The deresolved data matches the original data closely in the case of all the data obtained from the patterned sample. The deresolution process causes the patterns to be altered proportionately, thus conserving the results obtained for different kernel sizes used.

AFM topography and phase images of various blends of PMMA/PVC were also evaluated using different kernel sizes as described above. The largest percent difference observed between the original data and the deresolved data was 37.3%. For the phase images of the PMMA/PVC blend the largest percent difference observed was 30.5%. The data for the blends shows a considerably larger percent difference between the original images and the deresolved images. The classification results are compared for the XPS with resolution matched AFM topography images ($K = 9$). The %PMMA detected by XPS and the resolution matched AFM images ($K = 9$) are within 23.4% of each other for three of the four results. The largest % difference observed for the %PMMA detected by XPS and AFM for the four results is 66.6%. For the % PMMA detected by XPS and the

resolution matched AFM phase images ($K= 9$), the results are all within 26.7% of each other. One possible reason for the large differences observed in the comparisons is the results are dependent upon the features observed in the image. For example, if the original image shows small, closely spaced polymer domains embedded in a polymer matrix, the image after deresolution will show domains that have coalesced, forming continuous features. This will result in a difference between the calculated domain and matrix surface coverage between the original and deresolved images. Additionally, the AFM images of the PMMA/PVC blends are highly fractal

Exact Area Matching

The methods presented so far provide possible approaches to correlation of XPS and AFM data. Although it is more difficult, the comparison is more convincing if the data is acquired from the same areas on the samples. Multi-technique image alignment requires acquisition of images, and possibly small area spectra, from the same area on the sample. The problem has been approached through a variety of methods. The simplest approach is to mark sample areas with a felt pen, but this becomes difficult when the analysis area approaches the dimensions of the pen tip. Optical features on the sample can provide an area marker, but may not always be present. Grids have also been used to locate areas, but the height differential between the grid and the sample is frequently greater than the vertical range of the AFM scanner, preventing imaging of the grid.

Table 5. The effect of kernel size on classification results for AFM topography and phase images of a patterned polymer sample.

Composition	Original AFM Topography Image	Fractal Dimension	K = 9 (% difference)	K = 11 (% difference)	K = 13 (% difference)
% ITO	51.9	2.57	51.9 (0.1)	51.9 (0)	51.9 (0.1)
% Polymer	48.1		48.1 (0.1)	48.1 (0.1)	48.1 (0.1)
% ITO	49.8	2.57	50.0 (0.6)	50.1 (0.7)	49.9 (0.3)
% Polymer	50.2		50.0 (0.6)	49.9 (0.7)	50.1 (0.3)
% ITO	52.9	2.58	52.9 (0.1)	52.9 (0.1)	52.9 (0.1)
% Polymer	47.1		47.1 (0.1)	47.1 (0.1)	47.1 (0.1)

Composition	Original AFM Phase Image	K = 9 (% difference)	K = 11 (% difference)	K = 13 (% difference)
% ITO	45.3	45.3 (0.2)	45.3 (0.1)	45.3 (0)
% Polymer	54.7	54.7 (0.1)	54.7 (0.1)	54.7 (0)
% ITO	47.0	46.8 (0.4)	46.7 (0.6)	46.7 (0.6)
% Polymer	53.0	53.2 (0.4)	53.3 (0.6)	53.3 (0.6)
% ITO	48.7	48.1 (1.2)	48.2 (1.1)	48.3 (0.7)
% Polymer	51.3	51.9 (1.1)	51.8 (1.0)	51.7 (0.1)

Table 6. The effect of kernel size on classification results for AFM topography and phase images of PMMA/PVC blends.

Composition	Bulk Composition	XPS image	Original AFM Topography image	K = 9 (% difference)	K = 11 (% difference)	K = 13 (% difference)
% PVC	75	58.1	63.8	67.9 (6.4)	70.5 (10.4)	70.5 (10.4)
% PMMA	25	41.9	36.2	32.1 (11.3)	29.5 (18.4)	29.5 (18.3)
% PVC	50	47.7	41.8	39.8 (4.7)	40.1 (4.0)	39.5 (5.4)
% PMMA	50	52.3	58.3	60.2 (3.4)	59.9 (2.9)	60.5 (3.9)
% PVC	50	47.7	69.4	79.5 (14.4)	80.3 (15.5)	80.8 (16.4)
% PMMA	50	52.3	30.5	20.5 (32.7)	19.8 (35.3)	19.2 (37.3)
% PVC	25	40.3	37.9	36.9 (2.7)	33.3 (12.3)	31.6 (10.2)
% PMMA	75	59.7	62.1	63.1 (1.7)	66.7 (7.5)	68.4 (8.4)

Composition	Bulk Composition	XPS image	Original AFM Phase image	K = 9 (% difference)	K = 11 (% difference)	K = 13 (% difference)
% PVC	25	40.3	29.4	25.2 (14.3)	23.1 (21.5)	20.8 (29.1)
% PMMA	75	59.7	70.6	74.8 (6.0)	76.9 (8.9)	79.2 (12.1)
% PVC	25	40.3	23.1	19.6 (15.4)	17.9 (22.8)	16.1 (30.5)
% PMMA	75	59.7	76.9	80.4 (4.6)	82.1 (6.8)	83.9 (9.2)
% PVC	50	47.7	61.2	61.0 (0.4)	56.9 (7.1)	50.6 (17.3)
% PMMA	50	52.3	38.7	39.0 (0.6)	43.1 (5.1)	49.4 (27.4)

AFM Lithography

An alternative method for marking an analysis area is AFM lithography, which allows for the dimensions of the analysis area to be drawn using contact mode AFM. The tip is scanned under load forces that are experimentally determined to remove sample from the surface. AFM/XPS image alignment was carried out on the ITO patterned surface. The analysis area was drawn in the shape of a $\sim 130 \times 130 \mu\text{m}^2$ box, shown in an optical image in Figure 30 (a). Once drawn, 100×100 , 50×50 , and $30 \times 30 \mu\text{m}^2$ AFM images were obtained from inside the box. $100 \times 100 \mu\text{m}^2$ topography and phase images taken from inside of the analysis area are shown in Figure 30 (b). The box is located using imaging XPS, and data is obtained from the same area on the sample. To aid in locating the box using imaging XPS and AFM, a locator grid is placed over the sample before AFM lithography. This confines the area in which the box is drawn to the dimensions of a single grid square, $420 \times 420 \mu\text{m}^2$ in this case. The In 3d photoelectrons were chosen for imaging the patterned surface. A high magnification $200 \times 200 \mu\text{m}^2$ In 3d photoelectron image is shown in Figure 30 (c). An outline of the analysis area that was drawn using the AFM can be seen in the In 3d photoelectron image. Figure 30 (d) shows an overlay of the $100 \times 100 \mu\text{m}^2$ AFM topography profile and a $100 \times 100 \mu\text{m}^2$ In 3d photoelectron intensity profile. The region outside the marked area was cropped from the XPS In 3d intensity profile image. The AFM topography image and the XPS In 3d photoelectron intensity profile image were aligned by manual rotation so that corresponding features overlapped. The valleys in the AFM image, representative of the ITO substrate, correspond to the hills observed in the XPS In 3d intensity profile, also

due to the ITO substrate. This not only allows for phase identification, but also makes it possible for 3-D characterization by combining the topographical data from AFM and the chemical information from XPS.

Although the data acquisition by XPS and AFM seems straightforward, there were several problems that complicated this approach. For example, analysis by XPS has to be done almost immediately after preparation of the patterned sample was completed. This was done to prevent the accumulation of adventitious carbon on the sample surface, which, as was learned from multiple analyses, interfered with imaging the ITO substrate. On some occasions the patterned sample had to be prepared again due to the absence of a pattern or inconsistent patterns from sample-to sample. In addition, there were instances where the area marked by AFM was visible optically, but not by imaging XPS.

We have successfully analyzed the same area on a 50/50 PMMA/PVC blend using AFM and XPS. A locator grid was placed on a 50% PMMA : 50% PVC blend that was deposited on Teflon®. A high magnification Cl 2p photoelectron image was acquired from inside one of the grid squares. A 120x120 μm^2 AFM topography image was acquired from within the same grid square. The registered images are shown in Figure 31 (a) and (b). (The image registration method is discussed in Chapter 5.) Similar features are observed in the two images. Three circular domains, and a domain oriented diagonally across the surface appear as depressed regions in the Cl 2p photoelectron intensity map in Figure 31 (b). These same domains appear as topographic features in the AFM topography image in Figure 31 (a). This correlation confirms the presence of a PMMA

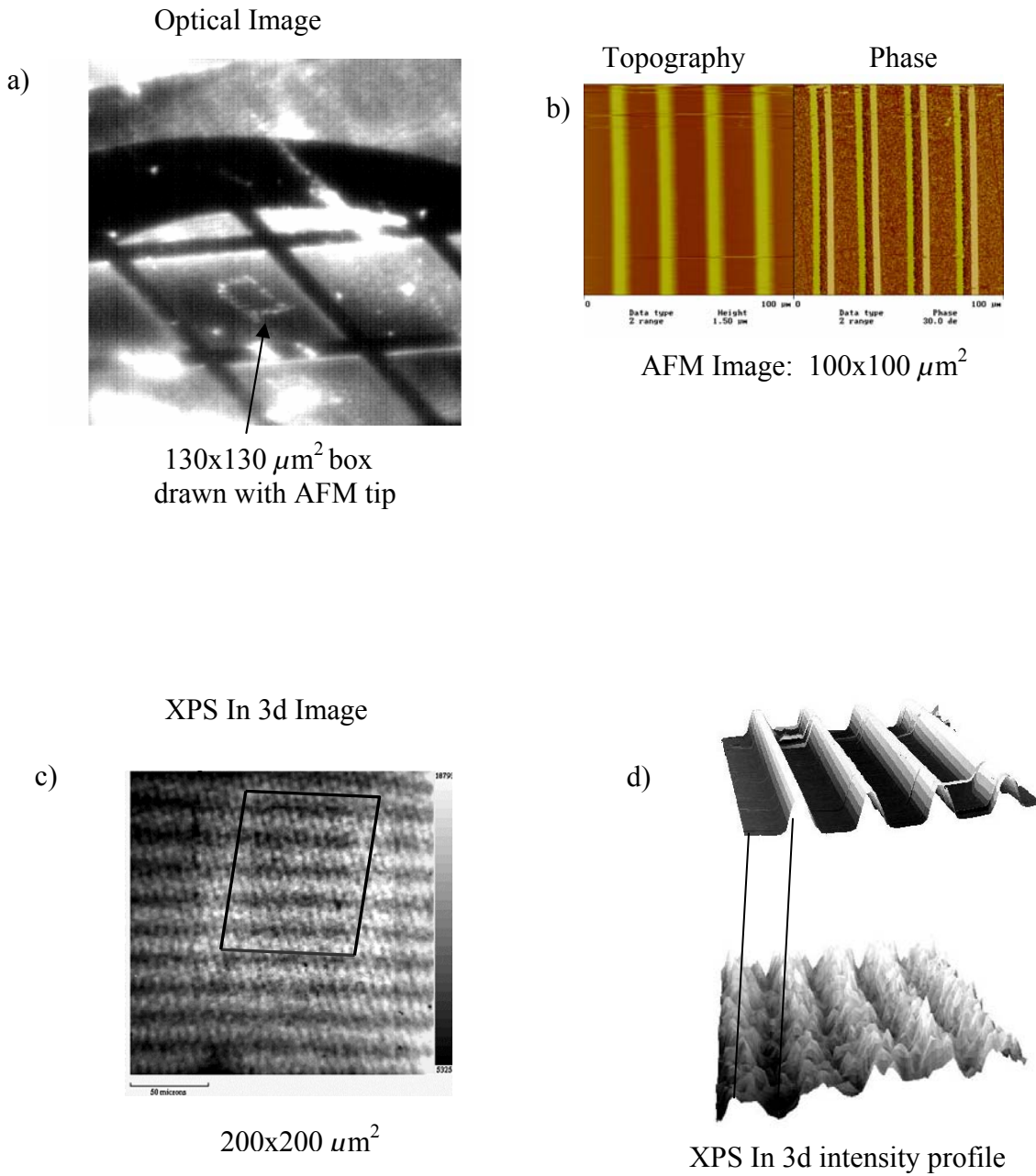


Figure 30. (a) Optical image of the box drawn by contact mode AFM. (b) AFM topography and phase images obtained inside the drawn box. (c) XPS In 3d image of the box. The black lines outline the boundaries of the box. (d) AFM topographical profile and XPS intensity profile. The images are aligned, showing data from the same area on the sample obtained using the two different techniques.

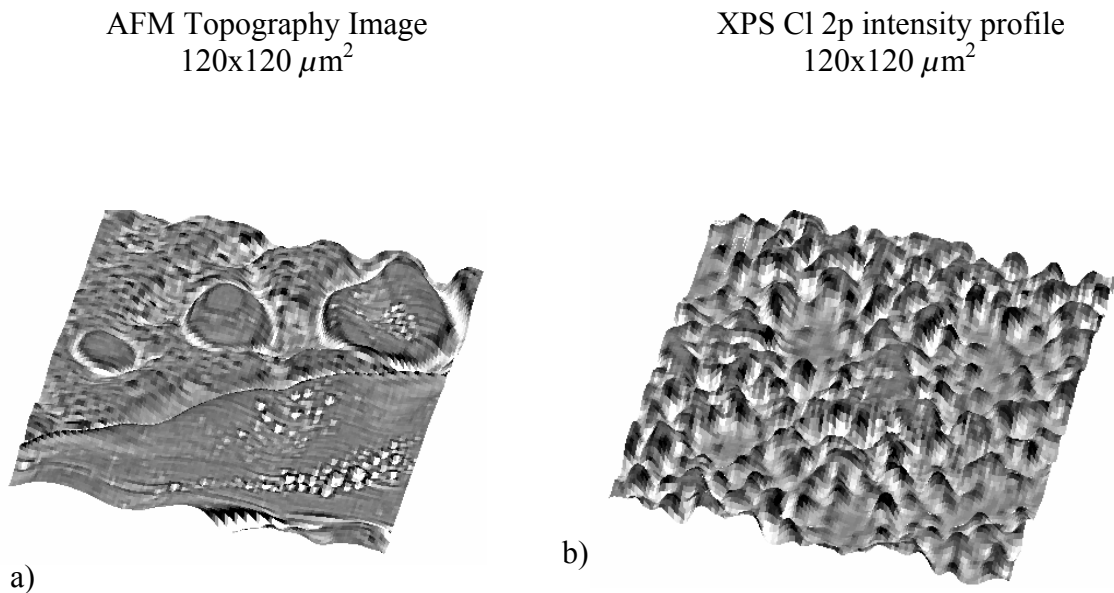


Figure 31. (a) AFM topography profile image from the same area as the cropped XPS Cl 2p image. (b) Cropped XPS Cl 2p intensity profile image from a 50% PMMA : 50% PVC blend.

overlayer, as the topographic features are similar to the PMMA-enriched areas in the Cl 2p map.

Conclusions

A procedure for chemical identification of the phases observed in AFM topography and phase images through correlation with imaging XPS has been demonstrated. Deresolving AFM images and cropping XPS images to the dimensions of the AFM images allows for a rapid qualitative assessment of the phase information contained in both techniques. Unsupervised classification, followed by post-classification statistics, produces a phase map of the images and calculates the surface coverage of each phase. A reasonable correlation between Phases detected by AFM and imaging XPS is observed. For the PMMA/PVC samples, the chemical phases identified through imaging XPS correspond to chemically specific phases in the AFM images. This correlation method can be extended to other heterogeneous samples such as liquid crystal polymer mixtures, biomaterials and organic light emitting diodes.

A method for acquiring data from the same sample area using AFM and XPS has been developed, whereby AFM lithography is used to outline the analysis area on a patterned sample. Applied load forces to the AFM tip are used to outline the analysis area by removing sample from the surface, revealing the substrate. This makes it less challenging to locate the analysis area by visual inspection for AFM analysis. Chemically, the outlined surface is visible using imaging XPS. These methods for the

direct correlation of images acquired using XPS and AFM allow for the identification of chemical phases in topographic or phase AFM images.

CHAPTER 5

Image Fusion of Polymer Blends using AFM, Confocal Microscopy and Imaging XPS

Introduction

Generating a 3-D model of a heterogeneous organic polymer sample using XPS, AFM, and confocal microscopy requires fusion of the images from the three different techniques. The goal of image fusion is to combine image data to form a new image that contains more interpretable information than could be gained using the original data. As discussed in Chapter 2, the benefits of image fusion using these three techniques are the extended spatial coverage due to the varying sampling depths of the techniques; the enhanced spatial resolution since the different methods provide information over a range of spatial dimensions; the enhanced information obtained due to different sampling properties of the techniques; and a resulting reduced ambiguity in the materials characterization.

In the past, image fusion has been implemented widely by the remote sensing and medical imaging communities.⁷⁵⁻⁸⁰ More recently, image fusion has been used by the SIMS community to generate 2-D and 3-D images of surfaces and volumes; however, as with the remote sensing and medical applications, the images were obtained using only a

single technique. Additionally, with SIMS, the sputtering used to generate the 3-D model was destructive to the sample.^{49,81}

Apart from resolution matching and developing a method to obtain data from the same area on a sample using different techniques, as discussed in the previous chapter, image registration must be considered. Image registration is used to establish a spatial correspondence between two images; it is the geometric alignment of corresponding pixels from two different images. There have been several methods devised to address the problem of image registration. In the past, fiducials or reference marks have been added to the sample, but this adds yet another sample preparation step and requires the sample and fiducials to be in the same field of view.⁸² Gilmore et al. used a combination of scratched cross-datum and visible optical interference patterns to register SIMS and AFM images.¹ Plaschke et al. used the cross correlation function to align AFM images taken from the same area on a sample.⁸³ We have decided to test an image registration method used by the medical imaging community called mutual information. This method does not require additional sample preparation and is easy to implement and test in MATLAB. Mutual information and variants of the algorithm have been used widely to register positron emission tomography (PET), magnetic resonance images (MRI) and computed axial tomography scan images (CAT scan).^{61,62} In brief, mutual information is a pixel intensity measure based upon the assumption that similar features in two different images will have similar gray values for all corresponding points in a specific region and images are registered when the variance of the ratio of gray values for corresponding points is

minimal.⁶³ A more detailed description can be found in Chapter 3. We have applied the mutual information algorithm to register images from XPS, AFM and LSCM.

This portion of the dissertation focuses on the development of methods to register and fuse images from AFM, imaging XPS and confocal microscopy obtained from the same area on a polymer blend. The varying sampling depths of the three techniques will enable a 3-D model be generated without destroying the sample.

The two blends that were analyzed using multi-technique fusion are fluorescein-labeled Poly (styrene)/Poly (butadiene) (PS*/PB) and fluorescein-labeled Poly (styrene)/Poly (methyl methacrylate) (PS*/PMMA).

Polymer Blend: PS/PB*

Polymers are blended to obtain products that have desirable characteristics such as increased strength or thermal stability. One such blend combination is PS and PB; PB is characterized by its good elasticity and low heat build up, but it has poor processability. PS has a high modulus, good dielectric properties and is easy to process. Combining a small amount of the rubbery polymer (PB) with the brittle polymer (PS) gives a final product, also known as high impact polystyrene (HIPS), with increased strength and elasticity.⁸⁴ PS* and PB are widely known to be incompatible polymers, and this blending leads to phase segregation in the bulk and on the surface. This blend combination is thus potentially ideal for multi-technique correlation using AFM, XPS and confocal microscopy. The blend morphology has been previously studied by SEM, TEM and more recently by a combination of Atomic Force Microscopy (AFM), DSC

(Differential Scanning Calorimetry), Fourier transform infrared spectroscopy (FTIR) and dynamic mechanical analysis (DMA).^{7,85} However, none of these studies were from the same area on the sample.

Experimental

Sample preparation

Fluorescein-labeled poly(styrene) (PS*, MW = 8.1 kDa) (excitation λ = 494 nm, emission λ = 518 nm) and poly(butadiene) (PB, MW = 233 .0 kDa) were obtained from Polysciences, Inc. Unpurified materials were used in a 2% (w/v) solution of fluorescein-labeled poly (styrene) and poly (butadiene) in HPLC grade toluene. Solutions containing a 50:50 mixture of the two polymers were allowed to sit for 24h before being solvent cast onto silicon wafers. Prior to the application of solutions, the silicon wafers were first cleaned with acetone and then methanol and dried with nitrogen. Standards were prepared using pure polymers individually in a 2% (w/v) solution followed by deposition on separate silicon wafers for analysis.

The XPS spectra and images were acquired on a Kratos AXIS Ultra photoelectron spectrometer using a monochromatic Al K α source operating at 300 W. The base pressure was 2×10^{-10} Torr and the operating pressure was 2×10^{-9} Torr. Charge compensation was accomplished using low-energy electrons. Standard operating conditions for good charge compensation are -2.8 V bias voltage, -1.0 V filament voltage and a filament current of 2.1 A.

Tapping mode AFM was performed with a Dimension 3100 (Digital Instruments) scanning probe microscope. Topographic and phase images were collected simultaneously at ambient conditions. Commercial Si₃N₄ cantilevers with force constants of 2.5-8.5 N/m, and resonance frequencies between 120-190 kHz were used.

Confocal images were obtained with a BioRad MRC-600 confocal laser-scanning microscope using an argon-ion laser with an excitation wavelength of 488nm in the single channel mode (T1/T2A filter cubes, BioRad, Hercules, CA). The emission wavelength was 518 nm for the fluorescein-labeled polystyrene. Confocal Microscopy images were collected with the BioRad CoMOS software.⁸⁶

Standards

Standards of PB and PS* were analyzed to determine the binding energy at which XPS images should be acquired. The structures of the two polymers are shown in Figure 32. Survey spectra were collected for 120s and core level C1s spectra were collected for 360s at a pass energy of 20 eV for PS* and PB, as shown in Figure 33 (a) and (b). The C 1s spectrum of PS* was fit with two peaks, similar to the fitting used in the XPS polymer handbook for polystyrene.³⁵ No oxidation of the PS* was observed from the C 1s peak. In addition, an O 1s peak was acquired for 300s at 20 eV, shown in Figure 33 (c). It is probably due to the native oxide layer on the surface of the substrate. The PB spectrum

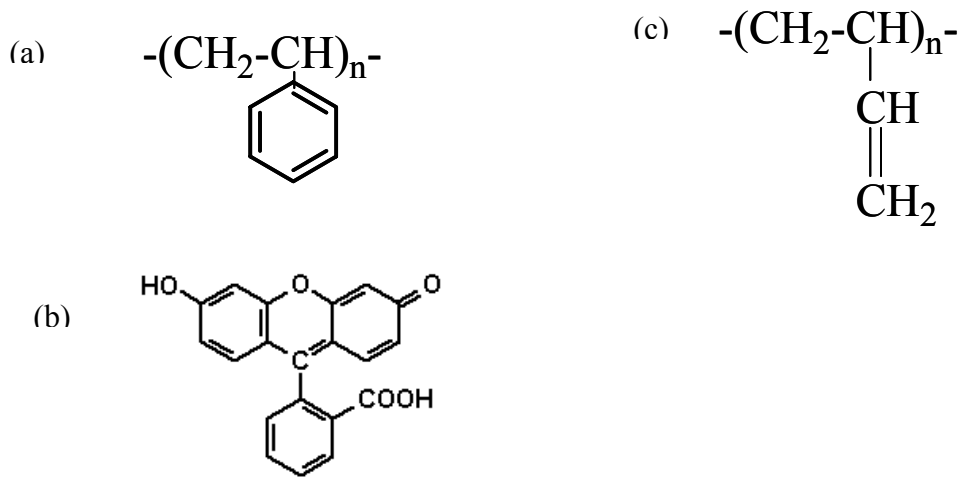


Figure 32. The structure of (a) polystyrene (PS), (b) the fluorescein label attached to polystyrene, and the structure of poly (butadiene) (PB).

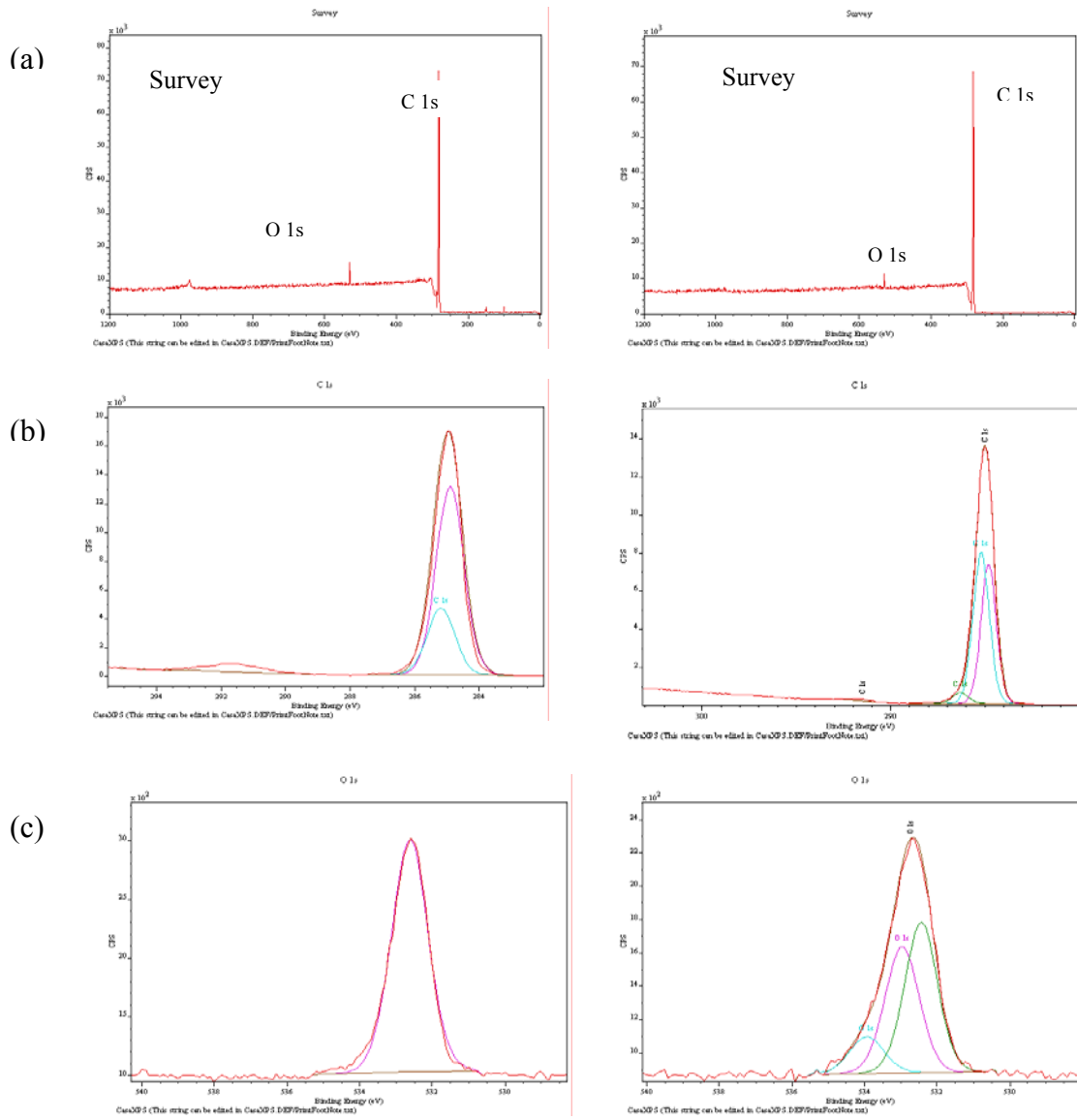


Figure 33. (a) Survey spectra of fluorescein-labeled polystyrene (PS*) and poly(butadiene) standards, respectively (PB). (b) C 1s spectra of PS* and PB standards, respectively (c) O 1s spectra obtained of PS* and PB standards, respectively.

was fit with three peaks; the two peaks at 284.8 and 285.3 eV were fit according to the XPS polymer handbook, and the third peak at 286.3 eV appears to be due to surface oxidation.³⁵ Because there was surface oxidation, an O 1s spectrum of PB was acquired for 300s at 20 eV, shown in Figure 34 (c). Since the C 1s spectra for PS* and PB are virtually identical, valence band spectra were acquired. The valence band spectra were acquired between 0 and 40 eV at a pass energy of 40 eV for 600s, shown in Figure 34.

Blend Analysis

In order to obtain data from the same area on the sample, the analysis area has to be located and marked. To aid in locating the box using imaging XPS and AFM, a locator grid is placed over the sample before AFM lithography to simplify area location using XPS or LSCM. This confines the area in which the box is drawn to the dimensions of a single grid square, 420x420 μm^2 in this case. Within one of the grid squares, an area is marked using AFM lithography. In AFM lithography the tip is scanned under load forces that are experimentally determined to remove sample from the surface to make patterns on the surface. For this experiment, two parallel lines are made, $\sim 80 \mu\text{m}$ long and $\sim 120 \mu\text{m}$ apart, as shown in Figure 35.

Before imaging inside the lines with the AFM, the center of the area from which the AFM images were to be taken is noted. This is done by moving to the right a distance of $\sim 70 \mu\text{m}$ from the top left of the left parallel line and moving down 40 μm . This area is the center from which the AFM images are acquired, illustrated in

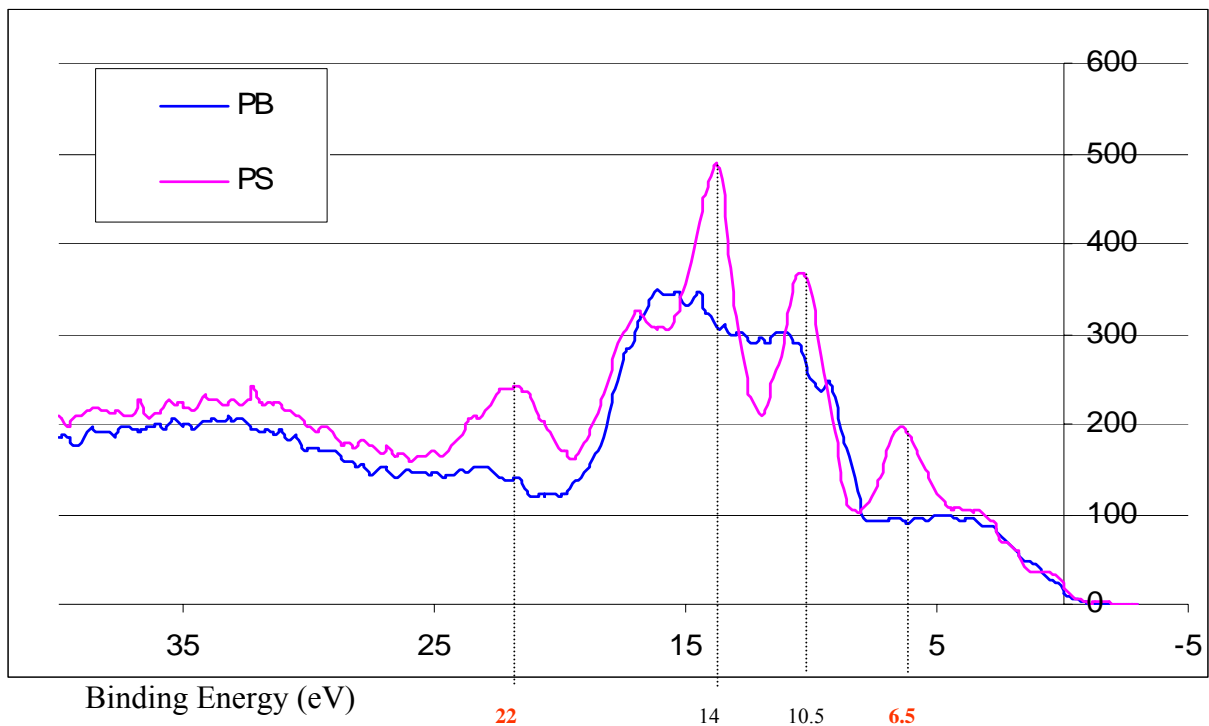


Figure 34. Valence band spectra of poly (styrene) and poly (butadiene). There are differences in the two spectra, which can be used for imaging.

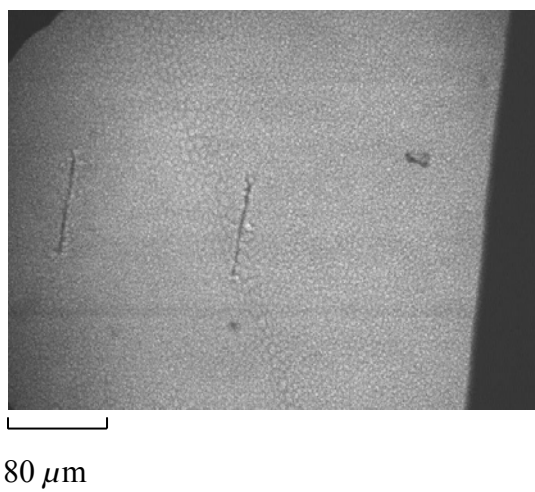


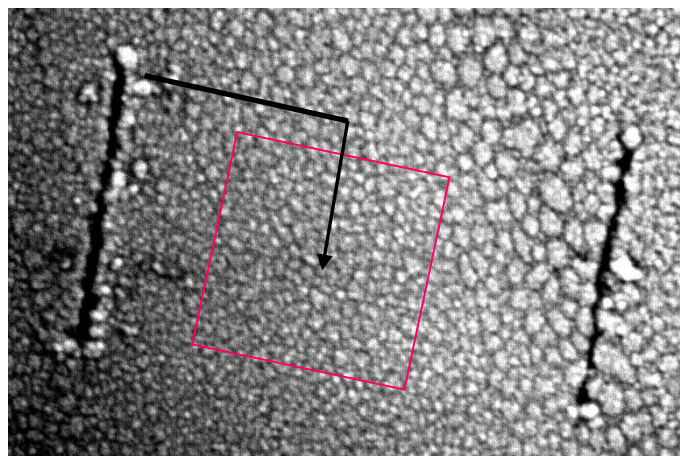
Figure 35. An optical image of the lines drawn with the AFM. The lines are $\sim 80 \mu\text{m}$ long and $\sim 120 \mu\text{m}$ apart.

Figure 36 (a). A tapping mode topography image is acquired from this area, as shown in Figure 36 (b). The area is then located and analyzed by confocal laser-scanning microscopy. A series of $185 \times 123 \mu\text{m}^2$ images are collected at $0.7 \mu\text{m}$ increments throughout the sample using a 40x objective and a 5x zoom. There are a total of 63 confocal images in the stack of images acquired. Some of the confocal slices are shown in Figure 37.

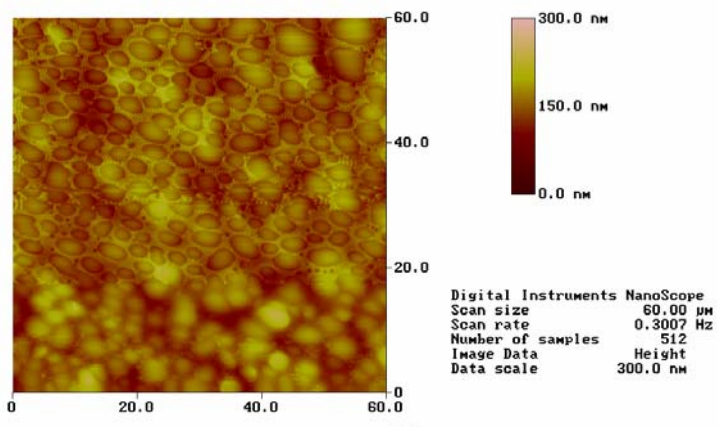
The mean of image slices 9-25 is used in this research. These slices are chosen by visual inspection of all the image slices. Image slice 9 represents the slice where image features just come into focus. Image slices beyond 25 appear out of focus, and thus were not used. The mean of slices 9-25 is calculated using MATLAB.⁶⁶

Imaging XPS Results

The marked area is located optically and XPS images are acquired with the marked area in the field of view. An O 1s image is acquired at 529.5 eV, as shown in Figure 38(a). This binding energy corresponds to the oxygen present in the fluorescein-labeled poly(styrene). The image was homogenous and the features did not appear to look like features observed in the AFM and confocal images previously acquired. A C 1s image acquired at 288.5 eV, shown in Figure 38(b) corresponds to the shake-up satellite peak that occurs for systems with aromatic structures and unsaturated bonds such as PS and PB. The intensity in the image is low and the surface appears homogenous. A C 1s image was acquired at 285.0 eV, the main



(a)



(b)

Figure 36. (a) The area from which the AFM topography image was taken.

(b) A tapping mode AFM topography image of a 50:50 fluorescein-labeled poly (styrene)/ poly (butadiene) blend obtained inside the area marked using AFM.

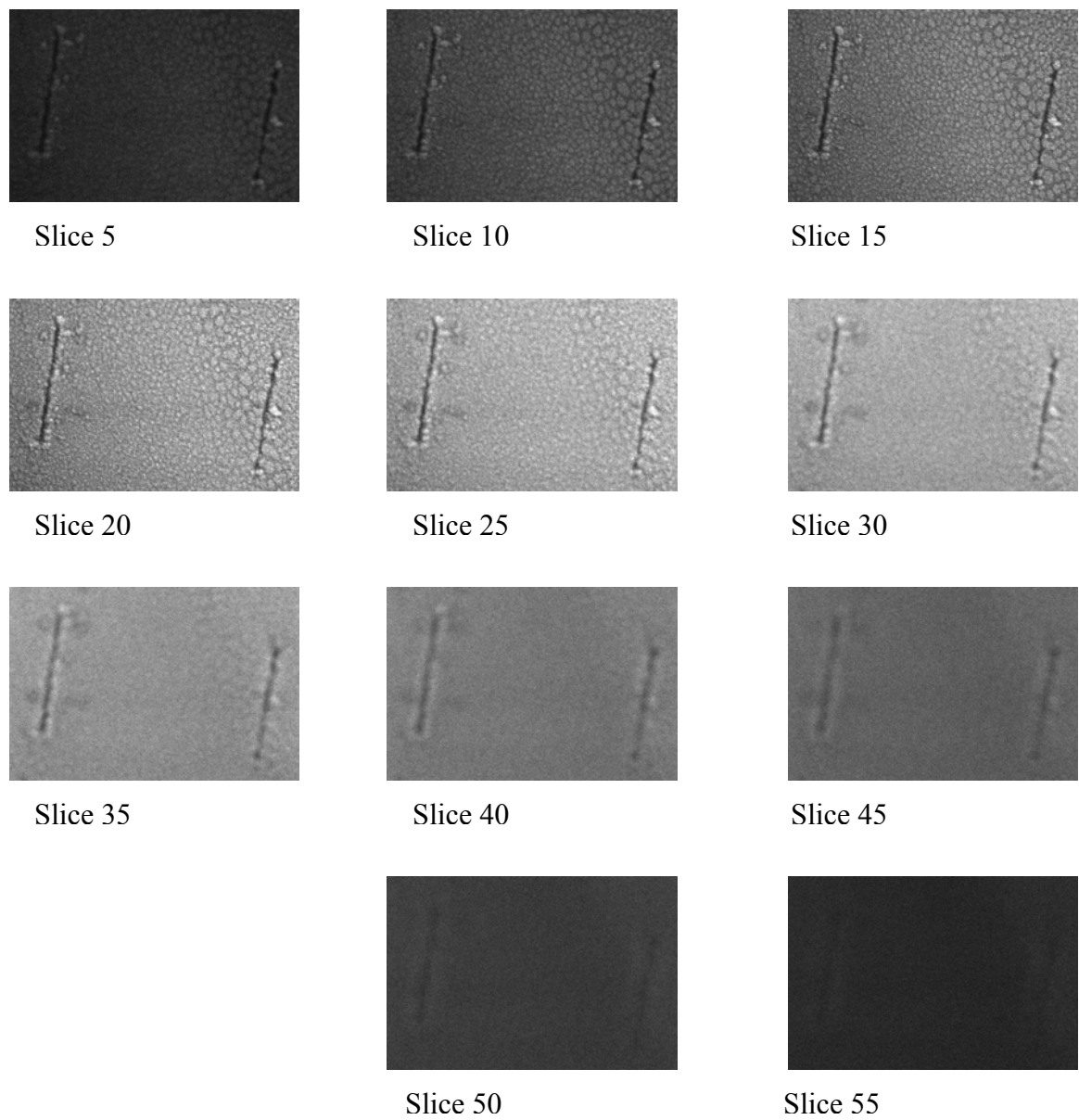


Figure 37. Representative confocal slices ($185 \times 123 \mu\text{m}^2$) of the PS*/PB blend.

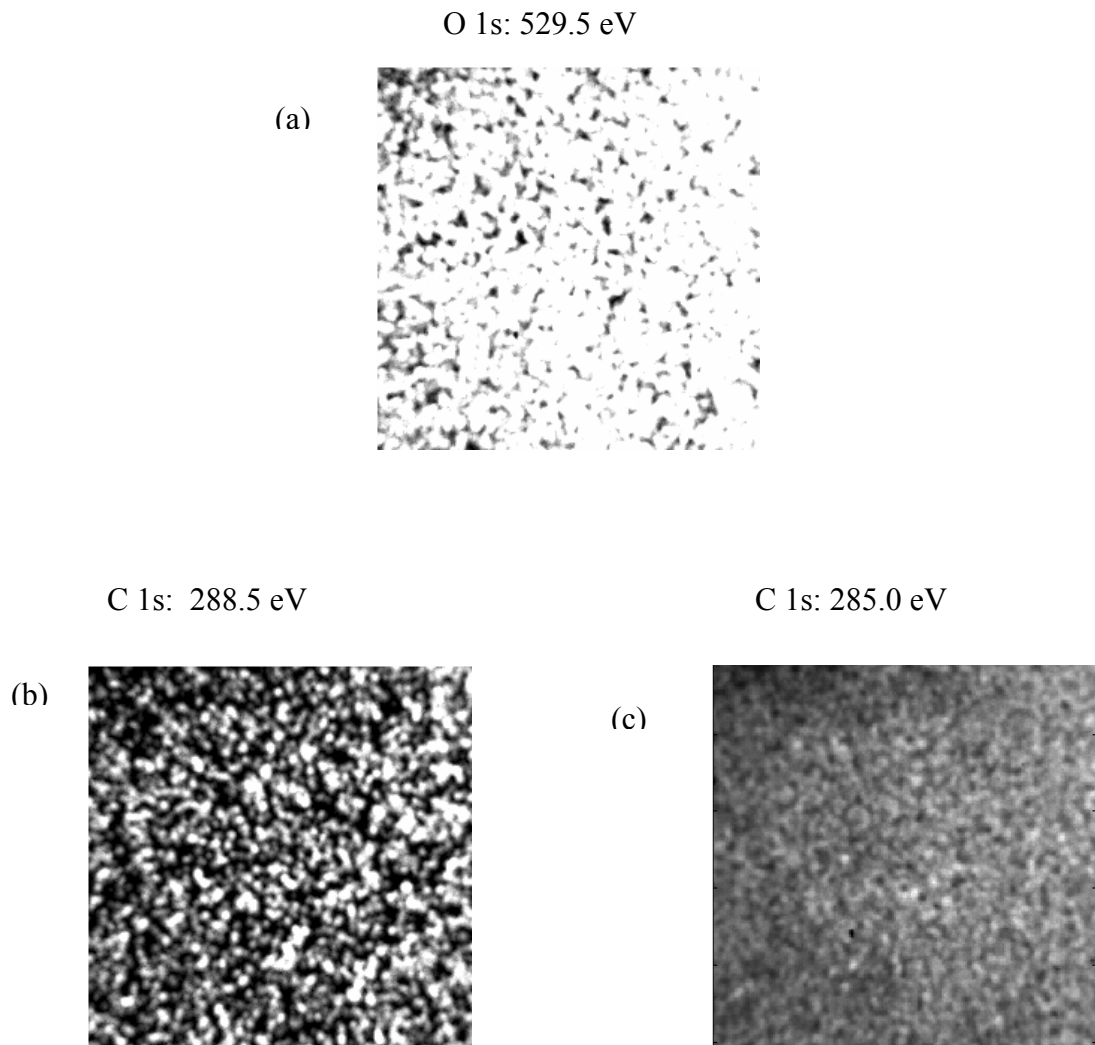


Figure 38. High magnification ($200 \times 200 \mu\text{m}^2$) XPS images taken from the marked area of the 50:50 PS*/PB blend. (a) O 1s image taken at a binding energy of 529.5 eV. (b) C 1s shake-up satellite image taken at 288.5 eV. All of the images appear homogenous and do not represent one particular chemical phase. (c) C 1s image taken at a binding energy of 285.0 eV.

carbon peak in the spectrum, shown in Figure 38(c) Again, the features in the image appear rather homogenous. This is expected since the molecular structures of PS* and PB are similar; therefore, there will not be significant differences in core level shifts in the spectra between the two polymers. Additionally, both polymers have shake-up structures as shown in Figure 33.

One alternative is to use the valence band region for imaging. The valence band region may show structural differences for polymers with identical core level spectra as shown for the PS* and PB. This region is similar to the fingerprint region found in infrared spectra. It has been previously used to differentiate between different isomers of PBMA. The valence bands for PS* and PB are shown in Figure 34. There is overlap between the valence band structures, but peaks at 22eV and 6.5eV are representative of PS*. A series of valence band images were collected for 600s at 22eV, 14eV, 10.5eV and 6.4eV, shown in Figure 39. The acquired images, shown in Figure 39, have similar features to those observed in the confocal and AFM images, but it's difficult to conclusively identify them as actual features or noise in the images. To remove the noise from the images, principal component analysis was applied to the series of images. The score images and their respective loadings are shown in Figure 40. Because the data was not mean centered, the first principal component image is considered to be the mean image with positive contributions from all of the variables (binding energy) in the loadings. The second principal component image has a significant positive contribution at 10.5 eV. However, this is an area of overlap between the PS* and PB in the valence band spectra, so the image

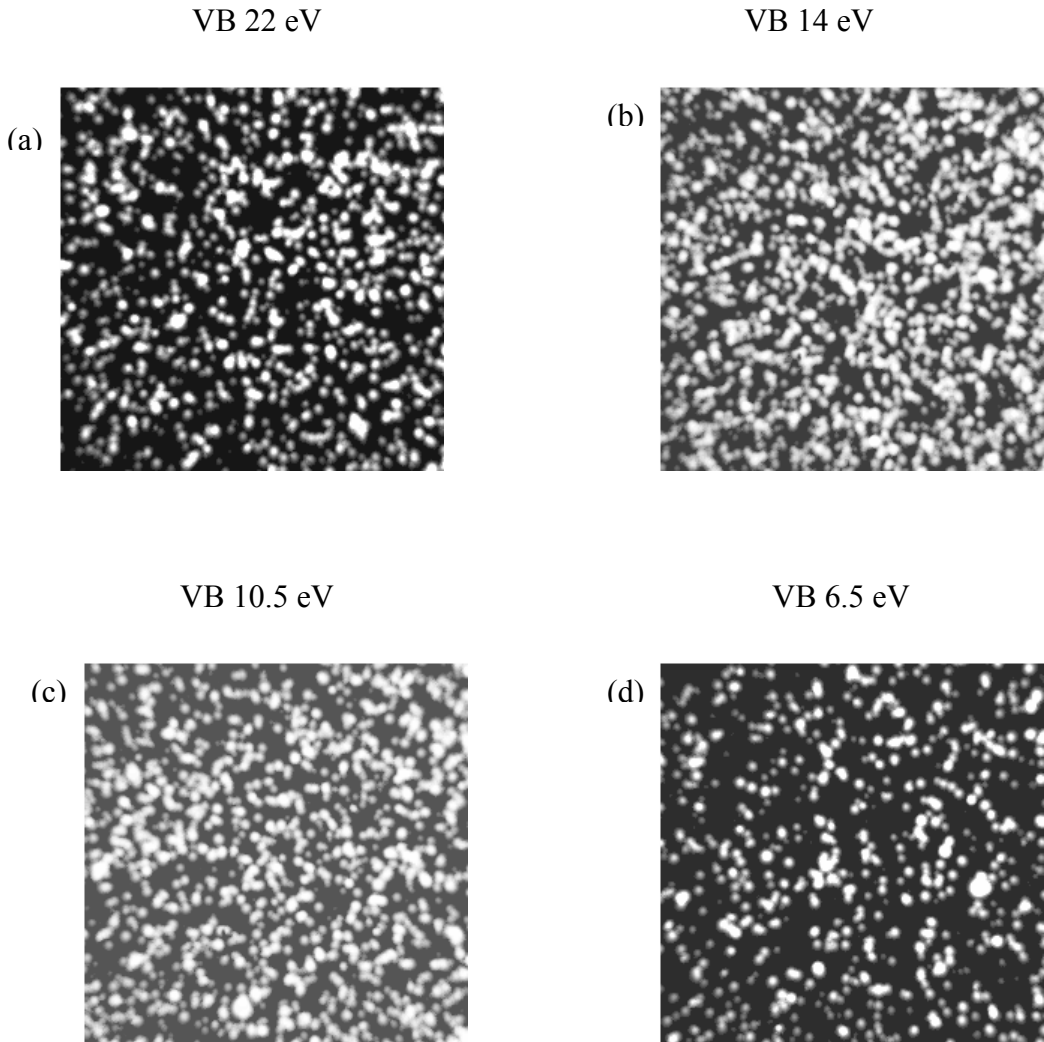


Figure 39. High magnification ($200 \times 200 \mu\text{m}^2$) XPS valence band images taken at different binding energies from the marked area of the 50:50 PS*/PB blend. (a) 22 eV. (b) 14 eV (c) 10 eV (d) 6.5 eV.

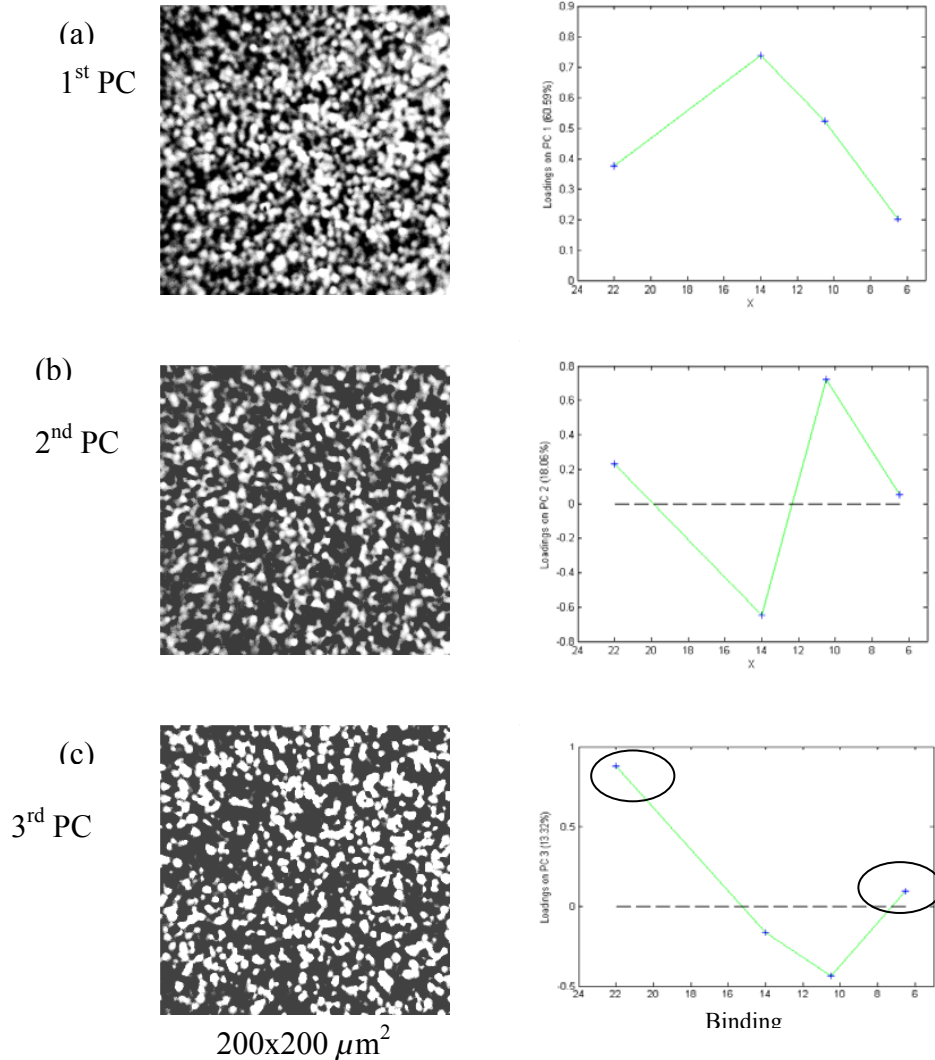


Figure 40. Principal component images and loadings obtained from Principal Component Analysis. (a) First principal component image and loadings. The loadings show positive contributions from all the variables and the image is not representative of one particular chemical phase. (b) 2nd Principal component image and loadings. The loadings show a large contribution at 14 eV, but this is the area of overlap between PS* and PB, so the image is not representative of PS* or PB. (c) 3rd Principal component image and loadings. The loadings show a large positive contribution at 22 eV and a smaller contribution at 6 eV; these binding energies are representative of the PS* phase.

is not representative of a single polymer phase. The 3rd principal component image shows a significant positive contribution from the PS* peak at 22eV and smaller positive contribution at 6.5 eV, also indicative of PS*; therefore, the features in the image are representative of a PS*-enriched image. When the third principal component image is compared with the original valence band image taken at 22 eV, shown in Figure 41, the features in the two images are identical giving increased confidence that the image is indeed a PS*-enriched image.

Image Preprocessing

AFM, XPS and confocal images were imported into MATLAB. In MATLAB the images were resized in terms of microns/pixel. The AFM images are .11 microns/pixel; XPS images are .78 microns/pixel; confocal images are .24 microns/pixel. The resolution of the XPS images can be increased, but it is computationally expensive; therefore, the resolution of the AFM and confocal images were decreased to .78 microns/pixel to have the same physical size. Prior to image registration of all three images, the AFM 60x60 μm^2 topography image and the confocal image, taken from the mean of slices 9-25, were histogram equalized. This converts all images to similar intensity distributions and produces more contrast in the image allowing for better registration of the images. A more detailed discussion of histogram equalization can be found in Chapter 3.

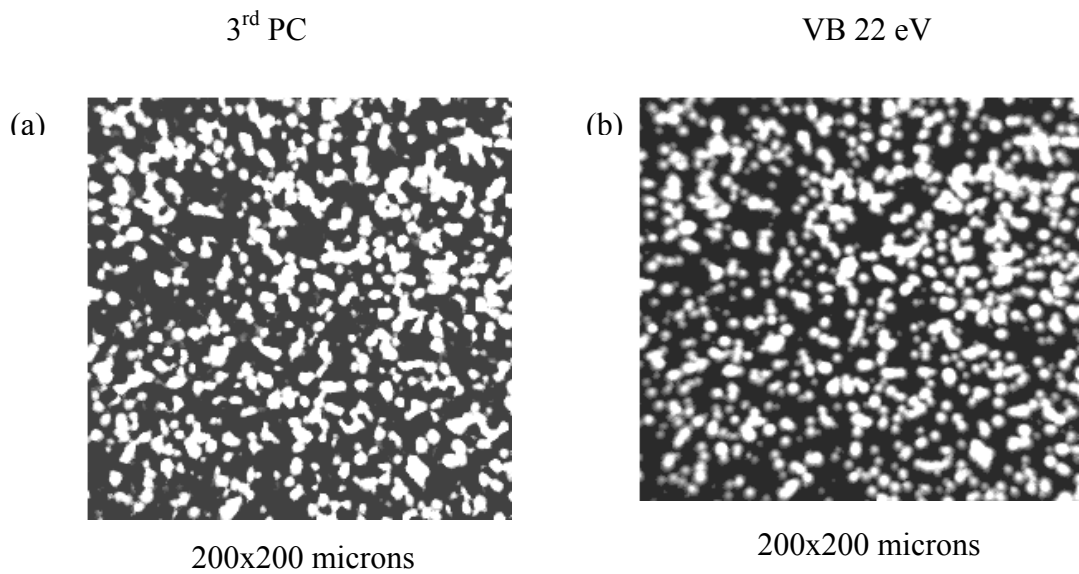


Figure 41. (a) 3rd Principal component image obtained from Principal Component Analysis. (b) Valance band image obtained at 22 eV. The features in the both images are the same, helping to confirm that the 3rd principal component image is indeed a *PS enriched phase.

Image Registration of XPS, AFM and Confocal Images

The third step in image fusion is image registration, discussed in Chapter 3. The accuracy of the mutual information program was tested by acquiring two AFM images; the first image was a 40x40 micron image of a 50:50 blend of fluorescein-labeled poly (styrene) and poly (butadiene) and the second image was a 20x20 μm^2 image obtained from the center of the 40x40 μm^2 area of the first image. If the program works properly, the images should register. The output for the program is two pixel locations, I and J. I is the vertical distance in pixels from the top of the reference image and J is the horizontal distance in pixels from the left side of the reference image. Therefore, I and J are the coordinates in the image to which an image B, registers with image A. The features in the 20x20 μm^2 image overlap with corresponding features in the 40x40 μm^2 shown in Figure 42. This demonstrates that the mutual information program is working accurately.

The mutual information program is then used to register AFM, confocal and XPS images acquired from the same area of the PS*/PB. The 60x60 μm AFM topography image is used for registration. For confocal microscopy the mean image for slices 9-25, shown in Figure 43, is used for image registration. XPS principal component image 3, calculated from the XPS valence band images, is used for image registration with AFM and confocal.

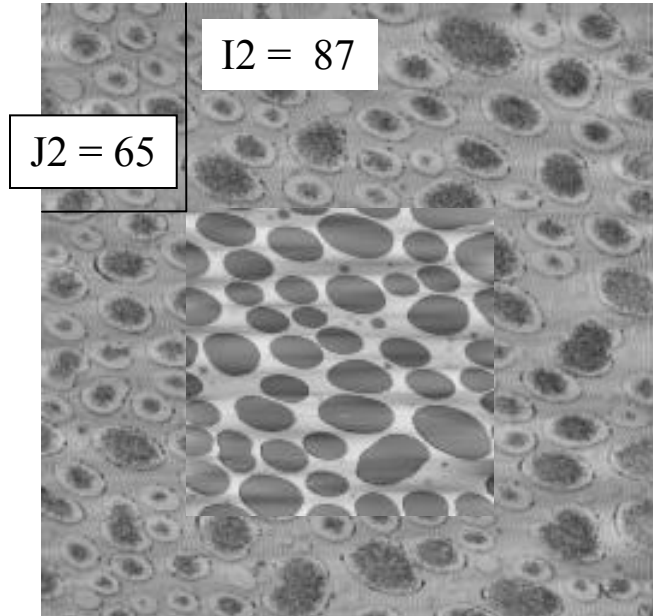


Figure 42 (a) Image registration using mutual information has been performed using two gray scale AFM phase images from a 50:50 blend of fluorescein-labeled poly (styrene) and poly (butadiene). A $40 \times 40 \mu\text{m}^2$ phase image was acquired from the blend and a smaller $20 \times 20 \mu\text{m}^2$ phase image (inset) was obtained from the center of that area. The smaller image, $20 \times 20 \mu\text{m}^2$, has been registered with the larger $40 \times 40 \mu\text{m}^2$ image. The coordinates of registration are $I = 65$ and $J = 87$. It can be seen that features from the two images overlap, providing a successful registration.

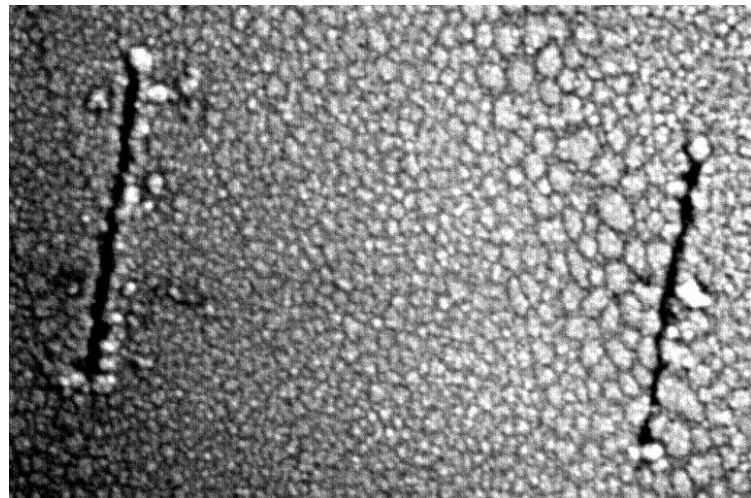


Figure 43. A $185 \times 123 \mu\text{m}^2$ confocal image of the marked area on the PS*/PB blend sample. Also shown is the area from which the AFM topography image was taken.

The confocal and AFM images are registered using the mutual information program that was written in MATLAB.⁶⁶ The coordinates of registration for the AFM image with the confocal image is I = 222 and J = 326. The registered images are shown in Figure 44. This $60 \times 60 \mu\text{m}^2$ area is cropped from the confocal image. The XPS image is then separately registered with the AFM and confocal images using the mutual information program written in MATLAB.⁶⁶ The output for registering the AFM image with the XPS principal component image is I = 45 and J = 146. I = 45 and J = 145 were the coordinates for the registration of the confocal image with the XPS principal component image. The registered $60 \times 60 \mu\text{m}^2$ area is located within the $200 \times 200 \mu\text{m}^2$ XPS principal component image and cropped. Similar registered coordinates for the AFM and confocal images help to confirm this registration method. The registered XPS principal component image, registered confocal image, and the AFM image are shown in Figure 45.

Comparing the registered AFM image with confocal image, it can be seen that similar size and shape features are observed in the two images. Additionally, intensities in both images match, that is, where there are bright features in the AFM image there are bright features in the confocal image. This agreement shows that there is a correlation between the topographical features observed in the AFM and fluorescent textures in the confocal images. This indicates surface segregation of PS*. A comparison of the confocal image with the XPS image shows some similarities in the images can be observed; however, the XPS image does not contain as many features as the AFM and confocal images. XPS is a lower resolution technique with a

lateral resolution of 2-5 μm for imaging. This means that many of the features observed in the AFM and confocal images would be merged, forming a continuous feature rather than the individual domains found in the AFM and confocal images. Secondly, the absence of intensity in the image does not necessarily mean that nothing is there; it may mean that there is less of that constituent present in that area. Since the image display depends upon an intensity scale, the intensity thresholds in the image can be changed to include more or less intensity in the image, corresponding to more or less features in the image. Because of the absence of features in the XPS image compared to the AFM and confocal images, merging the three images into a three dimensional model becomes difficult.

This work demonstrates the use of valence band imaging for systems, in which core level distinction is not possible. Mutual information applied to images without obvious unique reference points give consistent results. This led to confocal fluorescence images and AFM topography images that correlate well. Additionally, the analysis area can be quantified using small area valence band spectroscopy and multiple linear regression, but this was not possible at the time of data acquisition. Work on this polymer blend system is continuing.

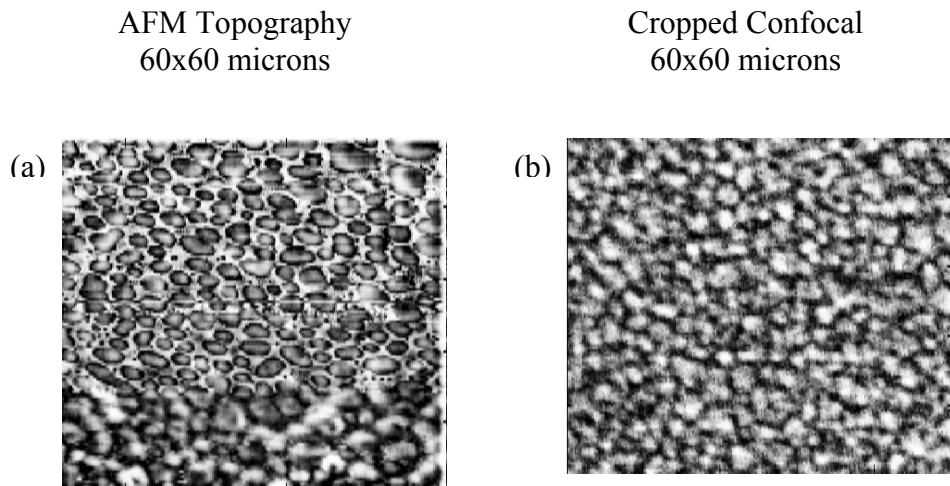


Figure 44. The AFM topography image is registered with the confocal image using mutual information. The I and J values obtained for the image registration coordinates were I=222 and J=326. The $60 \times 60 \mu\text{m}^2$ AFM topography image is shown in Figure 44(a). (b) The registered $60 \times 60 \mu\text{m}^2$ confocal image is shown in Figure 44 (b).

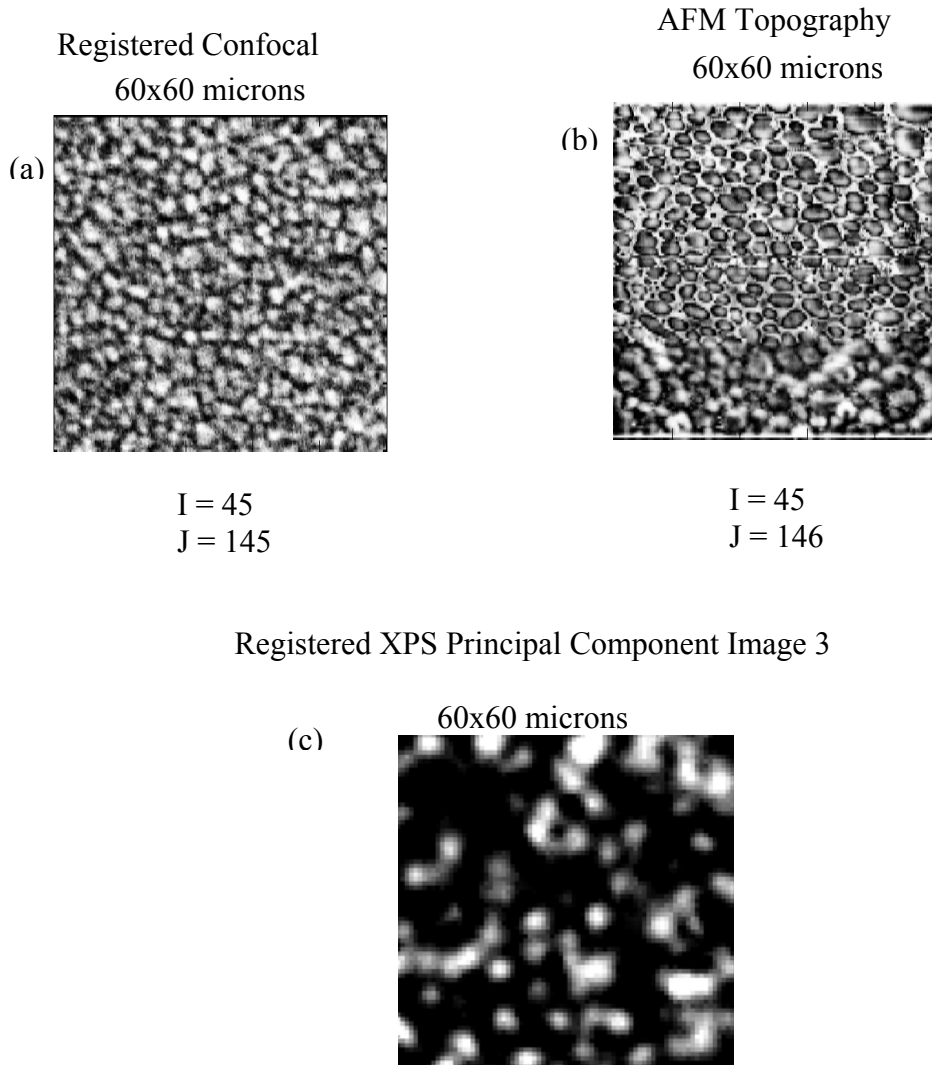


Figure 45. The AFM topography image and the cropped confocal image of the PS*/PB blend are independently registered with the XPS 3rd principal component image. (a) AFM topography image is registered with the XPS image using I and J values of 45 and 145, respectively. (b) The registered confocal image is registered with the XPS image using I and J values of 45 and 146, respectively. (c) Registered 60x60 μm^2 XPS image.

Polymer Blend: PS/PMMA*

The polystyrene (PS)/poly(methyl methacrylate) (PMMA) blend is a classic model system for polymer phase segregation studies, making the system suitable for multi-technique studies using AFM, XPS and confocal microscopy. PS/PMMA blends have been proposed for use in magnetic storage media, antireflective coatings, and biomaterials.⁸⁷ This has brought about increased interest in characterizing the blend to gain a better understanding of the system. Multi-techniques studies have been conducted in the past. Ton-That et al. studied the influence of the concentration and composition of PS/PMMA blends on the morphology and composition of the surface of films with XPS and AFM.¹⁹ Dekeyser et al. utilized XPS, AFM and SIMS to characterize the surface composition of PS/PMMA blends.⁸⁷ However, none of the multitechnique data was obtained from the same area on the sample.

Experimental

Sample preparation

Fluorescein-labeled poly (styrene) (PS*, MW = 8.1 kDa) (excitation λ = 494 nm, emission λ = 518 nm) was obtained from Polysciences, Inc and poly (methyl methacrylate) (PMMA, MW = 75 kDa) was obtained from Scientific Polymer Products.

Unpurified materials are used in a 2% (w/v) solution of fluorescein-labeled PS* and PMMA in HPLC grade chloroform. Solutions containing a 50:50 mixture of

the two polymers are allowed to sit for 24h before being solvent cast onto silicon wafers. Prior to the application of solutions, the silicon wafer is first cleaned with acetone, then methanol and dried with nitrogen. Standards were prepared using pure polymers individually in a 2% (w/v) solution followed by deposition on separate silicon wafers for analysis.

Standards

Standards of PMMA and PS* are analyzed to determine the binding energy at which XPS images should be acquired. The structures of the two polymers are shown in Figure 46. Survey spectra were collected for 120s for PS* and PMMA as shown in Figure 47(a). Core level C1s spectra are collected for 360s at a pass energy of 20 eV for PS* and PMMA as shown in Figure 47 (b). The C 1s spectrum of PS* was fit with two peaks, similar to the fitting used in the XPS polymer handbook for polystyrene.³⁵ No oxidation of the PS* was observed from the C 1s curve-fit. In addition, an O 1s peak was acquired for 300s at 20 eV, shown in Figure 47 (c). It appears at a binding energy of 532.6 eV and is probably due to the native oxide layer on the surface of the silicon substrate. The C 1s peak of PMMA was also fit according to the XPS polymer handbook, and no oxidation was observed from the C 1s spectrum. The curve-fit O1s peak of PMMA is shown in Figure 47 (c).

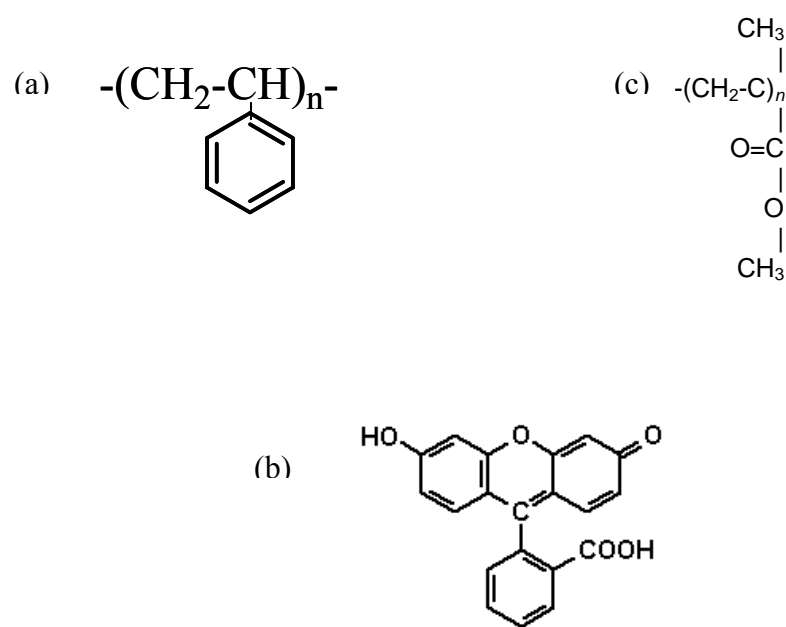


Figure 46. The structure of (a) polystyrene (PS), (b) the fluorescein label attached to polystyrene, and (c) the structure of poly (methyl methacrylate) (PMMA).

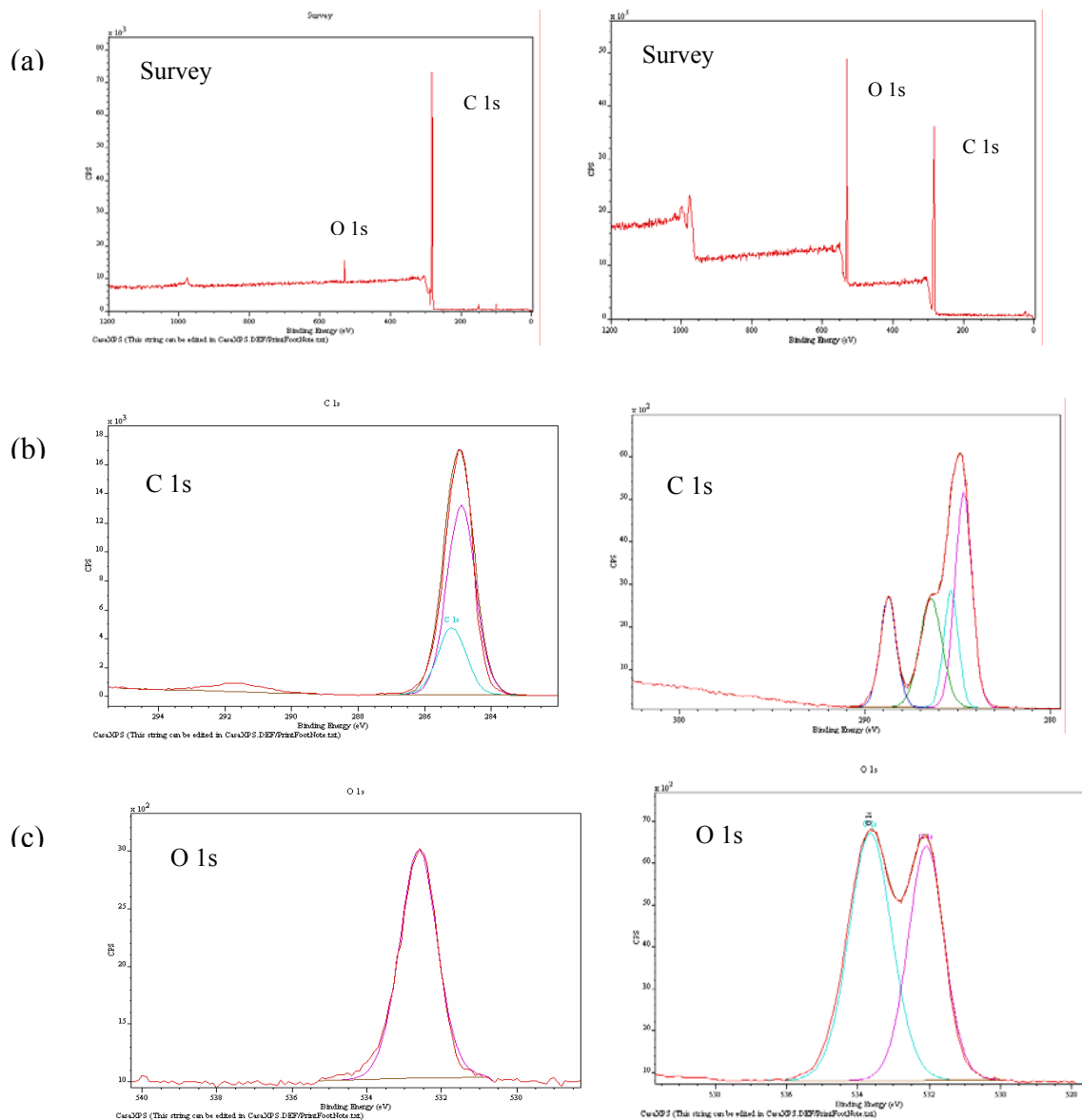


Figure 47. (a) Survey spectra of fluorescein-labeled polystyrene and poly (methyl methacrylate) (PMMA), respectively. (b) C 1s spectra of PS* and PMMA. (c) O 1s spectra of PS* and PMMA standards, respectively.

Blend Analysis

In order to obtain data from the same area on the sample, the analysis area has to be located and marked. A locator grid is placed over the sample before AFM lithography. This confines the area in which the box is drawn to the dimensions of a single grid square. Within one of the grid squares, an area is marked using AFM lithography. For this experiment, two parallel lines are made, $\sim 80 \mu\text{m}$ long and $\sim 120 \mu\text{m}$ apart. An optical image of the lines is shown in Figure 48.

Before imaging inside the lines with the AFM, the center of the area from which the AFM images were to be taken was noted. This is done by moving the AFM tip a distance of $\sim 40 \mu\text{m}$ to the right from the top left of the left parallel line and moving down $\sim 50 \mu\text{m}$. This area is the center from which the AFM images were acquired. Tapping mode and phase images were acquired simultaneously from this area. Images are shown in Figure 49 (a) and (b). The area is then located and analyzed by confocal laser-scanning microscopy. A series of $185 \times 123 \mu\text{m}^2$ images are collected at $0.7 \mu\text{m}$ increments throughout the sample with a 40x objective and a 5x zoom. The total number of confocal images in the series was 95. Some confocal slices are shown in Figure 50. The PCA program in MATLAB was used to extract three principal components from the 95 image slices, shown in Figure 51. The loadings from the first principal component show a gradient from image slices 20-45. Slices before image 20 are believed to be coming from air, while slices after 45 are coming from the silicon substrate. This is consistent with what is observed upon visual

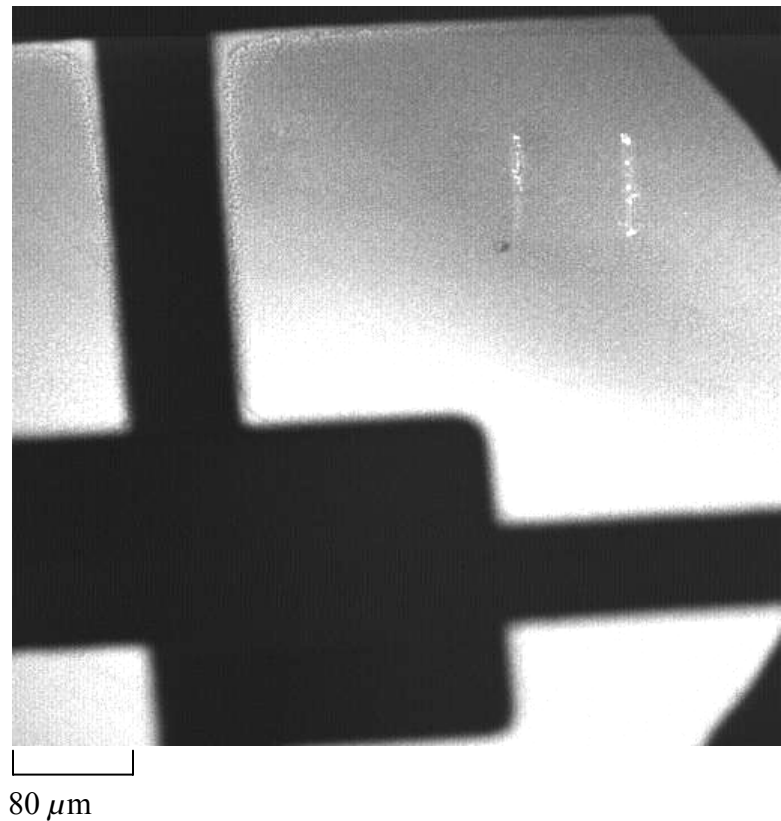


Figure 48. An optical image of lines drawn with the AFM on a PS*/PMMA blend.

The lines are $\sim 80 \mu\text{m}$ long and $\sim 120 \mu\text{m}$ apart.

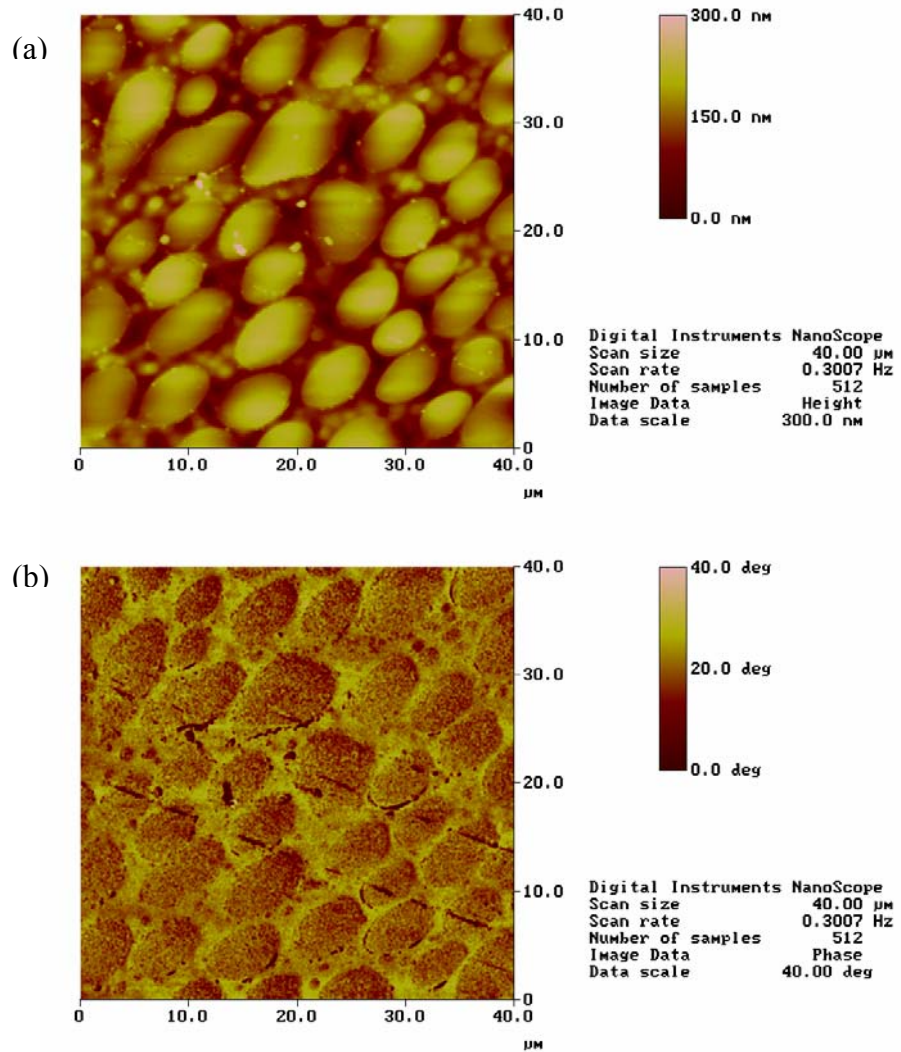


Figure 49. A $40 \times 40 \mu\text{m}^2$ tapping mode AFM (a) topography and (b) phase image of a 50:50 PS*/PMMA blend obtained inside the sample marked area.

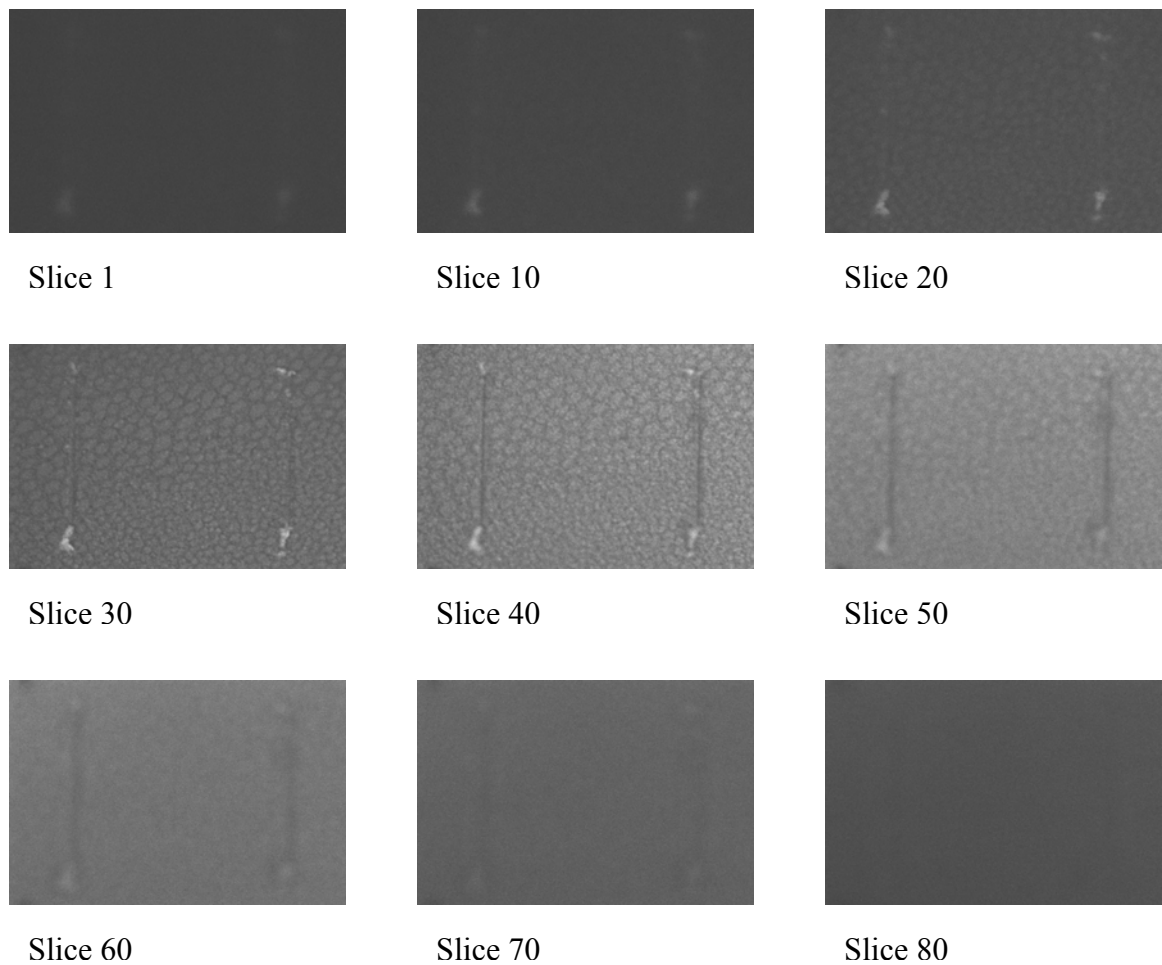


Figure 50. Representative confocal slices ($185 \times 123 \mu\text{m}^2$) taken from the PS*/PMMA blend.

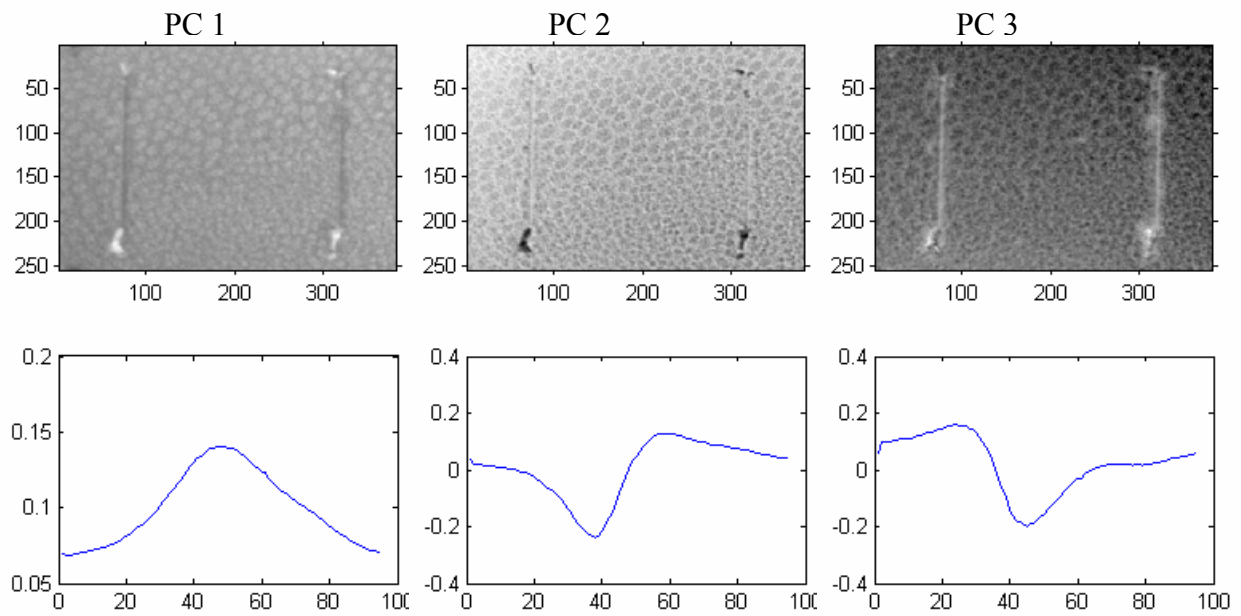
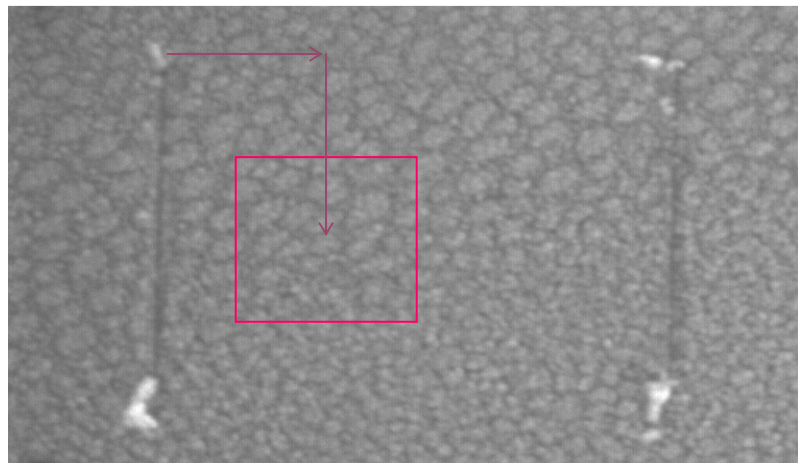


Figure 51. Principal component scores and loadings (a) first principal component, (b) second principal component (c) third principal component

inspection of the images. Therefore, the first principal component score image is used in this research. A larger image of the first principal component score image is shown in Figure 52. Also shown is the area from which the AFM images were acquired.

Imaging XPS Results

The marked area was located optically with the lines in the field of view of the analysis area. C 1s images were acquired at 288.5, 286.1, 283.7, 282.3, and 281.7 eV at a pass energy of 80eV for 360s each. The images are shown in Figure 53. In addition, two background images were obtained at 290 eV and 280 eV at a pass energy of 80eV for 360s each. Principal component analysis was applied to this multivariate data set to extract a phase that is representative of PS*. PCA was carried out in MATLAB. Three principal components were extracted. The scores and loadings for principal component image one are shown in Figure 54 (a). Principal component one has a positive contribution at 288.5 eV and a large positive contribution at 290 eV, which is representative of the background image collected, thus the image is not representative of a particular phase. The loadings for principal component two, shown in Figure 54 (b), shows a small positive contribution at 288.5 eV due to the shake-up peak from PS*, and a larger positive peak at 281.7, representative of the C 1s peak from PS*. The scores and loading for principal component three are shown Figure 54 (c). There is a large positive contribution at



$185 \times 123 \mu\text{m}^2$

Figure 52. $185 \times 123 \mu\text{m}^2$ confocal image of the marked area on the PS*/PMMA blend sample. Also shown is the area from which the AFM topography and phases image were taken.

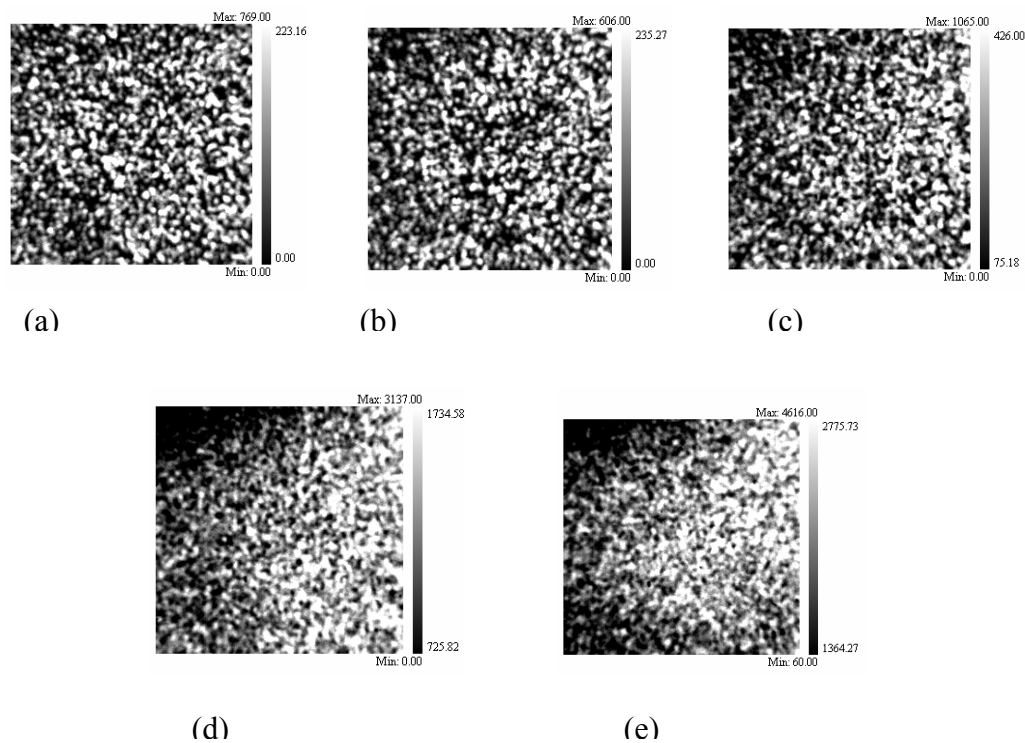


Figure 53. C 1s images of the PS*/PMMA blend taken at (a) 288.5, (b) 286.1, (c) 283.7, (d) 282.3, and (e) 281.7 eV

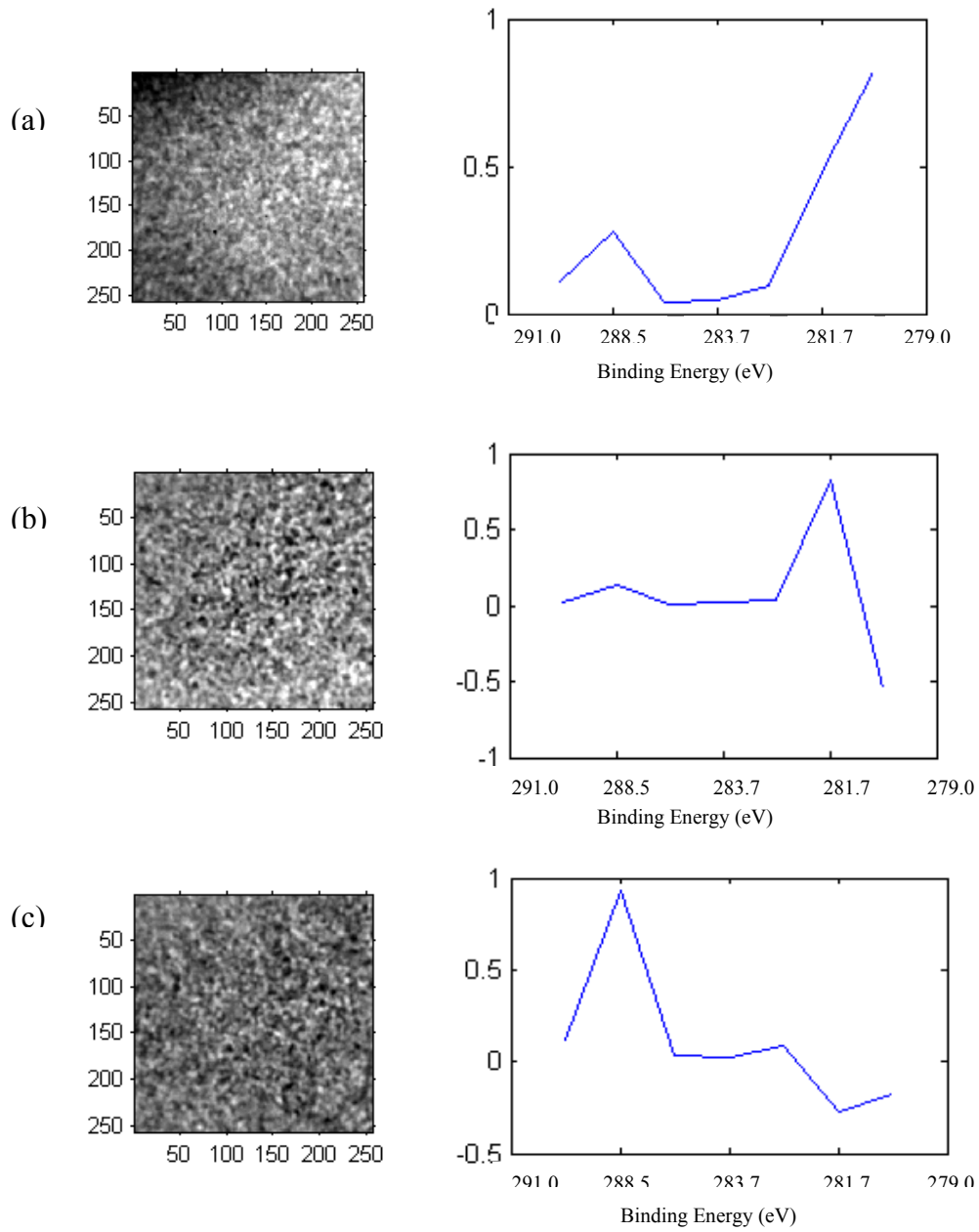


Figure 54. Principal component scores and loadings (a) first principal component, (b) second principal component (c) third principal component

288.5 eV, due to the shake-up satellite, but there is not a positive contribution at 281.7, which would be representative of PS*. Therefore, the image is not representative of a particular phase. The 2nd principal component image, representative of a PS* phase, is used for image registration.

Image Preprocessing

AFM, XPS and confocal images are imported into the MATLAB program. In MATLAB⁶⁶ the images are resized in terms of microns/pixel. The AFM images are .11 microns/pixel, XPS images are .78 microns/pixel and confocal images are .24 microns/pixel. The resolution of the XPS images can be increased, but it is computationally expensive; therefore, the resolution of the AFM and confocal images were decreased to .78 microns/pixel to have the same physical size. Prior to image registration of all three images, the AFM 60x60 μm^2 topography image and 1st principal component score image are histogram equalized. This produces more contrast in the image, allowing for better registration of the images. A more detailed discussion of histogram equalization can be found in Chapter 3.

Image Registration of AFM, XPS, and Confocal Images

The third step in image fusion is image registration. Mutual information, discussed in Chapter 3, was used to register the AFM, confocal 1st principal component score image and the XPS principal component image. The 60x60 μm^2

AFM topography image is used for registration. For confocal microscopy the first principal component score image is used for image registration, previously shown in Figure 52. The principal component image calculated from the XPS C 1s images is used for registration, as previously discussed.

The confocal and AFM images are registered using the mutual information program in MATLAB. The coordinates of registration for the AFM image with the confocal image are I = 209 and J = 161. The AFM and confocal images are then registered with the XPS image. This area is then cropped out of the confocal image. The output for registering the AFM image with the XPS principal component image is I = 10 and J = 141. I = 8 and J = 129 are the coordinates for the registration of the confocal 1st principal component image with the XPS principal component image. The registered area is cropped from the 200x200 μm^2 , XPS principal component image. All three registered images are shown in Figure 55.

Comparing the registered AFM image with the confocal image it can be seen that similar size and shape features are observed in the two images. The intensities in the two images are inverses of each other. The bright regions in the confocal principal component image are PS*. The domains observed in the AFM phase contrast image are believed to be PS* domains. Kailas et al. have previously reported the formation of droplet-like domains on a PMMA layer by ToF-SIMS and phase contrast AFM.^{88,89} Since PMMA prefers hydrophilic substrates like silicon with a native oxide layer, it is expected to segregate to the substrate interface. The XPS principal component image is representative of PS* on the surface. The domains in

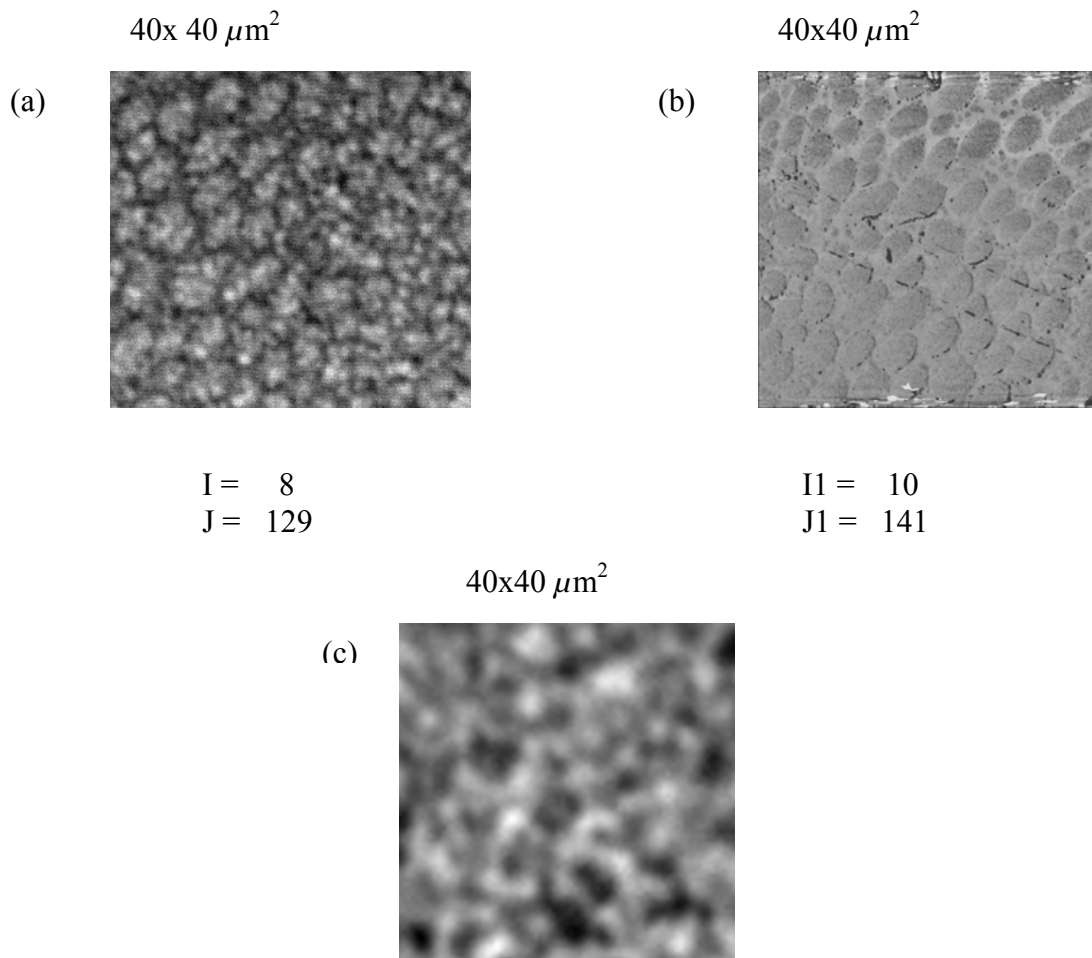


Figure 55. The AFM phase image and the registered confocal image are independently registered with the XPS principal component image. (a) The confocal 1st principal component image is registered with the XPS image with I and J values of 8 and 129, respectively. (b) The AFM phase image is registered with the XPS image with I and J values of 10 and 141, respectively. (c) 40x40 μm^2 XPS image that the confocal principal component was registered to. (d) 40x40 μm^2 XPS image that the AFM phase image was registered.

the XPS image appear merged, making it difficult to find similarities in the image; however, there are some regions in the image that have similar intensities. These images can be used to create a 3-D volume, which will be described in the next section.

Quantification of Confocal Images by XPS

Fusing confocal and XPS data provides a benefit of extended spatial coverage. Confocal microscopy provides information on how features change as a function of depth, but the data is not quantitative. The fluorescence intensity from a confocal image is proportional to concentration, but the technique is not generally used as a quantitative method. Conversely, XPS is a quantitative method that can be used to calculate concentrations from different areas on the surface. Spectra can be acquired from areas of interest within the images, and XPS images can be quantified directly. Confocal-XPS fusion involves the use of quantitative information obtained from the surface of the top of the sample and, ideally, the surface of the bottom of the sample. The XPS quantitative information is used to quantify confocal images and build a quantitative confocal volume, where each pixel represents a concentration of a particular chemical phase. The XPS, AFM topography and confocal images from the previous section are used for quantitative 3-D volume construction.

The first step is to quantify the PS* concentration on the surface by performing a curve fit of the XPS C 1s spectra (large area) taken from an area analyzed by imaging XPS, Confocal and AFM. Survey spectra of the analyzed areas

are shown in Figure 56 (a). The Cu 2p peak in the spectra is due to the copper grid that is in the field of view of the area analyzed. The C 1s envelope has been curve fit with components from PS* and PMMA shown in Figure 56 (b) and (c). In addition, there appears to be two oxygen contamination peaks in both of the spectra. The percent PS* calculated for the two curve fits are 17% and 28%, respectively. These values correspond to the maximum and minimum PS* concentrations from this area, respectively. Assuming that the gradient behaves similarly through the bulk of the sample, we would expect a minimum and maximum value of 70% and 90% for PS*, respectively, for the bottom of the sample. These values are the extrapolated values calculated with respect to the quantified regions from the first slice. The blend was too thin to be removed from the silicon substrate for analysis, thus preventing quantification from the bottom of the blend. Since these values are used for visualization purposes only, this assumption will suffice. For complete quantification it would be ideal to know concentrations from the top and bottom of the sample by XPS. In addition, a method must be devised to obtain quantitative information from different slices throughout the sample, perhaps by microtoming the sample into thin slices for XPS analysis.

Figure 57 (a) is a plot of grayscale values (0-255) for the minimum and maximum intensities obtained from each of the top 25 slices from the confocal image stack. The intensities must then be converted to concentrations using the quantitative information from XPS; the minimum and maximum values for the first slice are set to

17% and 28% PS*, respectively. The intensities in the remaining confocal slices are mapped by taking a weighted average between the maximum and minimum values obtained from the bottom and top of the sample. A plot of the quantified confocal data, % PS* versus confocal slice number is shown in Figure 57 (b). The quantified confocal data is then assembled into a volume using MATLAB,⁶⁶ shown in Figure 58 (a). The AFM topography image can be assembled into a volume, representing the topography of the PS*/PMMA. The volume created in MATLAB is shown in Figure 58 (b). Since the two images were registered in the previous section, the AFM volume, created in MATLAB, can be assembled on top of the confocal volume to create a real representation of the PS*/PMMA blend. Figure 59 (a) shows the assembled volume created in MATLAB. From the cross-sectional image in Figure 59 (b), the fluorescein labeled polystyrene can be followed through out the sample. It appears to be enriched near the surface; however, in the bulk, the fluorescence intensity decreases as it is interspersed with PMMA.

Conclusions

This work has demonstrated the ability to obtain data from the same area on the same sample using XPS, AFM and confocal microscopy. Once images were obtained using the different techniques, an automatic image registration program, mutual information, was used to register the images from the different techniques. The automatic registration method is more robust than manual image registration, taking pixel intensities into consideration. This method was used to register XPS,

AFM and confocal images obtained from the same areas from 50:50 blends of PS* and PB, and 50:50 blends of PS* and PMMA.

In addition, this work has demonstrated for the first time the use of valence band imaging with XPS. It allows images of a particular phase to be obtained from the valence band region when core-level spectra cannot be used, due to overlap in the spectra between the different blend constituents. Also, by creating a multivariate data set, a collection of images at various binding energies, feature extraction by principal component analysis was widely used to obtain images representative of a single polymer phase. This was demonstrated for a collection of valence band images of the 50:50 blend of PS* / PB in which a PS* phase images was obtained from the 3rd principal component image. In addition, a PS*-enriched principal component image was obtained for the 50:50 blend of PS* / PMMA

Quantification of confocal images by XPS has been introduced as a method to obtain quantitative information from confocal slices. However, in this work it was only semi-quantitative due to the lack of data from the bottom and center of the sample. As discussed earlier, a sample should be able to be removed from the substrate for analysis of the bottom. In addition, a method should be devised to obtain quantitative XPS data from different slices through the sample for proper quantitative confocal images.

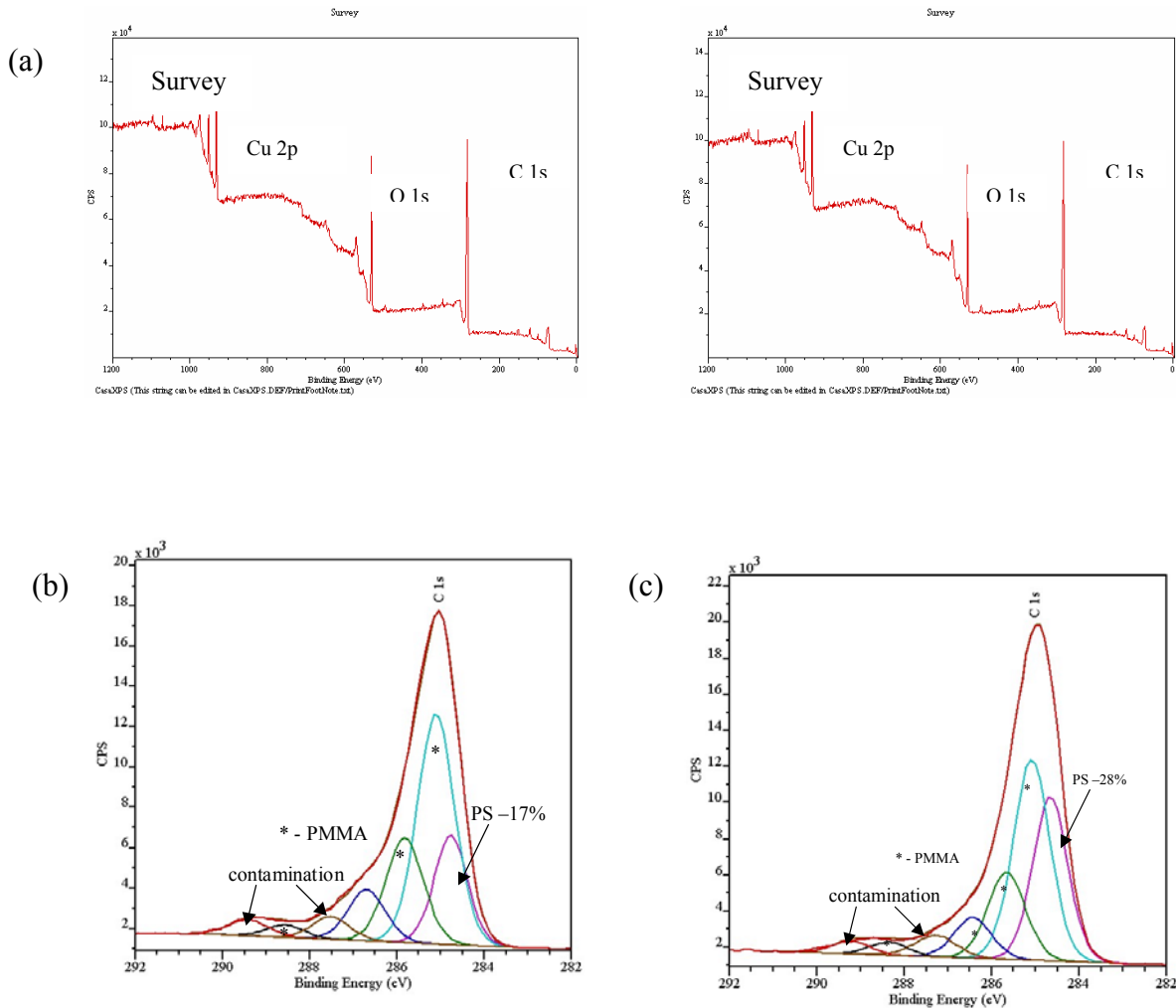


Figure 56. Survey spectra from two of the analyzed areas on the PS*/PMMA sample (b) C 1s envelope fit with PS* and PMMA components. There also appears to be peaks due to contamination. The percent PS* determined from the curve fit is 17%. C 1s envelope fit with PS* and PMMA components, along with two contaminant peaks. The percent PS* determined from the curve fit is 28%.

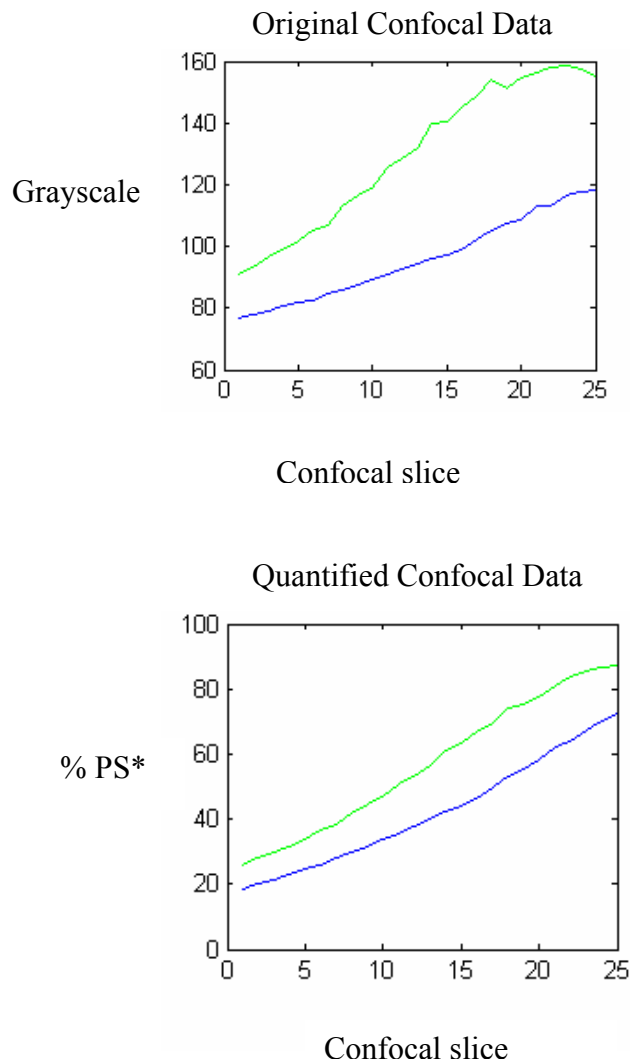


Figure 57. (a) Grayscale values (0-255) versus confocal slice for the minimum and maximum values obtained for each slice. (b) A plot of the quantified confocal data, % PS* versus confocal slice.

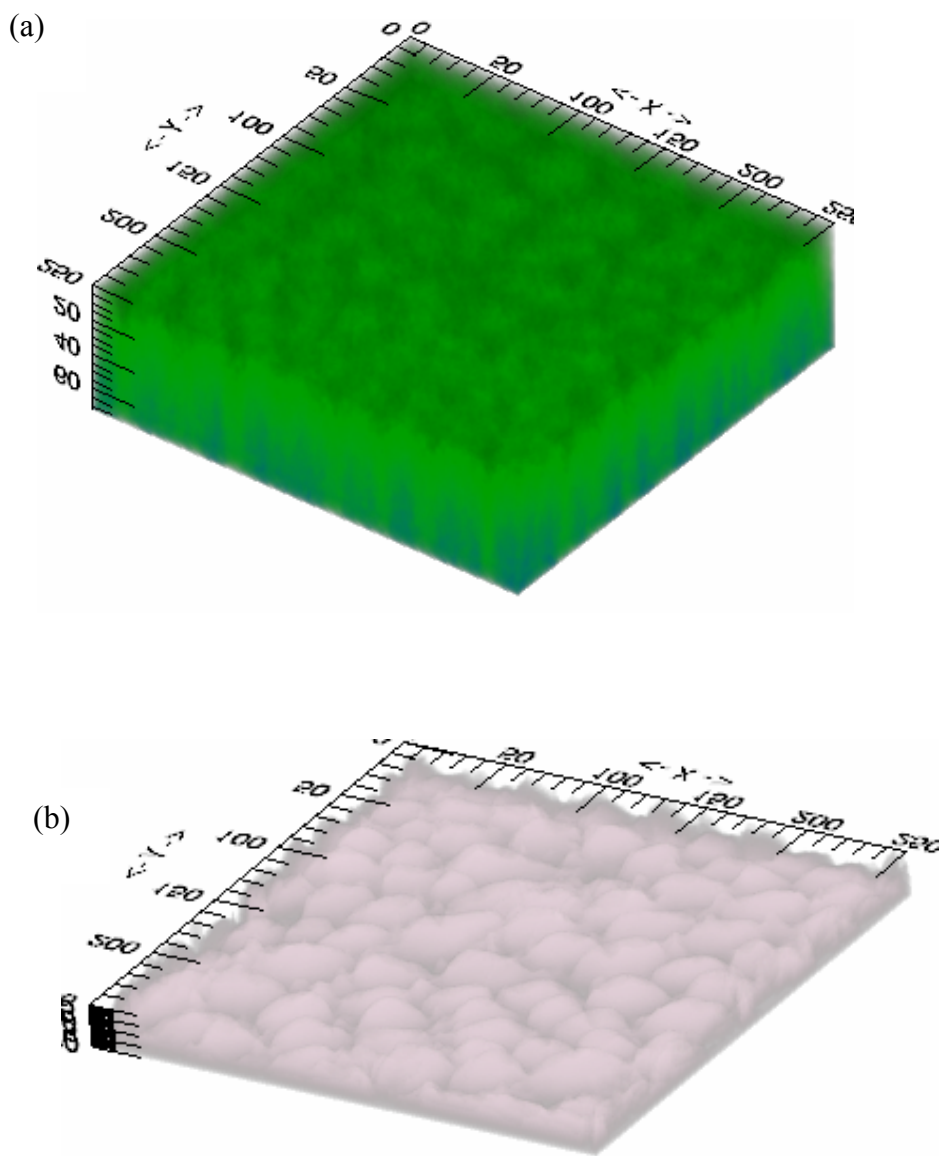


Figure 58. (a) Quantified confocal volume ($40 \times 40 \mu\text{m}^2$) (b)
AFM topography image assembled into a volume ($40 \times 40 \mu\text{m}^2$).

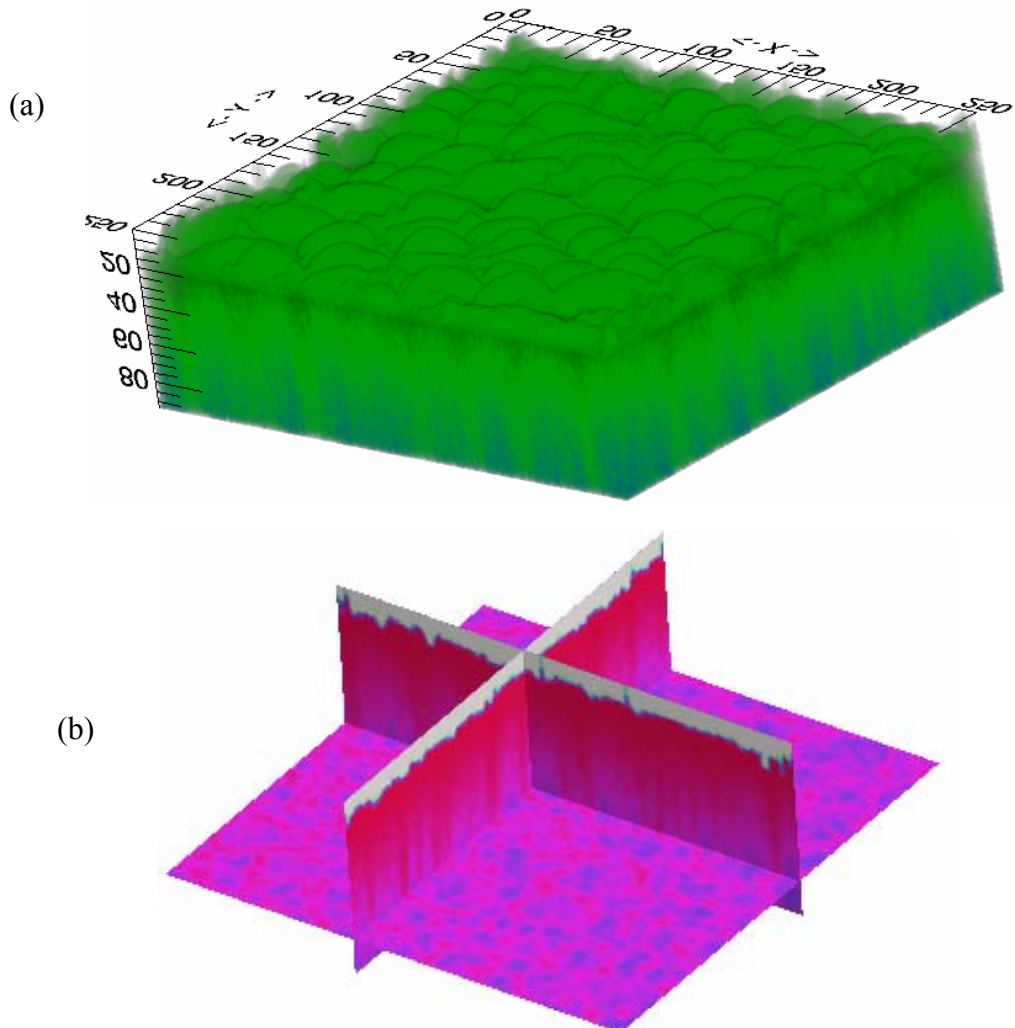


Figure 59 (a) The AFM volume is assembled on top of the confocal volume to create a real representation of the PS*/PMMA blend ($40 \times 40 \mu\text{m}^2$). (b) A cross-sectional representation of the assembled volume.

CHAPTER 6

PRELIMINARY EVALUATION OF FLUORESCENT POLYMER BEADS FOR IMAGE REGISTRATION AND 3-D FEATURE CORRELATION

Introduction

A single fluorescent bead can serve several purposes when doing multitechnique correlation with imaging XPS, AFM, and confocal microscopy. The bead can serve as a different approach to image registration. In Chapters 4 and 5, image registration was accomplished by manual image registration, marking an analysis area with an AFM tip, and the use of mutual information. By depositing beads on a surface that can be imaged by XPS, AFM and confocal microscopy, same area analysis and image registration can be made easier. The bead can also serve as a calibration tool. Intensity calibration kits, composed of microspheres with known relative intensities, can be purchased and used as a possible method for confocal image quantification and can serve as a spatial resolution marker. In addition, blurring in confocal images can be evaluated using a single bead. This blurring can be corrected using deconvolution software, and the correction can be applied to the 3-D confocal volume. This chapter presents a preliminary evaluation of the utility of fluorescent polymer beads in the development of image correlation methods.

When trying to obtain data from a single fluorescent bead using XPS, AFM and confocal microscopy, several issues had to be addressed. The first consideration was how to prepare the beads to obtain data from a single bead. The beads were prepared in a solution so that they could be deposited on a surface. Since the beads had a tendency to cluster together on the surface after deposition, the bead solution had to be sufficiently diluted to circumvent this problem. Additionally, to analyze a single bead by AFM, the bead had to be no taller than 6 μm , the z-range of piezo in AFM. Since the bead was 9 μm in diameter, we took the approach of spin coating polymer around the bead to embed it in polymer so that no more than 5 μm of the bead protruded from the polymer surface. Consideration was also given for the best choice of polymer. The polymer had to be chemically different from the polystyrene bead so that imaging XPS could be done. In addition, the solvent the polymer was dissolved in should not remove the fluorescent dye from the sample; many organic solvents do remove the dye. After the proper polymer was chosen, it had to be spin coated onto the sample. The thickness of the layers depended on the concentration of the polymer used and the spin rate.

One of the problems with confocal images is the image degradation that occurs during image acquisition. This image degradation is brought about by four independent phenomena: noise, scatter, glare and blur.⁴⁹ Blur, however, can have the greatest affect on image quality and has become the impetus for a host of newly developed image deconvolution software programs for confocal microscopy. Blur is due the nonrandom spreading of light from out of focus light emitted by objects situated above and below the confocal plane. Blurring causes the observed features to have a reduced sharpness and

limits the spatial detail of the object in the collected image.⁴⁹ This becomes a problem when comparing images from the same area using multiple techniques.

A theoretical optics based model for blur that has evolved is the point spread function (PSF). It is based upon an infinitely small point source of light originating from the sample. Since the confocal microscope only collects a fraction of the light emitted by this single point, it cannot be focused into a perfect three-dimensional image of the point. Therefore, the point spreads into a three-dimensional diffraction pattern, causing the observed features in the image to be widened. Light that is emitted from each point in the object is convolved with a point spread function to produce a final image. The brightness of every point in the image is linearly related by the convolution operation to the fluorescence intensity of each point in the sample.⁴⁹ Since the point spread function is three-dimensional, blurring from the point spread function is an inherently three-dimensional phenomenon.⁴⁹ Confocal microscopy images from a fluorescent bead provide qualitative information about blurring in the confocal microscope used in this research, as well as a data set that can be used to test software designed to correct for blurring.

The goal of this work was to develop a method to obtain data from a single 9 μm microsphere using XPS, AFM and confocal microscopy. Once a method was developed, the dimensions of the features were measured and compared with each other and the manufacturers value. In addition, the feasibility of using the microspheres as an image registration method was investigated.

Experimental

XPS spectra and images were acquired on a Kratos AXIS Ultra photoelectron spectrometer using a monochromatic Al K α source operating at 300 W. The base pressure was 2×10^{-10} Torr and the operating pressure was 2×10^{-9} Torr. Charge compensation was accomplished using low-energy electrons. Standard operating conditions for good charge compensation are -2.8 V bias voltage, -1.0 V filament voltage and a filament current of 2.1 A.

Tapping mode AFM was performed with Digital Instruments Dimension 3100 AFM or a Park Scientific scanning probe microscope. Topographic images were collected at ambient conditions. Commercial Si₃N₄ cantilevers with force constants of 2.5-8.5 N/m, and resonance frequencies between 120-190 kHz were used.

Confocal images were obtained with a BioRad MRC-600 confocal laser-scanning microscope using an argon-ion laser with an excitation wavelength of 488nm in the single channel mode (T1/T2A filter cubes, BioRad, Hercules, CA). The emission wavelength was 518 nm for the fluorescein labeled polystyrene. Confocal microscopy images were collected with the BioRad Cosmos software.⁸⁶

Fluorescein labeled polystyrene beads were purchased from Duke Scientific. The beads have a nominal diameter of 9 μm with a 13% coefficient of variation, according to the specifications of the manufacturer.

Bead Preparation

To be able to image an individual bead using imaging XPS, AFM and confocal microscopy the beads should be dispersed when deposited on a surface. Initially, the beads were prepared in a 1% w/v solution in tetrahydrofuran (THF). A couple of drops were then deposited on a silicon substrate with a glass pipette and allowed to dry under ambient conditions. Under an optical microscope, the beads appeared clumped on the surface, and few individual beads were visible. In addition, analysis of the beads by confocal microscopy revealed the dye was removed from some of the beads by the solvent, THF.

The beads were then prepared in a 0.01% w/v aqueous (distilled water) solution. The solution was sonicated for 10 minutes to disperse the beads in the solution. A few drops of the beads were deposited on a silicon substrate and allowed to dry. Under the optical camera, the beads appeared somewhat dispersed, and individual beads were located easily. Some of the beads were packed together, but these clusters can serve as markers for locating individual beads for XPS, AFM and confocal analysis. This preparation method was used for all samples discussed in this chapter.

Previous Sample Preparation Trials

Poly (methyl methacrylate) (PMMA, MW = 75 kDA) was used in initial trials. A 0.2 % w/v solution of PMMA in tetrahydrofuran was prepared and spin coated onto the sample. The C 1s spectrum of the two polymers is shown in Figure 60 (a) and (b). This

particular polymer was unsuccessful for imaging XPS because there was overlap between the C 1s peaks for both of the polymers, thus preventing imaging of a single bead.

Polypropylene (PP, MW = 12 kDa) purchased from Sigma-Aldrich was dissolved in boiling o-Xylene to make a 1% w/v solution. After cooling, the solution was placed in a 5cc syringe and filtered through a .45 μm pore size Acrodisk filter to remove any undissolved polymer. 10 drops of the polymer were then spin coated on the beads at 800 rpm. The sample was first analyzed by XPS. The C 1s peak for PP appears at 285.0 eV, while the C 1s peak for polystyrene appears at 284.8, shown in Figure 61 (a) and (b). An image taken at 284.8 eV did not show any beads on the surface. An O 1s spectrum was acquired for both polymers, shown in Figure 61 (c) and (d). It appeared that the surface of polypropylene was oxidized. An O 1s image taken at 529.4 eV showed the absence of intensity due to the presence of the beads, shown in Figure 62 (b). However, when analyzed by AFM, the beads dislodged from the polymer easily, preventing imaging.

Polyethylene glycol (PEG, MW = 20 kDa) was tried because the C 1s peak appeared at 286.4 eV, which is a couple of electron volts away from the polystyrene peak at 284.8 eV. A solution of 0.2% ethylene dissolved in chloroform was prepared, and 30 drops of polyethylene glycol was spin coated on the sample at 800 rpm. In addition, PEG formed a reflective coating on the silicon substrate, resulting in an intense reflection while acquiring confocal images. In some cases, the reflection intensity was greater than the fluorescence signal, causing the contrast to be reversed in the images, as shown in Figure 63.

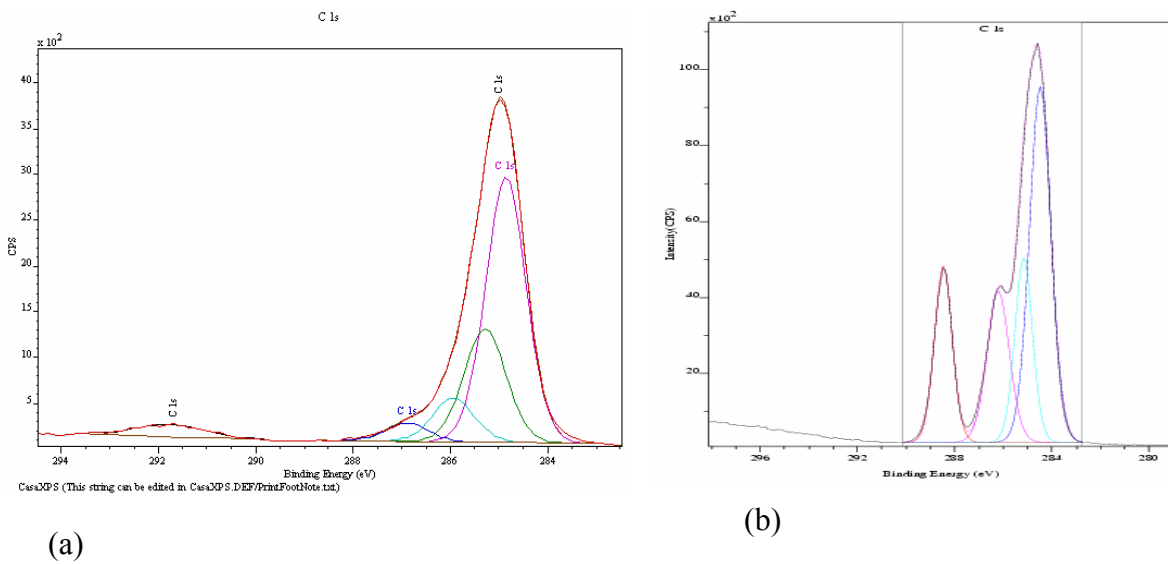


Figure 60. (a) C 1s spectrum of fluorescein labeled polystyrene microspheres. (b) C 1s pectrum of PMMA.

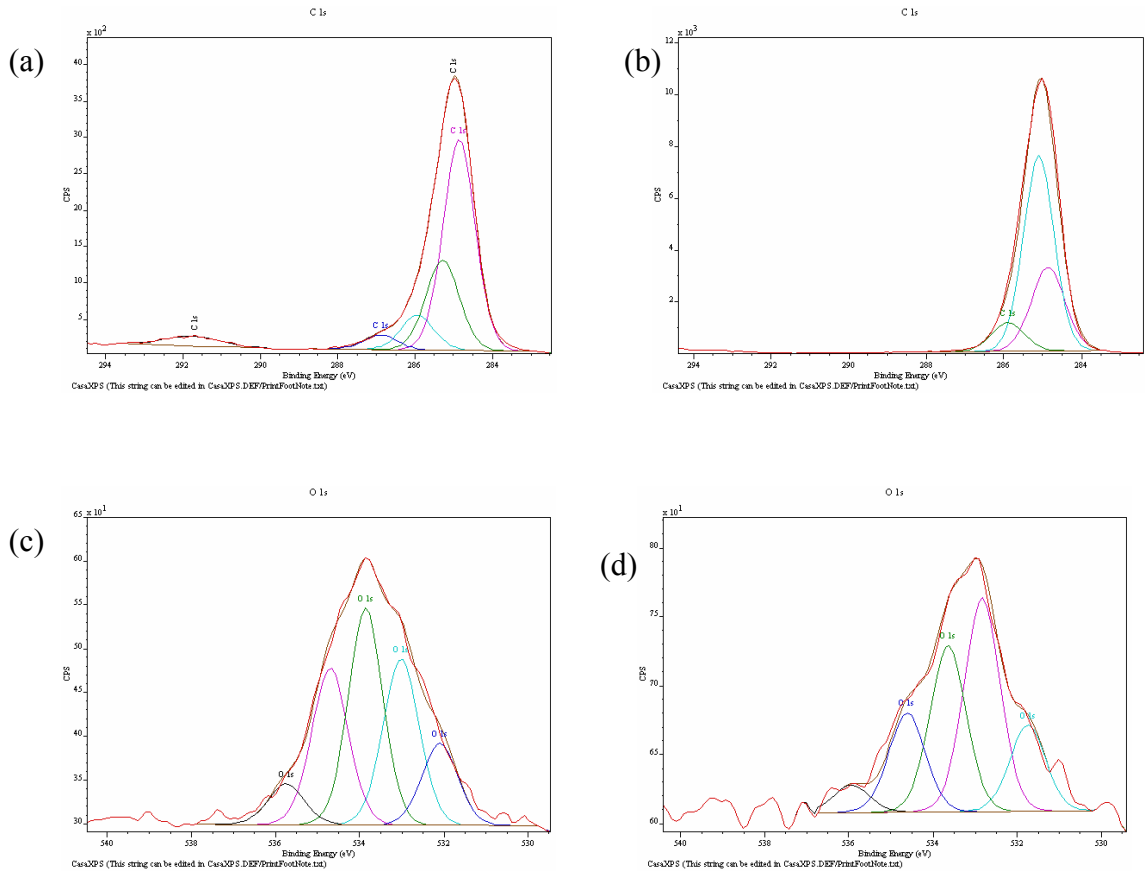


Figure 61. (a) C 1s spectrum of fluorescein labeled polystyrene. (b) C 1s spectrum of polypropylene. (c) O 1s spectrum of fluorescein labeled polystyrene. (d) O 1s spectrum due to the surface oxidation of polypropylene.

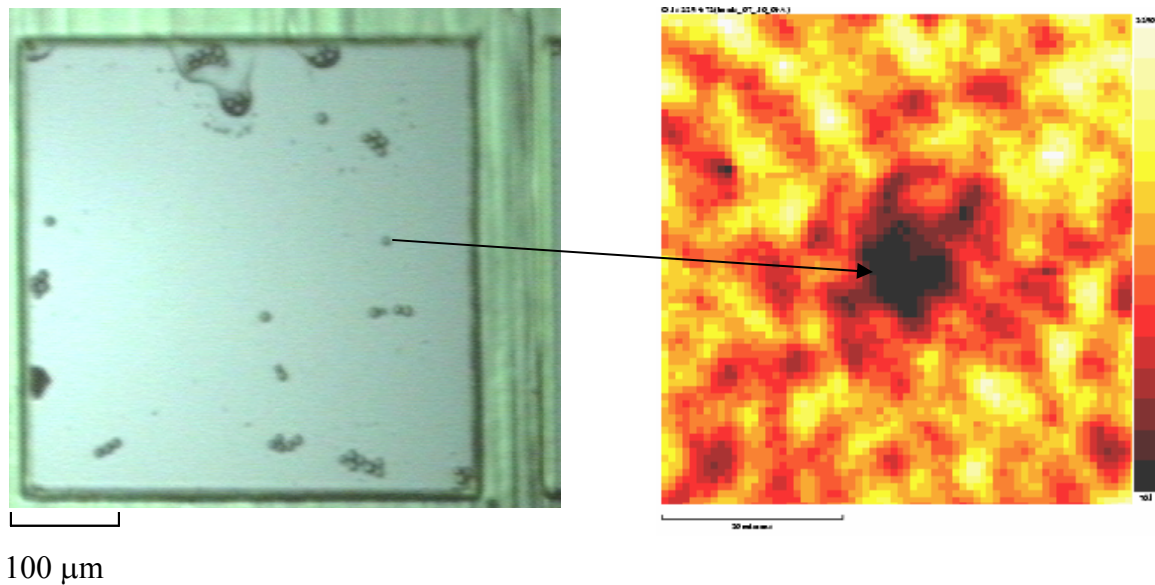


Figure 62. (a) An optical image of beads embedded in polypropylene. (b) An O 1s XPS image of a single bead taken at 529.4 eV. The arrow shows which bead was imaged with XPS.

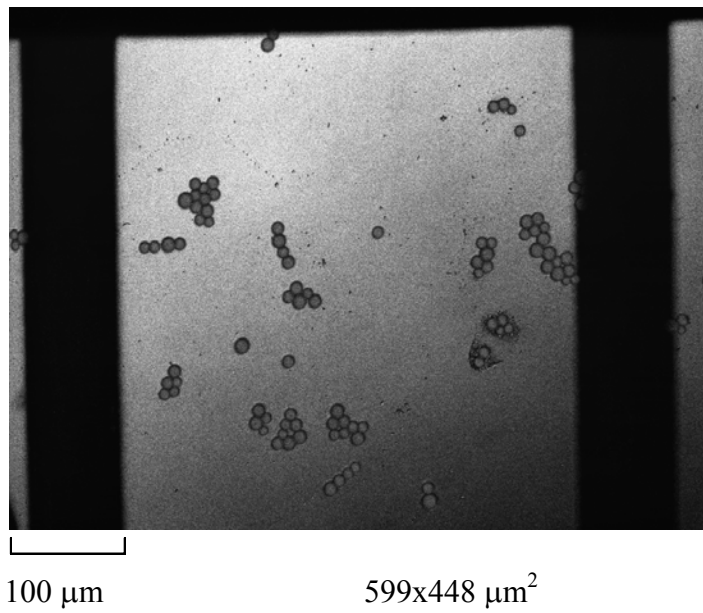


Figure 63. Confocal image of polystyrene beads on a surface embedded Polyethylene glycol (PEG). The reflective surface reverses the contrast in the image; the beads appear dark and the polymer appears brighter.

It would be ideal to use a polymer that forms an opaque coating on the surface to minimize the reflection from the silicon substrate. Additionally, during imaging with tapping mode AFM, the beads were easily dislodged.

An attempt was made using Polyimide 2555, since it is a polymer that can be cured. The idea was that the curing process would prevent the single bead from becoming dislodged when imaging by AFM. 110 drops of Polyimide 2555 were spin coated on the sample at 1500 rpm. Imaging of the sample was successful by AFM, but when the sample was analyzed by confocal microscopy, it appeared as if the dye had been removed from some of the beads. Removal of the dye may be a result of the solvent the polymer is dissolved in or the curing process (heating on a hotplate for 60s at 90°C). Each may have detrimental effects on the dye. In addition, Polyimide 2555 formed a reflective coating on the silicon substrate, resulting in an inversion in image contrast, as described in the previous paragraph. Because of this, confocal images were not acquired.

45 drops of polytetrafluoroethylene-30 (PTFE-30), dissolved in a surfactant (Triton and water mixture), was spin coated onto the sample at 1500 rpm for 45s. PTFE was chosen because the C 1s peak from PTFE appeared at 292.5 eV, while the C 1s peak for the bead appeared at 284.8 eV for XPS; the C 1s peak for polystyrene should be far enough away from the PTFE peak to image individual beads. Confocal microscopy images were collected with the BioRad CoMOS software⁸⁶. The 154x123 μm confocal image was obtained using a 60x objective and a 2x zoom. A total of 111

slices were collected at 0.7 μm increments through the sample. Every tenth slice is shown in Figure 64. The next step is to image an individual bead using imaging XPS.

Image Analysis

An O 1s image was obtained of a single bead, shown previously in Figure 62 (b). The polymer used was polypropylene. The image of the bead is a result of the absence of intensity at 529.4 eV. The bead appeared somewhat round in the XPS image. This may be due to noise in the image or polypropylene may have built-up around the bead, preventing it from appearing completely round, as it appears in the optical image in Figure 62 (a). The measured width of the single bead was determined from a line scan shown in Figure 65. The measured diameter of the bead was 8.5 μm . This value was close the manufacturers quoted value of 9 μm . One additional problem that became apparent in the course of this investigation was the range of bead sizes, which made imaging by AFM difficult at times. The manufacturer reported a 13% coefficient of variation in bead size; however, by visual inspection, some of the beads appear larger and smaller than the manufacturers reported variation.

Confocal microscopy images were collected from an individual bead embedded in PTFE-30, described in the sample trials section, with the BioRad CoMOS software.⁸⁶ 154x123 μm^2 confocal images were obtained using a 60x objective and a 2x zoom. A total of 111 slices were collected at 0.7 μm increments

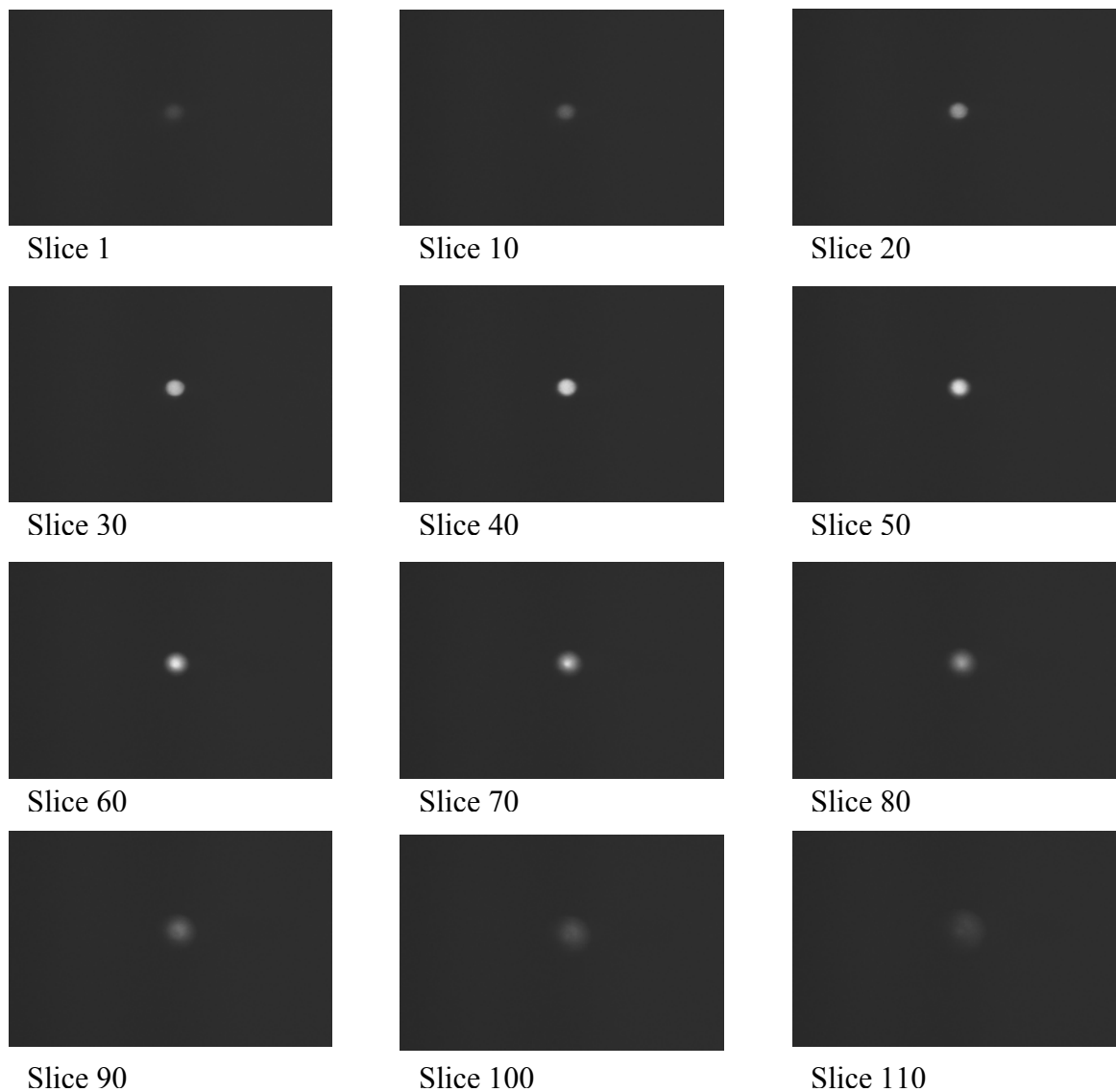


Figure 64. Representative confocal slices ($154 \times 123 \mu\text{m}^2$) from a $9\mu\text{m}$ microsphere embedded in PTFE-30.

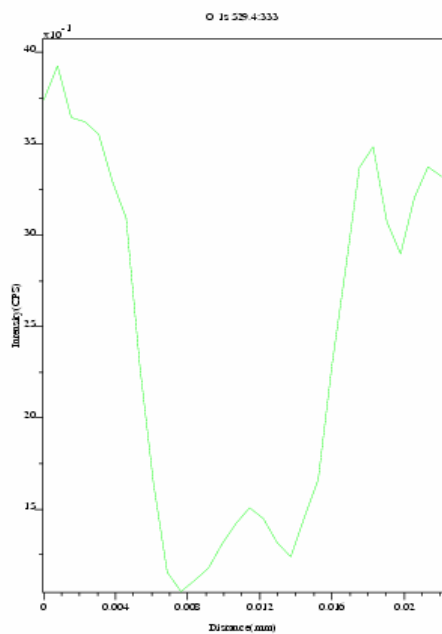
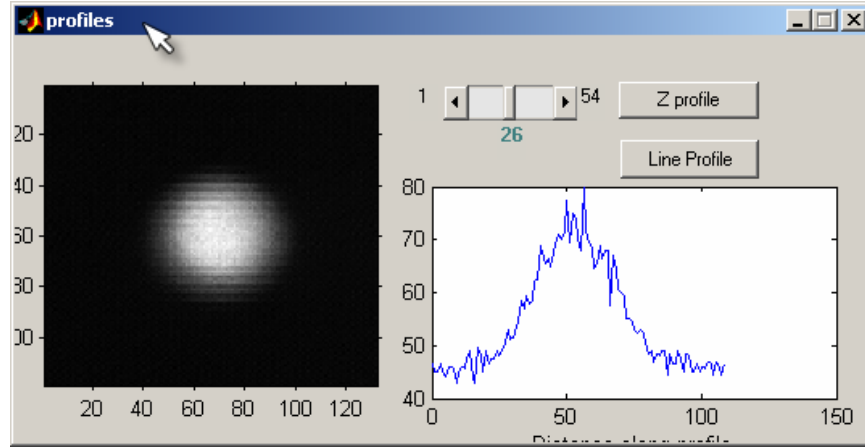


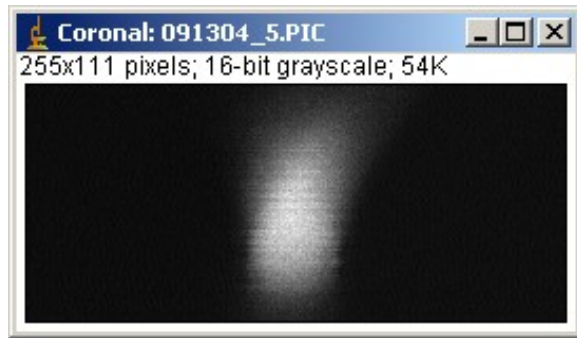
Figure 65. An XPS line-scan of the single polymer microsphere, shown in Figure 62 (a). The measured width of the bead is 8.5 μm .

through the sample. A cross sectional evaluation of one of the slices showed that the diameter of the bead to be $\sim 9 \mu\text{m}$, shown in Figure 66 (a). This agreed well with the manufacturers quoted value of $9 \mu\text{m}$. The images demonstrate that the entire bead volume was acquired. An image of the confocal volume was created in MATLAB⁶⁶, shown in Figure 66 (b). The image appeared diffuse and lacked the features of a round bead, as a result of the blur that is associated with confocal images. Blurring causes the observed features to have a reduced sharpness and limits the spatial detail of the object in the collected image. A deconvolution software program can be useful to help resolve this problem, and this data set will be used to evaluate programs as they become available.

An AFM topography image was acquired from the individual bead embedded in PTFE-30, described in the sample trials section. In order to properly image the bead, the tip was raised so that it just touched the surface. In addition, a slow scan rate of 0.1 Hz was used so that the feedback loop had time to adjust to the sudden height changes on the surface, otherwise scanning artifacts would be introduced into the image. A topographical image of the bead is shown in Figure 67 (a). The image was not plane-fitted, so that artifacts due to large surface features are not introduced into the image. One example of an artifact is shown in Figure 67 (b). The image was obtained using a 0th order plane fit. Dark features appear to the left and right of bead, due to the plane-fitting procedure. The artifact becomes more pronounced as the order of the plane-fit increases. A cross-sectional evaluation of the bead showed that it was $\sim 10.5 \mu\text{m}$ wide and had a height of $5.25 \mu\text{m}$, shown in Figure 68 (b). By optical inspection, the bead did not appear



(a)



(b)

Figure 66. (a) A cross-sectional image of a single polymer microsphere embedding in PTFE-30. The measured diameter of the bead is $\sim 9 \mu\text{m}$, which agrees reasonably well with the manufacturer's quoted value of $9 \mu\text{m}$. (b) An image of the total confocal volume of the bead. The image appears blurred, and lacks the features of a microsphere.

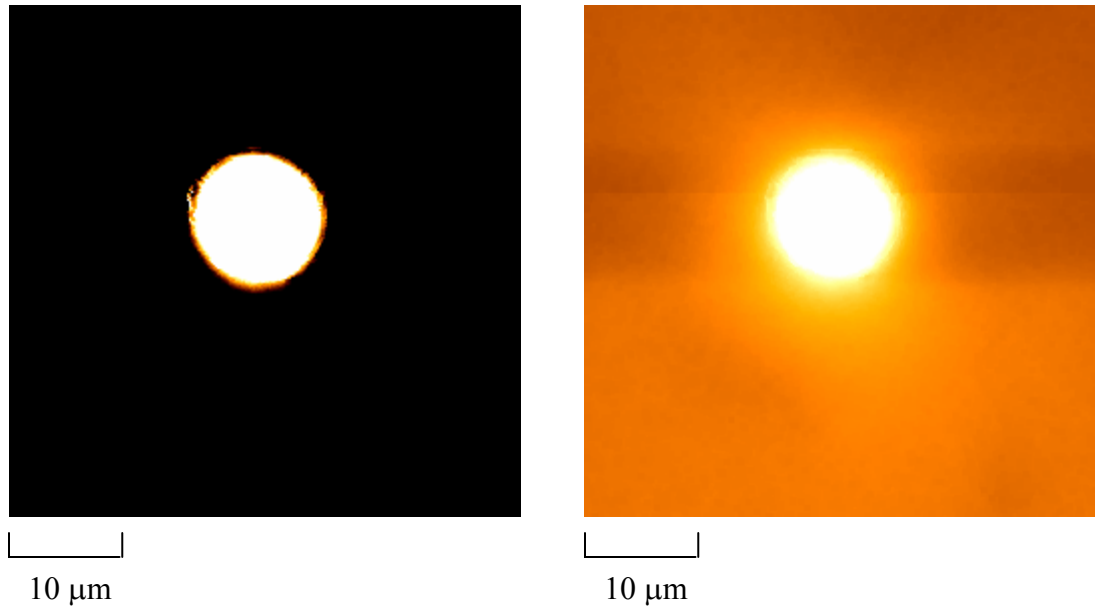


Figure 67. (a) A $45 \times 45 \mu\text{m}^2$ image of a single polymer microsphere embedding in PTFE-30. (b) Image 8(a) fit with a 0^{th} order plane-fit. The dark areas to the left and right of the bead are artifacts of the plane-fit. These artifacts become more pronounced as the plane-fit order is increased.

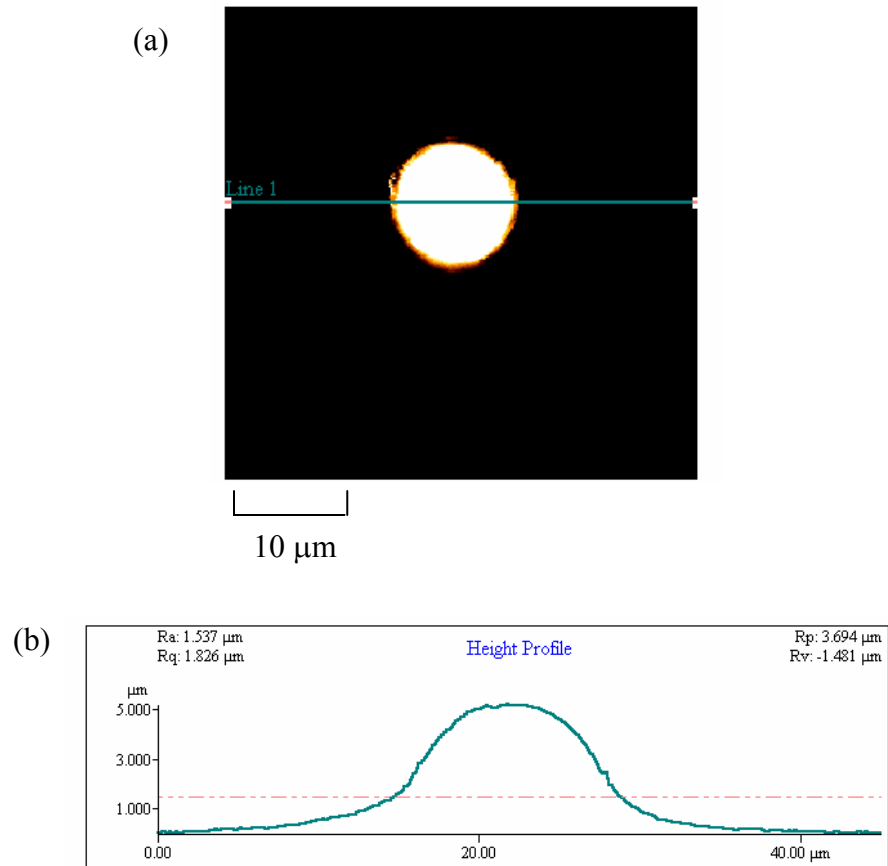


Figure 68. (a) An AFM image polymer microsphere embedded in PTFE-30, showing where the cross-sectional measurement are taken. (b) A cross-sectional image of a single polymer microsphere. The measured diameter of the bead is 10.5 μm , and the maximum height is 5.25 μm

to be covered by the polymer, but it was difficult to establish and this will need to be confirmed by imaging XPS. One possible explanation for the greater diameter measured with AFM, compared with the confocal image was that there appeared to be polymer build-up around the bead in Figure 68 (b), due to the spin-coating process. Therefore, it was difficult to get an exact measurement of the bead diameter using the AFM cross-sectional image. One advantage of the confocal microscope was that polymer build-up around the bead did not interfere with the imaging; since PTFE does not fluoresce. Therefore, only the bead is observed. This will lead to a better estimate of the bead diameter.

The Utility of Fluorescent Microspheres

The fluorescent microspheres can serve as features in an image for image registration purposes. If the beads are in the field of view for images obtained by XPS, AFM and confocal microscopy, area location and image registration can be made easier. To check the feasibility of this, two images were resolution matched in terms of micron/pixel, as discussed in Chapter 5, and registered in MATLAB,⁶⁶ using the mutual information algorithm discussed in Chapter 3. The registered images are shown in Figure 69. This registration method does not require the sample to be damaged, unlike AFM lithography, and the beads can serve as a means of calibration for the confocal microscope, as discussed in the following paragraphs.

Microscopy image intensity calibration kits can be purchased from commercial vendors. The kit comes with 6 μm microspheres that are coated to have nominal relative

fluorescence intensities. The microspheres can be used for intensity calibrations and calculating point spread functions. In addition, focal check fluorescent microspheres with diameters of 6 μm can be used for examining the alignment, stability of the laser, and confirming the optical sectioning thickness (Z-resolution) in three-dimensional imaging applications.⁹⁰ These microspheres have a well-defined dye layer that, when viewed in cross section in the confocal laser-scanning microscope, appears as a fluorescent ring of varying dimensions depending on the focal plane. This will aid in determining the focus depth into the sample.

Conclusions

A single 9 μm sphere can be imaged using XPS, AFM and confocal microscopy. The beads must be prepared in an aqueous solution dilute enough to provide dispersion of the beads on a surface. The appropriate concentration used in this research was a 0.01% w/v aqueous (distilled water) solution. A polymer that does not remove the fluorescent dye, appears opaque on the surface, is thin enough to coat the sample without covering the bead, and is chemically different from the bead should be used. This method clearly has more limitations than were apparent at the start of the experiment. PTFE-30 has proven successful for AFM and confocal microscopy imaging. In the future, XPS will be used to image a single bead. It is hoped that the chemical differences between PTFE-30 and the bead will allow an image of a single bead to be obtained.

From the image comparison data from the three techniques, it appears that XPS and confocal sectional images give a reasonable estimate of the bead diameter. However,

the AFM cross sectional analysis gives a larger estimation of the bead diameter. One explanation is that there is polymer build-up around the bead, making the diameter wider than it should. In addition, further work, possibly by imaging XPS, has to be done to ensure that the polymer does not cover the bead. When the confocal volume is displayed, it appears diffuse and the features don't resemble a sphere, as expected, as a result of blur of the confocal image. Calculation of the point-spread function and the use of deconvolution software may remove some of these artifacts. This will have to be investigated in the future.

In the future, the polymer microspheres may serve as an additional registration method for images obtained by imaging XPS, AFM, and confocal microscopy. The bead patterns can be located and imaged by all three techniques. Beads can be purchased and embedded in the sample for calibration purposes, in addition to image registration. Polymer microsphere kits can be obtained for intensity calibrations and calculating point-spread functions. In addition, focal check fluorescent microspheres with diameters of 6 μm can be used for examining the alignment, stability of the laser, and confirming the optical sectioning thickness (Z-resolution) in three-dimensional imaging applications. This is important for knowing the depth of focus.

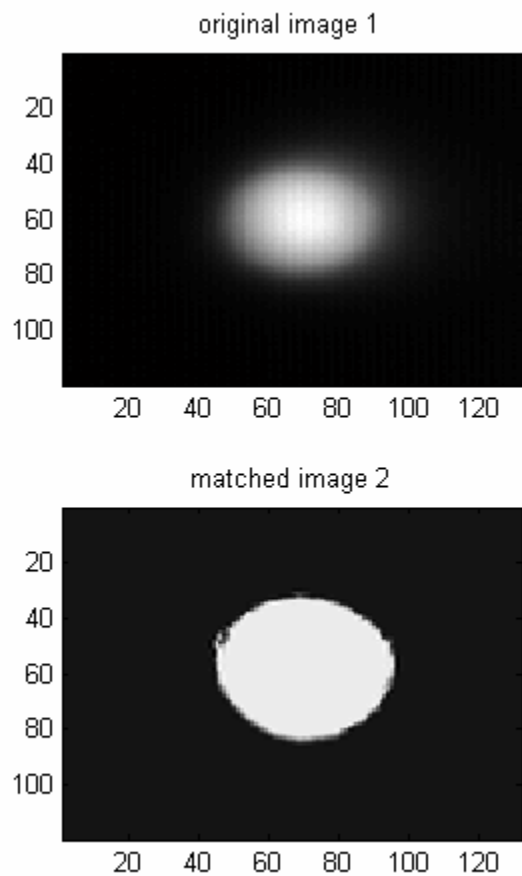


Figure 69. The confocal and AFM registered images from the same polymer microsphere embedded in PTFE-30. The images were registered using the mutual information algorithm.

CHAPTER 7

SUMMARY AND FUTURE WORK

Correlation of AFM and XPS Imaging for Qualitative and Quantitative Phase Identification in Polymer Blends

This work demonstrated that imaging XPS could be used to chemically identify different phases observed in phase-contrast AFM images. The first step was to outline a method for AFM/XPS correlation using a sample of known properties. A patterned sample of polymer on ITO prepared by photolithography was used. The sample was composed of alternating lines (~6 μm wide) of polymer and ITO. AFM topography and phase images were acquired from the patterned sample. XPS In 3d images were acquired of the same sample.

To correlate the images the field of view, resolution and image alignment were taken into consideration. Since the field of view for AFM overlaps with that of XPS, the field of view for the two techniques were matched by cropping an area from the XPS image that had the same dimensions as the AFM image.

Resolution from the two techniques had to be matched. This was accomplished by using a median convolution filter. In the first step, the mathematical resolution had to be

matched in terms of $\mu\text{m}/\text{pixel}$, and in the second step the technique resolution were matched. Kernel sizes were determined for each step and used in the convolution filter.

Quantification of the images was achieved through the use of K-means unsupervised classification. This assigned color-coated labels to pixels that belong to a particular phase, ITO or polymer. After classification, post classification statistics was used to calculate the percent surface coverage for each phase detected by AFM and imaging XPS. The results were compared for images of the patterned polymer sample at different sizes. There was a reasonable agreement for the results between the two techniques.

This correlation method was extended to blends of PMMA/PVC prepared at three different compositions (25/75, 50/50, 75/25). AFM and XPS images were acquired of the blends. For a qualitative comparison between the two techniques, the field of view were matched for images from a 75/25 blend obtained from XPS and AFM. The AFM image was deresolved, and similar size and shape features were observed for the two images. This means that similar phases are being accessed.

Image classification was applied to AFM and XPS images acquired from the PMMA/PVC blend for the three different blend compositions. The surface coverage for PMMA was obtained from the post classification statistics results for all the images. A plot of the PMMA-enriched surface coverage for the PMMA/PVC blends detected by AFM versus the PMMA-enriched surface coverage detected by XPS demonstrates that the two techniques correlate reasonably well. For the 25/75 and 50/50 blend compositions, surface segregation of PMMA is confirmed by both methods. For the

75/25 blend, PVC segregation, relative to the bulk composition, was observed by both experiments.

The problem of image alignment was addressed by using AFM lithography to mark an area on a sample. In this research, the AFM tip was used to draw a $130 \times 130 \mu\text{m}^2$ box on a patterned polymer sample. Once drawn, a $100 \times 100 \mu\text{m}^2$ AFM topography and phase image was acquired from inside the box. Additionally, the box was located with imaging XPS, and an In 3d image was acquired. The box could be clearly seen within the XPS image. The analysis area was cropped from the XPS image and converted to an In 3d intensity profile image, and the AFM image was converted into a 3-D topography image. The AFM topography image and the XPS In 3d photoelectron intensity profile image were aligned by manual rotation so that corresponding features overlapped. This not only allows for phase identification, but also makes it possible for 3-D characterization by combining the topographical data from AFM and the chemical information from XPS.

In addition, the effect of kernel size on classification results was studied. The classification results obtained for AFM topography and phase images of the patterned sample show that results did not vary much for the three kernel sizes used (9,11,13). The deresolution process caused the patterns to be altered proportionately, thus conserving the results obtained for different kernel sizes used. In the case of the polymer blends, the results are dependent upon the features observed in the images; features may coalesce, altering the classification results.

The fractal dimension of the three different blends (25/75, 50/50 and 75/25 PMMA/PVC) was calculated to provide information about the self-similarity and disorder of the surface. Using the box-counting method, the fractal dimensions were determined for AFM topography images at the 1 μm , 5 μm , and 10 μm level. The fractal dimension at the 1 μm level were similar for all the blend combinations. At the 5 μm level the fractal dimension reached a maximum for the 75/25 blend. From the fractal dimensions calculated, it appeared that the PMMA/PVC blends form a highly disordered (fractal) surface.

In the future, this correlation method will be applied to the multitechnique correlation work, using AFM, XPS and confocal microscopy. This procedure can readily be extended to other heterogeneous samples.

Image Fusion of Polymer Blends using AFM, Confocal Microscopy and Imaging XPS

In Chapter 5 two blends were analyzed, PS*/PB and PS*/PMMA. For the PS*/PB blend an analysis area was marked with the AFM tip by drawing two parallel lines \sim 80 μm long and \sim 120 μm apart. Inside this area a 60 μm AFM image was acquired at a known distance inside the marked area. With the marked area in the field of view, a z-series of confocal images was acquired from this area. The sample area was then analyzed by imaging XPS. Since it was not possible to distinguish between the blend phases using the core peaks, the valence band was used. Images were acquired at different binding energies in the valence band. This created a multivariate data set in

which PCA was applied to extract a PS* phase. The three images were registered using the mutual information algorithm.

For the PS*/PMMA blend an analysis area was marked with the AFM tip by drawing two parallel lines ~80 μm long and ~120 μm apart. Inside this area a 40 μm AFM image was acquired at a known distance inside the marked area. With the marked area in the field of view, a z-series of confocal images was acquired from this area. A series of C 1s images was also acquired with the lines in the field of view. PCA was used to extract a PS* image from the C 1s data set. The images were registered using the mutual information algorithm to provide images from the same area on the same sample.

The above data set was used for quantitative confocal imaging, in which pixel intensity in a confocal image was assigned a concentration, according to XPS analysis from the same area. This created a quantitative confocal volume. The AFM topography volume was assembled on top of the confocal volume to create a real representation of the PS*/PMMA blend.

In the future, resolution-merging algorithms will be applied to AFM and XPS images to improve the resolution of the XPS images. To do quantitative confocal imaging accurately, data must be obtained from the top, bottom and middle of the sample. If the sample can be peeled, data can be obtained from the top and bottom of the sample. The sample can then be microtomed and the slices can be analyzed by XPS to obtain data from the center of sample. In addition to XPS, AFM and confocal microscopy, imaging FTIR data will be added to the image fusion procedure.

Preliminary Evaluation of Fluorescent Polymer Beads for Image Registration and 3D Feature Correlation

This work demonstrated the feasibility of using polymer microspheres in multitechnique studies using AFM, XPS and confocal microscopy. For this study it was determined that the best method for obtaining individual microspheres on the surface was to prepare them in a 0.01% w/v aqueous solution, and deposit them on the silicon substrate. This solution was sufficiently dilute to prevent the clustering of beads. In addition the proper polymer had to be chosen so that a single bead could be analyzed by AFM, XPS and confocal microscopy. An O 1s XPS image of single bead embedded in polypropylene proved useful for imaging a single bead with XPS, but beads were easily dislodged from the sample when imaged with AFM. PTFE-30 proved successful for imaging by AFM and confocal microscopy, but XPS data could not be obtained at the time of analysis.

The dimension of a single bead was measured by XPS, confocal microscopy, and AFM. The measured diameter from an XPS line-scan of a single bead was 8.5 μm . The measured diameter from a cross-sectional image using confocal microscopy was $\sim 9 \mu\text{m}$. Cross-sectional analysis of an AFM image obtained from a single bead gave a measured diameter 10.5 μm . This measurement was larger than the values obtained for XPS and con focal microscopy. The difference was probably due to polymer build-up around the bead during the spin coating process. This will give the bead a greater apparent width.

The XPS and confocal results agree reasonably well with the manufacturers quoted value of 9 μm .

Images of a single bead, embedded in PTFE-30, imaged with AFM and confocal microscopy were registered using the mutual information algorithm. The purpose of this was to see if the beads could be used as markers for image registration. This is a different approach to image registration. Since this was successful, this approach can be used.

In the future, the beads will serve as a marker for same area analysis and image registration. The bead patterns can be located and imaged by all three techniques. In addition, polymer microsphere kits will be obtained for intensity calibrations and calculating point-spread functions. Focal check fluorescent microspheres with diameters of 6 μm will be used for examining the alignment, stability of the laser, and confirming the optical sectioning thickness (Z-resolution) in three-dimensional imaging applications. This is important for knowing the depth of focus. Therefore the beads will play a dual role, image registration and calibration.

Summary

This research provides a new approach to the analysis of materials that are heterogeneous on the scale of microns. This work demonstrates a process that can be utilized to acquire image data using AFM, XPS, and LSCM. Data acquired from the same sample areas can be registered, facilitating phase identification and comparisons of chemical and topographic information acquired from polymer blends. Preliminary

methods for the development of non-destructive, quantitative 3-D volumes have been demonstrated and will be further developed in the coming years.

BIBLIOGRAPHY

- (1) Gilmore, I. S.; Seah, M. P.; Johnstone, J. E. *Surface and Interface Analysis* **2003**, 35, 888-896.
- (2) Feng, J.; Weng, L.-T.; Lin, L.; Chan, C.-M. *Surface and Interface Analysis* **2000**, 168-174.
- (3) Artyushkova, K. A.; Wall, B.; Koenig, J.; Fulghum, J. E. *Journal of Vacuum Science and Technology A* **2001**, 19, 2791-2799.
- (4) Lhoest, J.-B.; Bertrand, P.; Went, L. T.; Dewez, J. L. *Macromolecules* **1995**, 28, 4631-4637.
- (5) Schmidt, J. J.; Gardella, J. A. J.; Salvati, L. J. *Macromolecules* **1989**, 22, 4489-4495.
- (6) Lipatov, Y. S. *Progress in Polymer Science* **2002**, 27, 1721-1801.
- (7) Rhagavan, D.; Gu, X.; Nguyen, T.; Van Landingham, M.; Karim, A. *Macromolecules* **2001**, 33, 2573-2583.
- (8) Magonov, S. N.; Elings, V. B.; Papkov, V. S. *Polymer* **1997**, 297-307.
- (9) Wen, G.; Li, X.; Liao, Y.; An, L. *Polymer* **2003**, 4035-4045.
- (10) Affrosman, S.; Jerome, R.; O'Neill, S.; Schmitt, T.; Stamm, M. *Colloid & Polymer Science* **2000**, 278, 993-999.
- (11) Prosycevas, I.; Tamulevicius, S.; Guobiene, A. *Thin Solid Films* **2004**, 453-454, 304-311.
- (12) Chen, X.; McGurk, S. L.; Davies, M. C.; Roberts, C. J.; Shakesheff, K. M.; Tendler, S. J. B.; Williams, P. M.; Dawkes, A. C.; Davies, J.; Domb, A. *Macromolecules* **1998**, 31, 2278-2283.
- (13) Simmons, S.; Thomas, E. L. *Polymer* **1998**, 39, 5587-5599.
- (14) Jiang, X.; Huang, H.; Zhang, Y.; Zhang, Y. *Journal of Applied Polymer Science* **2004**, 92, 1437-1448.
- (15) Wickes, B. T.; Kim, Y.; Castener, D. G. *Surface and Interface Analysis* **2003**, 35, 640-648.
- (16) Burkhardt, C. A.; Gardella, J.A. Jr. *Applied Spectroscopy* **1993**, 47, 1636.
- (17) Briggs, D.; Fletcher, I. W.; Reichlmaier, S.; Agulo-Sanchez, J. L.; Short, R. D. *Surface and Interface Analysis* **1996**, 24, 419-421.
- (18) Fulghum, J. E. *Journal of Electron Spectroscopy and Related Phenomena* **1999**, 100, 331-355.
- (19) Ton-That, C.; Shard, A. G.; Teare, D. O. H.; Bradley, R. H. *Polymer* **2001**, 42, 1121-1129.
- (20) Wang, P.; Koberstein, J. T. *Macromolecules* **2004**, 37, 5671-5681.
- (21) Affrosman, S.; Kiff, S.; O'Neill, S.; Pethrick, R. A.; Richards, R. W. *Macromolecules* **1999**, 32, 27121-27130.

- (22) Garcia, R.; Tamayo, J.; San Paulo, A. *Surface and Interface Analysis* **1999**, 27, 312-316.
- (23) Bar, G.; Brandsch, R.; Whangbo, M. H. *Langmuir* **1998**, 14, 7343-7347.
- (24) Cleveland, J. P.; Anczykowski, B.; Schmid, A. E.; Elings, V. B. *Applied Physics Letters* **1998**, 72, 2613-2615.
- (25) Behrend, O. P.; Odoni, L.; Loubet, J. L.; Burnham, N. A. *Applied Physics Letters* **1999**, 75, 197-301.
- (26) Garcia, R.; Perez, R. *Surface Science Reports* **2002**, 47, 197-301.
- (27) Ratner, B. D.; Castner, D. G. In *Surface Analysis: The Principle Techniques*; Vickerman, J. C., Ed.; John Wiley & Sons: New York, New York, 1997; Chapter 3.
- (28) Riviere, J. C. In *Practical Surface Analysis: Auger and X-ray Photoelectron Spectroscopy*, 2nd ed.; Briggs, D.; Seah, M. P., Eds.; John Wiley & Sons: New York, New York, 1990; Vol. 1, Chapter 2.
- (29) Drummond, I. W. In *Surface Analysis by Auger and Photoelectron Spectroscopy*; Briggs, D.; Grant, J. T., Eds.; IM Publications Surface Spectra Limited: Manchester, UK, 2003; Chapter 5.
- (30) Tielsch, B. T.; Fulghum, J. E. *Surface and Interface Analysis* **1996**, 24, 422.
- (31) Kratos Home Page. <http://www.kratos.com/> (accessed June 2004).
- (32) ASTM: E 902-904 In *Annual Book Of ASTM Standards*, 1998;
- (33) Swift, P. *Surface and Interface Analysis* **1982**, 4, 47.
- (34) Moulder, J. F.; Stickle, W. F.; Sobol, P. E.; Bombden, K. D. *Handbook of X-ray Photoelectron Spectroscopy*; Perkin-Elmer Corporation: Eden Prairie, Minnesota, 1992.
- (35) Beamson, G.; Briggs, D. *High Resolution XPS of Organic Polymers: The Scientia ESCA 300 Database*; John Wiley & Sons: New York, New York, 1992.
- (36) Riviere, J. C.; Briggs, D. In *Practical Surface Analysis: Auger and X-ray Photoelectron Spectroscopy*, 2nd ed.; Briggs, D.; Seah, M. P., Eds.: New York, New York, 1990; Vol. 1, Chapter 3.
- (37) Thomas, E. A.; Fulghum, J. E. *Journal of Vacuum Science and Technology A* **1998**, 16, 1106.
- (38) Briggs, D. In *Surface Analysis of Polymers by XPS and Static SIMS*; Cambridge University Press: Cambridge, UK, 1998; Chapter 2.
- (39) Binnig, G.; Quante, C. F.; Gerber, C. *Physical Review Letters* **1986**, 56, 930-934.
- (40) Noy, A.; Husery, T. R. *Review of Scientific Instruments* **2003**, 74, 1217-1221.
- (41) Institut für Werkstofftechnik Home Page. <http://www.werkstoff.tu-ilmenau.de/Labore-und-Ausruestung/spmguide/> (accessed June 2004).
- (42) Zhong, Q.; Innis, D.; Kjoller, K.; Elings, V. B. *Surface Science Letters* **1993**, 290, L688-L692.
- (43) Zhou, H.; Li, A.; Wu, A.; Zheng, J.; Zhang, J. *Applied Surface Science* **2004**, 221, 402-407.
- (44) Tamayo, J.; Garcia, R. *Langmuir* **1996**, 12, 4430-4435.
- (45) Noy, A.; Sanders, C. H.; Vezenov, D. V.; Wong, S. S.; Lieber, C. M. *Langmuir* **1998**, 14, 1508-1511.

- (46) Magonov, S. N.; Elings, V. B.; Papkov, V. S. *Polymer* **1999**, *75*, 2551-2553.
- (47) Magonov, S. N.; Whangbo, M. H. *Surface Analysis with STM and AFM*; VCH Weinheim: New York, 1996.
- (48) MIT Web Media Home Page.
<http://web.media.mit.edu/~minsky/papers/ConfocalMemoir.html> (accessed July)
- (49) FluView Resource Center Home Page.
<http://www.olympusfluoview.com/theory/index.html> (accessed July 2004).
- (50) Ling, X.; Prtzker, M. D.; Byerly, J. J.; Burns, C. M. *Journal of Applied Polymer Science* **1998**, *67*, 149-158.
- (51) Li, L.; Sosnowski, S.; Chaffey, C. E.; Balke, S. T.; Winnik, M. A. *Langmuir* **1991**, *10*, 2495.
- (52) Verhoogt, H.; van Dam, J.; Posthuma de Boer, A.; Draaijer, A.; Houpt, P. M. *Polymer* **1993**, *34*, 1325.
- (53) Showgerdt, R. A. *Techniques for Image Processing and Classification in Remote Sensing*; Academic Press, Inc.: New York, 1983.
- (54) Chang, C. I.; Ren, H. *IEEE Trans. Geosci. Remote* **2000**, *38*, 1044-1063.
- (55) Bonnet, N. *Ultramicroscopy* **1995**, *57*, 17-27.
- (56) Artyushkova, K. A.; Fulghum, J. E. *Surface and Interface Analysis* **2002**, *33*, 185-195.
- (57) Almqvist, N. *Surface Science* **1996**, *355*, 221-228.
- (58) Pfeifer, P.; Obert, M. In *In The Fractal Approach to Heterogeneous Chemistry*; Avnir, D., Ed.; John Wiley & Sons: Great Britain, 1989; Chapter 1.
- (59) *Digital Instruments Software*, version 4.10; Digital Instruments: Santa Barbara, Ca., 1999
- (60) *ENVI: The Environment for Visualizing Images*, version 4.0; The Research Systems: Boulder, CO, 2003.
- (61) Pluim, J. P.; Maintz, A.; Viergever, M. *IEEE Transactions on Medical Imaging* **2000**, *22*, 1-6.
- (62) Pluim, J. P.; Maintz, A.; Viergever, M. *IEEE Transactions on Medical Imaging* **2003**, 986-1004.
- (63) Viola, P.; Wells III, W. *International Journal of Computer Vision* **1997**, *24*, 137-154.
- (64) Zitova, B.; Flusser, J. *Image and Vision Computing* **2003**, *21*, 977-1000.
- (65) Hill, D.; Batchelor, P., Registration Methodology: Concepts and Algorithms, 2000.
- (66) *MATLAB: The language of Technical Computing*. version 6.5; The Mathworks, Inc: Natick, Massachusetts, 2002.
- (67) Kotula, P. G.; Keenan, M. R. *Surface and Interface Analysis* **2004**, *36*, 203-212.
- (68) Statsoft Home Page. Vol. 2004.
- (69) Geladi, P.; Wold, S.; Esbensen, S. *Chemometrics and Intelligent Laboratory Systems* **1989**, *5*, 209-220.
- (70) MacGregor, J. F.; Bharati, M. H.; Yu, H. *Industrial and Engineering Chemical Research* **1998**, *37*, 4715-4724.

- (71) Artyushkova, K. A.; Fulghum, J. E. In *Surface Analysis by Auger and X-Ray Photoelectron Spectroscopy*; Briggs, D.; Grant, J. T., Eds.; IM Publications Surface Spectra Limited: Manchester, UK, 2003; Chapter 24.
- (72) Short, R. D.; Ameen, A. P.; Jackson, S. T.; Dawson, D. J.; O'Toole, L.; Ward, A. J. *Vacuum* **1993**, *44*, 1143-1160.
- (73) Leeson, A. M.; Alexander, M. R.; Short, R. D.; Briggs, D.; Hearn, M. J. *Surface and Interface Analysis* **1997**, *25*, 261-274.
- (74) Clark, M.; Burkhardt, C. A.; Gardella, J. A. *J. Macromolecules* **1989**, *22*, 4496.
- (75) Barillot, C.; Lemoine, D.; Le Briquer, L.; Lachman, F.; Gibraud, B. *European Journal of Radiology* **1993**, *17*, 22-27.
- (76) Schoder, H.; Erdi, E.; Larson, S.; Yeung, H. *European Journal of nuclear medicine and molecular imaging* **2003**, *30*, 1419-1437.
- (77) Chen, Y.; Wang, M. *Computerized medical imaging and graphics: official journal of the Computerized Medical Imaging Society* **2004**, *28*, 21-31.
- (78) Colin, A.; Boire, J. Y. *Computer methods and programs in biomedicine* **1999**, *60*, 107-116.
- (79) Ranchin, T.; Aiazzi, T.; Alparone, L.; Baronti, S.; Wald, L. *ISPRS Journal of Photogrammetry and Remote Sensing* **2004**, *21*, 177-192.
- (80) Bijaoui, A.; Bobichon, Y.; Vandame, B. *Vistas in Astronomy* **1997**, *41*, 366-372.
- (81) Hutter, H.; Nowikow, K.; Grammer, K. *Applied Surface Science* **2001**, *179*, 161-166.
- (82) Schaaff, T. G.; McMahon, J. M.; Todd, P. J. *Analytical Chemistry* **2002**, *74*, 4361-4369.
- (83) Plaschke, M.; Romer, J.; Kim, J. I. *Ultramicroscopy* **1998**, *75*, 77-83.
- (84) Mathur, D.; Nauman, E. B. *Journal of Applied Polymer Science* **1999**, *72*, 1151-1164.
- (85) Kim, G.; Libera, M. *Macromolecules* **1998**, *31*, 2569-2577.
- (86) *BioRad MRC 600 CoMOS*, version 6.01; Bio Rad: New Jersey
- (87) Dekeyser, C. M.; Biltresse, S.; Marchand-Brynaert, J.; Rouxet, P.G.; Dupont-Gillain Ch.C. *Polymer* **2004**, *45*, 2211-2219.
- (88) Kailas, L.; Nysten, B.; Bertrand, P. *Surface and Interface Analysis* **2004**, *36*, 1227-1230.
- (89) Kailas, L.; Audinot, J.-N.; Migeon, J.-N.; Bertrand, P. *Surface and Interface Analysis* **2004**, *231-232*, 289-295.
- (90) Molecular Probes Home Page. <http://www.probes.com/handbook/sections/2401.html> (accessed September 2004).